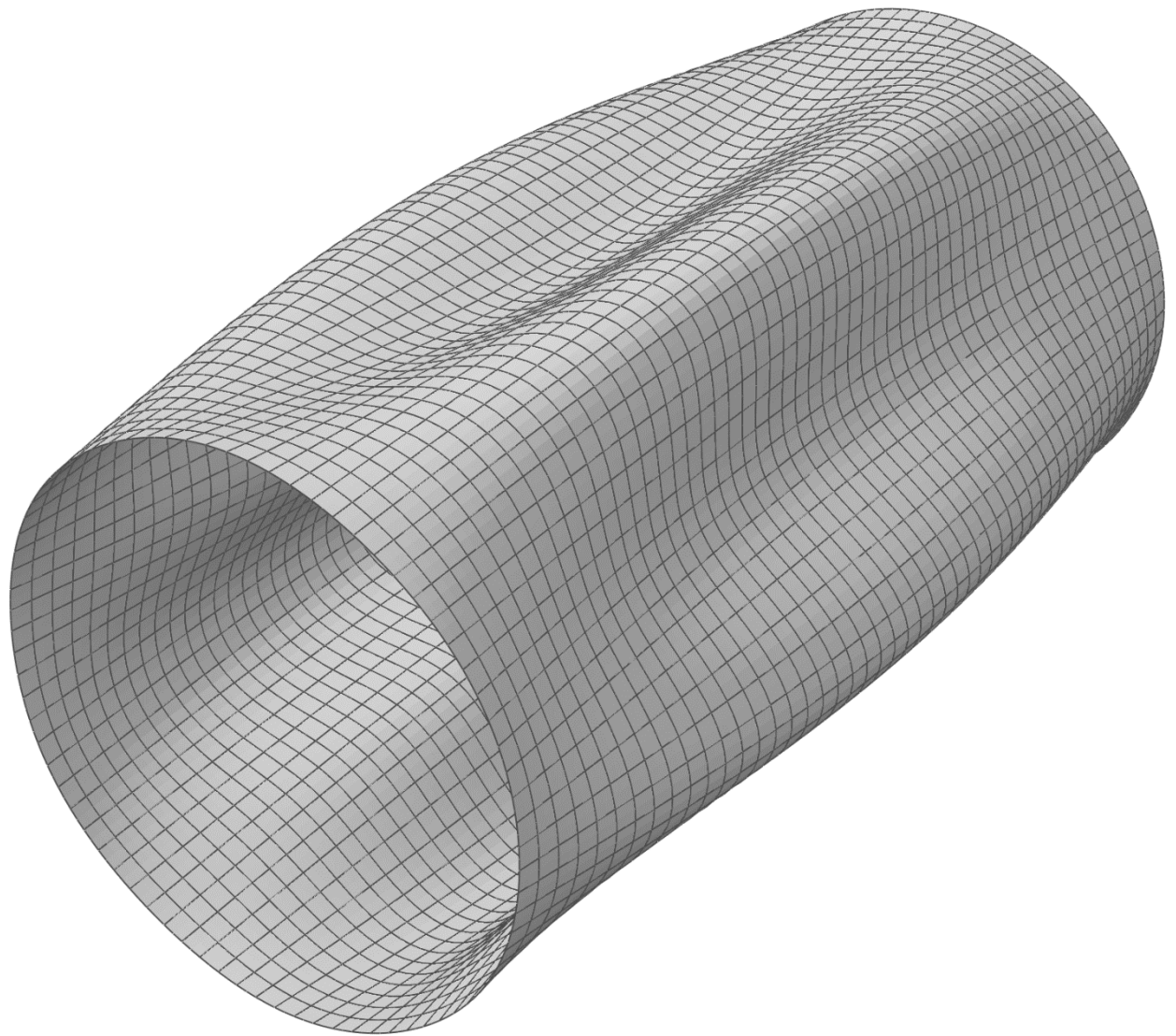


STOCHASTIC ANALYSIS OF GEOMETRIC IMPERFECTIONS OF A CYLINDRICAL SHELL STRUCTURE

MASTER THESIS



4th semester MSc – Structural and Civil Engineering
Martin W. Boserup & Christian L. Krog
Aalborg University
10-06-2014

Department of Civil Engineering

Aalborg University
Sohngårdsholmsvej 57
9000 Aalborg
www.civil.aau.dk

Master thesis

Title:

Simulation of geometrical imperfections and reliability estimation of cylindrical shell structures

Project period:

4th semester, Spring 2014
01-02-2014 to 10-06-2014

Project group:

Martin Winther Boserup
Christian Lebech Krog

Supervisors:

Henrik Stensgaard Toft
Søren Madsen

Printed editions: 5

Number of pages: 80 + CD

Abstract:

This thesis deals with buckling of axially compressed thin cylindrical steel shells. Through state-of-the-art review, it is shown that a slightly imperfect cylinder has a load-carrying capacity (critical buckling resistance), that is significantly reduced compared to a perfect cylinder. Therefore, three different imperfection patterns is analysed through the most complex of the recommended procedures in the Eurocode, namely the geometrically and materially non-linear analysis with imperfection. Furthermore, the reliability of the imperfect models, as well as semi-empirical mathematical models from the Eurocode and DNV is estimated along with a calibration of partial coefficients.

Martin Winther Boserup

Christian Lebech Krog

Preface

This master thesis is made in the period 03-02-2014 to 10-06-2014 on the 4th semester of the Master program in *Structural and Civil Engineering* under the *School of Engineering and Science* at *Aalborg University*.

Readers guide

To get an overview of the thesis, a description of the individual chapters is given in the following:

- **Introduction** - The buckling phenomenon is introduced through a history and a state-of-the-art review along with a derivation of the classical solution to the critical buckling stress of a axially compressed cylindrical shell. Based on this, a thesis statement is presented.
- **Finite Element Model** - The finite element model used through the thesis is presented, along with relevant numerical analysis methods.
- **Simulation of Imperfections** - By use of the presented finite element model, different approaches to simulate initial geometric imperfections is investigated.
- **Uncertainties related to the Critical Buckling Resistance** - In this chapter, main focus is put on estimating model uncertainties related to selected mathematical models used to calculate the load-carrying capacity.
- **Reliability Estimation of the Critical Buckling Resistance** - Reliability levels of the selected mathematical models are estimated and compared to target reliability levels, and it is investigated, whether an optimisation of the partial safety factor γ_M is possible.

In this thesis, sources are referred to by the Harvard method, [Surname, year]. A complete list of all sources is shown in the bibliography chapter in the end of the thesis. Sources with more than two authors are mentioned by the surname of the first author followed by "et al.". In the bibliography, books are listed by author, year, title, publisher and ISBN. Articles are listed by author, year, title and journal. Web pages are listed by author, year, title, url-address and date the page were accessed. Sources in figures/tables are shown in the caption below.

Figures and tables are numbered by given chapters, *i.e.* the first figure in *e.g.* chapter 3, will be named Figure 3.1. Similarly, equations are numbered by given chapters, *i.e.* the first equation in *e.g.* chapter 3, will be numbered (3.1).

A complete list of notations, symbols and abbreviations used in the thesis, is given on page 1. Vectors are displayed with a bar above the symbol, *e.g.* (\bar{v}) , while matrices are displayed with a bold symbol, *e.g.* (\mathbf{K}) .

Digital appendices (attached CD) include Matlab files, Abaqus files, Python files etc. Files that are relevant for a given section is placed in a folder on the CD with a similar name *i.e.* calculations used in section 2.4 is placed in the folder named **2.4 Boundary conditions**.

Contents

1	Introduction	3
1.1	Review of buckling history	6
1.2	General shell stability and buckling behavior	7
1.3	Linear shell theory	9
1.4	State-of-the-art review of simulating geometric imperfections	12
1.5	Thesis statement	14
2	Finite Element Model	15
2.1	Numerical analyses	15
2.1.1	Linear bifurcation analysis	15
2.1.2	Geometrically and materially non-linear analysis	15
2.2	Geometry	17
2.3	Material properties	18
2.4	Boundary conditions	19
2.5	Convergence analysis	22
2.6	Model summary	25
3	Simulation of Imperfections	27
3.1	Geometrical perfect cylinder	27
3.2	Geometrical imperfections by means of linear buckling mode-shapes	28
3.2.1	LBA	29
3.2.2	GMNIA	30
3.3	Geometrical imperfections by means of a single perturbation displacement	32
3.4	Geometrical imperfections by means of two perturbation displacements	35
3.5	Comparison/summarising of imperfections	38
4	Uncertainties related to the Critical Buckling Resistance	41
4.1	Finite element model representing experimental setup from Batterman	41
4.2	Estimation of model uncertainty according to DS/EN-1990	43
5	Reliability Estimation of the Critical Buckling Resistance	53
5.1	General reliability estimation	53
5.1.1	First-Order Reliability Method	54
5.1.2	Crude Monte Carlo simulation and Importance Sampling	55
5.2	Design equation and limit state function	56
5.2.1	Stochastic variables	57
5.3	Reliability estimation	58
5.3.1	Semi-empirical models	59
5.3.2	Numerical models	60
5.4	Calibration of partial safety factors	65
6	Conclusions	69

Bibliography**71****A Buckling strength according to EN 1993-1-6****B Buckling strength according to DNV-RP-C202****C Mode shapes**

Notation

Symbol	Description	Unit
b	Bias	[-]
C	Extension stiffness parameter	[N/m]
D	Bending stiffness parameter	[Nm]
E	Young's modulus	[Pa]
f_y	Yield stress	[Pa]
F	Force	[N]
h	Mathematical model	[-]
\mathbf{K}	Tangent stiffness matrix	[N/m]
l	Length	[m]
$N_x, N_\theta, N_{x\theta}$	Forces in x , θ and $x\theta$ -directions	[N]
P_f	Probability of failure	[-]
Q	Variable load	[N]
r	Radius	[m]
R_1, \dots, R_m	Regression parameters	[-]
t	Thickness	[m]
u, v, w	Displacements in x , θ and z -directions	[m]
\bar{v}_i	Buckling mode shapes (eigenvectors)	[m]
V	Coefficient of variation	[-]
V_Δ	Coefficient of variation of the model uncertainty	[-]
w_0	Imperfection amplitude	[m]
X_R	Model uncertainty of h	[-]
$X_{R,imp}$	Knock down factor for imperfections	[-]
$X_{R,GMNA}$	Knock down factor	[-]
X_Q	Model uncertainty of Q	[-]
\mathbf{X}	Stochastic variables	[-]
z_a, z_b	Design parameter	[-]
Z	Batdorf-parameter	[-]
α	Elastic imperfection reduction factor	[-]
α^2	Sensitivity measure	[-]
β	Reliability index	[-]
β_{target}	Target reliability	[-]
χ	Buckling reduction factor	[-]
Φ	Standard normal distribution function	[-]
γ	Partial safety factor	[-]
η	Parameter controlling the ratio between permanent and variable load	[-]
λ_i	Eigenvalue (elastic critical buckling resistance)	[N]
μ	Mean value	[-]

σ	Standard deviation	[-]
σ^2	Variance	[-]
σ_c	Characteristic buckling stress	[Pa]
σ_{cr}	Critical buckling stress	[Pa]
∇	Laplace operator	[-]
ν	Poisson's ratio	[-]

Abbreviations	Explanation
ASI	A xisymmetric I mperfections
DNV	D et N orske V eritas
DS/EN	D ansk standard/ E uropean standard
FERUM	F inite E lement R eliability U sing M atlab
FORM	F irst- O der R eliability M ethod
GDI	G eometrical D imple I mperfection
GMNA	G eometrically and M aterially N on-linear A nalysis
GMNIA	G eometrically and M aterially N on-linear A nalysis with I mperfection
LBA	L inear elastic B ifurcation A nalysis
LBMI	L inear B uckling M ode-shaped I mperfection
MCSIS	M onte C arlo S imulation with I mportance S ampling
MCS	C rude M onte C arlo S imulation
MDB	M odel D atabase
MNA	M aterially N on-linear A nalysis
MSI	M id-surface I mperfection
ODB	O utput D atabase
SPDI	S ingle P erturbation D isplacement I mperfection
SPLI	S ingle P erturbation L oad I mperfection
S4R	4 -node general-purpose shell, reduced integration with hourglass control, finite membrane strains
S8R	8 -node doubly curved thick shell, reduced integration
TPDI	T wo P erturbation D isplacement I mperfections
TPLI	T wo P erturbation L oad I mperfections

1 Introduction

In structures, many forms of instability can occur. The most common and important form is buckling, which occur primarily in slender members in compression. For these members, buckling is likely to occur at a much lower stress than the yield stress and buckling will therefore govern the load-carrying capacity [Williams & Todd, 2000].

When members under compression are relatively long they become sensitive to Euler buckling. Since the Euler buckling stress increases when the material is placed far away from the center axis, cylindrical shells are very efficient as compression members [Teng & Rotter, 2004]. Therefore cylindrical shells are widely used in civil engineering structures such as pipelines, silos, tanks, wind turbine towers, chimneys and off-shore platforms. However when the wall thickness becomes thinner, local buckling modes are appearing and becomes the dominating failure modes [Teng, 1996]. Examples of local buckling are shown in Figure 1.1 and 1.2.



Figure 1.1: Example of local buckling of a wine tank [Bushnell, 1981]

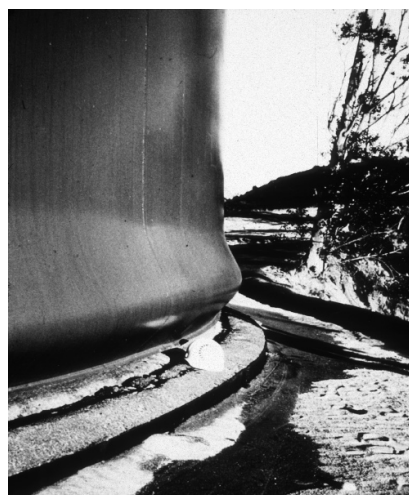


Figure 1.2: Example of “elephants foot” buckling of a water tank [Bushnell, 2011]

The buckling resistance of a thin cylindrical shell is very complex to estimate, since it is very sensitive to imperfections in both material, geometry, boundary conditions and applied loads. Moreover, when measuring the buckling resistance in laboratory tests, a very low and scattered resistance is observed compared to the “classical elastic critical stress” proposed by Lorenz, Timoshenko and Southwell [Teng & Rotter, 2004], see Figure 1.3. A derivation of the “classical elastic critical stress” is given in section 1.3 on page 9.

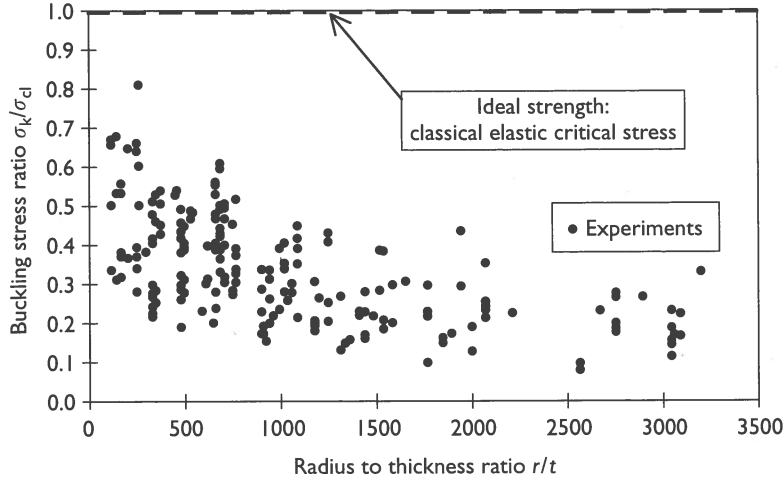


Figure 1.3: Experimental strength versus ideal strength of isotropic axial compressed cylinders. [Teng & Rotter, 2004]

It is observed that the bias increases with an increasing radius to thickness ratio r/t , which indicate that the critical buckling resistance is sensitive to changes of r/t . Due to the high bias, use of empirical “knock-down” factors are the primary approach to estimate the buckling resistance when designing cylindrical shells [Singer et al., 2002]. This approach is also used in [DS/EN-1993-1-6, 2007], where the characteristic buckling stress is given as:

$$\sigma_c = \chi f_{yc} \quad (1.1)$$

where

σ_c	Characteristic buckling stress [Pa]
χ	Buckling reduction factor [-]
f_{yc}	Characteristic yield stress [Pa]

The buckling reduction factor χ_x depends on the bifurcation load and the elastic imperfection reduction factor (α). In general (α) is known as a knock down factor, which depends on the shell geometry, load conditions, boundary conditions and the initial imperfection amplitude [Rotter & Schmidt, 2008]. The reduction factor is calibrated through experimental tests so that approximately 95% of the experimental test results have a larger buckling load than the characteristic buckling load obtained through (1.1) [Rotter & Schmidt, 2008]. The procedure to calculate $\sigma_{x,Rc}$, according to [DS/EN-1993-1-6, 2007], is shown in Appendix A.

Another procedure to estimate the buckling resistance, proposed by [DS/EN-1993-1-6, 2007], is the global numerical geometrically and materially non-linear analysis with imperfection (GMNIA). Here the finite element method is used to predict the most realistic buckling behavior. The following analyses with increasing complexity are used in the procedure suggested in [Rotter & Schmidt, 2008]:

- Linear bifurcation analysis (LBA) to obtain elastic critical buckling resistance.

- Material non-linear analysis (MNA) to obtain the plastic resistance.
- Geometrically and materially non-linear analysis (GMNA) to obtain the elastic-plastic buckling resistance of the perfect structure.
- Multiple GMNIA with different imperfection modes to obtain the worst imperfection form and thereby the elastic-plastic buckling resistance of the imperfect structure.
- Calibration of the elastic-plastic buckling resistance of the imperfect structure with known experimental test results.

The reliability of models with the highest complexity (GMNIA) strongly depends on the size and pattern of the initial imperfection. In [DS/EN-1993-1-6, 2007], no clear guideline of how to select the initial imperfections is given. It is therefore interesting to perform reliability estimates of the numerical models, to ensure that the structure meets the suitable requirements. To achieve safe structures, usually the *partial safety factor method* is used, where a target reliability β_{target} level is selected, depending on various measures. Target reliabilities recommended in [DS/EN-1990, 2007] for a one year and a 50 years reference period are listed in Table 1.1.

Reliability class	Minimum values of β	
	1 year reference period	50 years reference period
RC3	$\beta = 5.2(P_f \approx 10^{-7})$	$\beta = 4.3(P_f \approx 10^{-5})$
RC2	$\beta = 4.7(P_f \approx 10^{-6})$	$\beta = 3.8(P_f \approx 5 \cdot 10^{-5})$
RC1	$\beta = 4.2(P_f \approx 10^{-5})$	$\beta = 3.3(P_f \approx 5 \cdot 10^{-4})$

Table 1.1: Recommended minimum values for reliability index β (ultimate limit states) [DS/EN-1990, 2007].

As presented in Table 1.1, [DS/EN-1990, 2007] introduces three *reliability classes* depending on loss of human life or economical, social or environmental consequences. It is seen that a high reliability class leads to a high reliability index.

Since cylindrical shell structures are widely used in the off-shore industry, it is of interest to take into account the classification society, *Det Norske Veritas* (DNV). Reliability levels recommended in [DNV-Note-30.6, 2013] are presented in Table 1.2. The reliability levels are, in contrast to [DS/EN-1990, 2007], based on *consequences* and *class of failure*.

Class of failure	Consequences	
	Less serious	Serious
I - Redundant structure	$P_f = 10^{-3}(\beta \approx 3.09)$	$P_f = 10^{-4}(\beta \approx 3.71)$
II - Non-redundant structure, significant warning before failure	$P_f = 10^{-4}(\beta \approx 3.71)$	$P_f = 10^{-5}(\beta \approx 4.26)$
III - Non-redundant structure, no warning before failure	$P_f = 10^{-5}(\beta \approx 4.26)$	$P_f = 10^{-6}(\beta \approx 4.75)$

Table 1.2: Values of acceptable annual probabilities of failure P_f (and target reliabilities β) [DNV-Note-30.6, 2013].

Different reliability levels are observed, which reflect the different applications of the two standards. In this thesis, the main focus is inspired by the methods recommended in the Eurocode, while DNV is used in order to have a reference. In the following, a brief historical review of buckling will be presented along with a general description of the buckling phenomenon. The latest investigations in the field of simulation imperfections, is described in a state-of-the-art review, which ends up in a thesis statement.

1.1 Review of buckling history

Studies of buckling instability has been researched for more than two centuries. Leonard Euler was the first to derive a formula that gives the maximum axial load that a long, slender, ideal column can carry without buckling. This was done in 1744 and investigations on the subject has been going on ever since [Singer et al., 1998]. Approximately one century later, in 1845, Fairbairn and Hodgkinson conducted tests on thin walled tubes under axial compression. These studies were commenced in connection with the construction of the Britannia and Conway bridges in England. Later in 1882, construction began on Scotland's Firth of Forth bridge, which was made of tubular steel members, see Figure 1.4, and was finished in 1890 [Schmidt, 2000]. The bridges were constructed without clear knowledge about the buckling phenomenon, since no theoretical solution existed at that time.

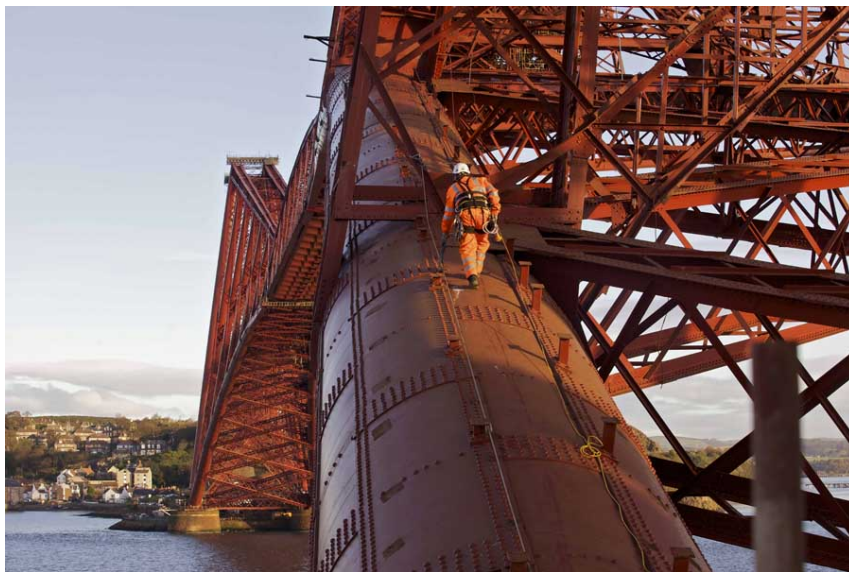


Figure 1.4: Tubular steel members of Firth of Forth bridge in Scotland. [Network Rail, 2012]

In 1905-1908, the first systematic study of elasto-plastic buckling of cylindrical shells was carried out at Trinity College in Dublin by W. E. Lilly. His work led to the conclusion that the buckling load becomes smaller with higher radius to thickness ratio (r/t) and the “true” resistance of a compressed cylindrical shell is the load that produces the buckling mode [Singer et al., 2002]. The theoretical solution to axial compressed cylindrical shells was solved independently by Lorenz, Timoshenko and Southwell in 1910 and is, as mentioned earlier, known as the “classical elastic critical stress”. Soon after, the theoretical solutions for the critical load under external pressure and torsional shear, was solved successfully by v. Mises and Schwerin, respectively [Singer et al., 2002].

Through the 1930s a lot of work within linear shell theory was done, especially by

Timoshenko, Flügge and Donnell. Flügge was the first to present a theory of cylindrical shells in 1934, but around the same time, Donnell presented a theory that was simpler and easier to solve [Zingoni, 1997]. Though, no matter how precise the used linear theory was, major deviations from experimental results was observed. This resulted in safety factors as large as 4 to “knock down” the critical buckling stress, which unfortunately still led to unsafe structures [Schmidt, 2000].

Even though a lot of work was done on linear shell theory, it was not before the 1950s that it was realised that the large discrepancies between theoretical and experimental results was due to unavoidable imperfections and unpredictable post-buckling behavior. The effect of geometrical imperfections can be seen in Figure 1.5, where it is observed, that a minor imperfection amplitude, decreases the critical buckling resistance dramatically. The most notable researchers to implement imperfections and use non-linear formulations of Donnell’s shell theory were Karman and Tsien (1941) and Donnell and Wan (1950) [Teng & Rotter, 2004] [Schmidt, 2000].

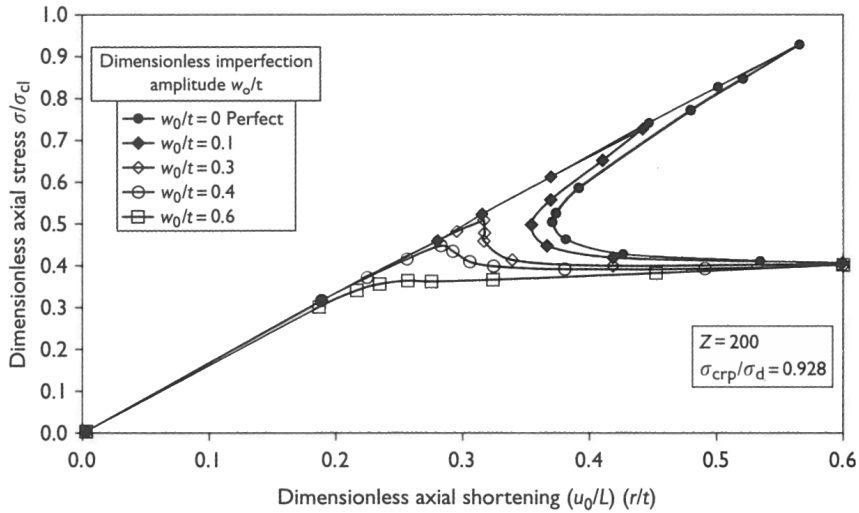


Figure 1.5: Load - axial shortening relationships for cylinders with circumferential asymmetric imperfections. [Teng & Rotter, 2004]

However, with the knowledge of the effects of geometrical imperfections, guidelines of how to take these into account was not yet available. This encouraged Seide, Weingarten and Morgan to publish a collection of experimental results in 1960 which later, in 1965, led to the basis of the NASA SP-8007 guideline [Castro et al., 2013].

Work on buckling resistance of cylindrical shell structures has since the late 1970s been dominated by numerical approaches due to the increasing availability of computational power. Especially the finite element method has been widely used to predict the behavior of cylindrical shells by using fully non-linear theory combined with imperfect geometry [Schmidt, 2000].

In the following section, a brief introduction to general shell stability and buckling behavior, including a derivation of the classical elastic critical stress is given.

1.2 General shell stability and buckling behavior

Two ways of instability can occur, namely *bifurcation of equilibrium* and *limitation of equilibrium*. A typical type of *limitation of equilibrium* is known as snap-trough buckling

[Farshad, 2010]. Both behaviors causes the structure to change shape and thereby reduce the stiffness resulting in unwanted deflections. The controlling parameter of the stability is the membrane stresses in the shell wall [Rotter & Schmidt, 2008].

Snap-through buckling can be illustrated as shown in Figure 1.6. At a certain point a critical load is reached (snap-through load) and the system becomes unstable. At this point buckling occurs rapidly and the structure exhibits a dynamic jump which cause large deformations, as illustrated in Figure 1.7. After the dynamic jump, once again the structure becomes stable, usually in an inverted form.

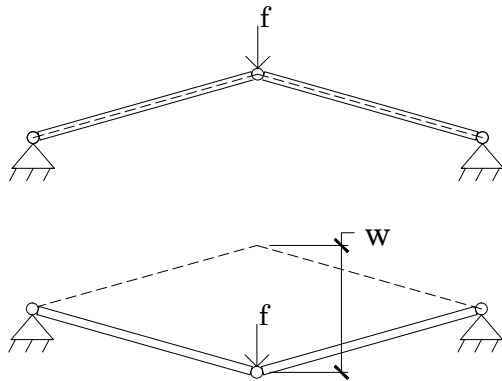


Figure 1.6: Illustration of geometric change due to snap-through buckling. [Rotter & Schmidt, 2008]

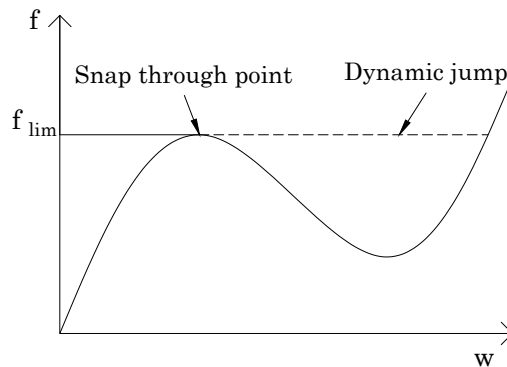


Figure 1.7: Illustration of load displacement response of snap-through buckling. [Rotter & Schmidt, 2008]

Typical, snap-through occurs in domes and arches, but might also appear in cylindrical shells under certain conditions.

When minimum two possible equilibrium paths pass through the same point, *bifurcation buckling* occur. An example of bifurcation buckling in a column is shown in Figure 1.8. The point referred to as the bifurcation point is given as the intersection between the pre- and post-buckling equilibrium paths. When traveling from the origin towards the bifurcation point, shown in Figure 1.9, the structure is stable. From the bifurcation point the pre-buckling equilibrium path becomes unstable, and the post-buckling equilibrium path can be either stable or unstable, depending on the type of bifurcation [Rotter & Schmidt, 2008].

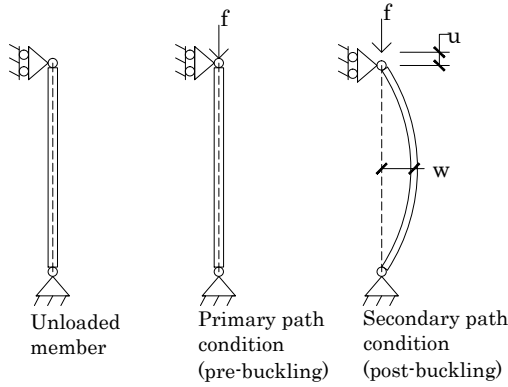


Figure 1.8: Illustration of pre- and post buckling behavior of a column. [Rotter & Schmidt, 2008]

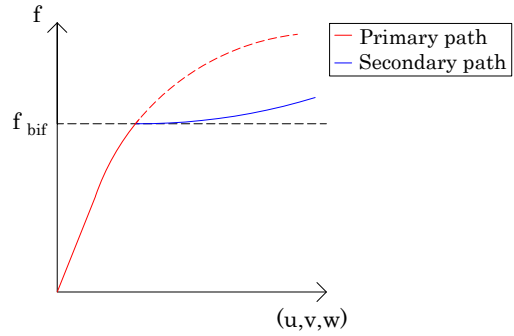


Figure 1.9: Illustration of load displacement response of a column. [Rotter & Schmidt, 2008]

The post-buckling deformations of the structure, will take form in a different pattern, named the buckling mode. In some cases more than 100 critical buckling modes can lie with a bifurcation load within 1%, and for this reason the “unique” critical bifurcation load is hard to predict [Teng & Rotter, 2004]. Normally the buckling load leading to the lowest load-carrying capacity is considered. Usually, columns and beams, undergoing axial compression, exhibit stable symmetric bifurcation, whereas the typical post buckling behavior of cylindrical shells is unstable. Due to this fact, the buckling resistance of cylindrical shells is highly sensitive to geometric imperfections [Rotter & Schmidt, 2008].

In the following, a derivation of the classical solution to the critical elastic buckling stress will be given.

1.3 Linear shell theory

This section is based on [Brush & Almroth, 1975] and [Farshad, 2010]

In this section a linear stability analysis will be carried out for a cylindrical shell, see Figure 1.10, under axial loading. The linear theory assumes a perfect system and predicts the bifurcation point and thereby the critical buckling stress. As stated by [Farshad, 2010], the linear theory is not capable of predicting the “real” buckling behavior of cylindrical shells. To obtain a “realistic” buckling behavior, implementation of imperfections and use of non-linear shell theory is therefore necessary. Nevertheless, the linear theory still provide useful results of the buckling behavior and will be presented briefly in the following.

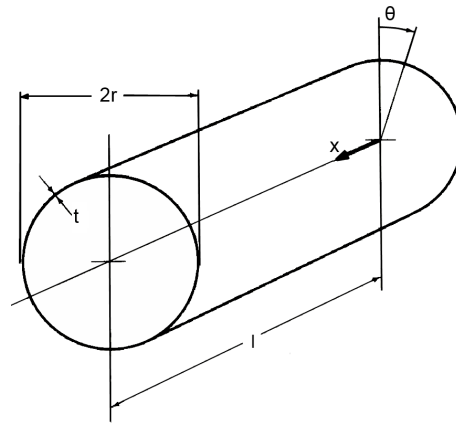


Figure 1.10: Cylindrical shell with coordinate system. [Brush & Almroth, 1975]

The “real” prebuckling behavior of a perfect cylindrical shell under axial compression is shown in Figure 1.11. It is seen that the thickness of the shell wall is varying along the x-axis. However, in the linear theory it is assumed that the wall thickness is constant as shown in Figure 1.12.

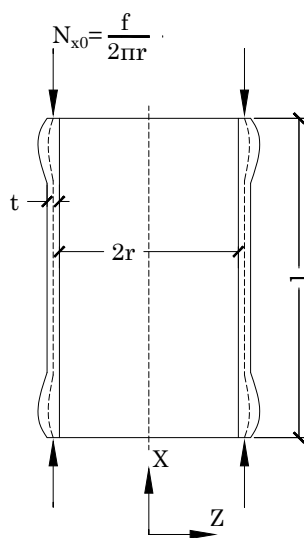


Figure 1.11: “Real” prebuckling behavior of a cylinder subjected to axial compression. [Brush & Almroth, 1975]

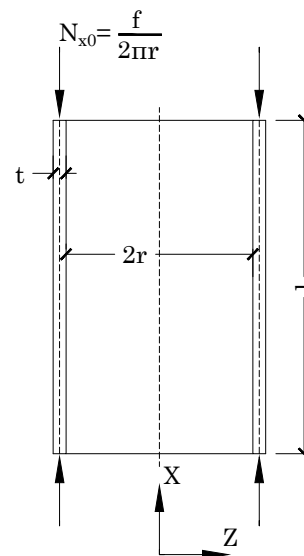


Figure 1.12: Linear prebuckling behavior of a cylinder subjected to axial compression. [Brush & Almroth, 1975]

The goal is to determine the critical buckling load and thereby the critical buckling stress. The analysis contains following steps suggested by [Farshad, 2010]:

- A deformed infinitesimal equilibrium state is considered as shown in Figure 1.13.
- Equilibrium, kinematic and constitutive equations are derived for the shell element.
- When constructing the equilibrium, kinematic and constitutive equations, a set of homogeneous differential equations are derived, where the critical buckling load is the unknown parameter.

- These homogeneous differential equations can be rewritten and identified as an eigenvalue problem, where the nontrivial solution is sought.

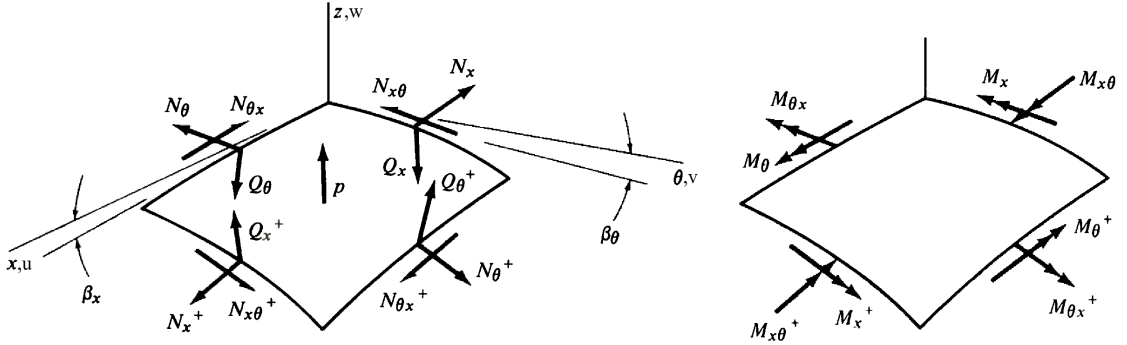


Figure 1.13: Forces (left) and moments (right) on an infinitesimal element. [Brush & Almroth, 1975]

The buckling behavior can be described by the governing linear differential equations (1.2) to (1.4), named the *Donnell stability equations in uncoupled form*.

$$\nabla^4 u = -\frac{\nu}{r} \frac{\partial^3 w}{\partial x^3} + \frac{1}{r^3} \frac{\partial^3 w}{\partial x \partial \theta^2} \quad (1.2)$$

$$\nabla^4 v = -\frac{2 + \nu}{r^2} \frac{\partial^3 w}{\partial x^2 \partial \theta} - \frac{1}{r^4} \frac{\partial^3 w}{\partial \theta^3} \quad (1.3)$$

$$D \nabla^8 w + \frac{1 - \nu^2}{r^2} C \frac{\partial^4 w}{\partial x^4} - \nabla^4 \left(N_x \frac{\partial^2 w}{\partial x^2} + \frac{2}{r} N_{x\theta} \frac{\partial^2 w}{\partial x \partial \theta} + \frac{1}{r^2} N_\theta \frac{\partial^2 w}{\partial \theta^2} \right) = 0 \quad (1.4)$$

where

∇	Laplace operator [-]
u, v, w	Displacements in x , θ and z -directions [m]
r	Undeformed middle surface radius [m]
ν	Poisson's ratio [-]
$C = \frac{Et}{1-\nu^2}$	Extension stiffness parameter [N/m]
$D = \frac{Et^3}{12(1-\nu^2)}$	Bending stiffness parameter [Nm]
$N_x, N_\theta, N_{x\theta}$	Forces in x , θ and $x\theta$ -directions [N]

A simple supported, axially compressed cylindrical shell with perfect geometry at the initial condition is considered. The homogenous differential equation in the z -direction (1.4), can then be simplified by assuming that the membrane forces N_θ and $N_{x\theta}$ are small compared to the axial force N_x :

$$N_x = -\frac{F}{2\pi r} \quad , \quad N_{x\theta} = N_\theta = 0 \quad (1.5)$$

By implementation of these values into (1.4) the differential equation simplifies to:

$$D \nabla^8 w + \frac{1 - \nu^2}{r^2} C \frac{\partial^4 w}{\partial x^4} + \frac{F}{2\pi r} \nabla^4 \frac{\partial^2 w}{\partial x^2} = 0 \quad (1.6)$$

It is assumed that the shell has zero displacements in the z-direction and zero curvature at the ends:

$$w = 0 \quad , \quad \frac{\partial^2 w}{\partial x^2} = 0 \quad (1.7)$$

An assumed solution to the homogeneous partial differential equations for the shell is given as;

$$w = C_1 \sin(n\theta) \sin\left(\frac{m\pi r}{l} x\right) \quad (1.8)$$

where

C_1	Constant [-]
m, n	1,2,3,..., [-]
l	Length [m]

This solution satisfies the end conditions, given in (1.7), and by inserting (1.8) in (1.6) along with use of the constitutive and kinematic relations an eigenvalue problem can be obtained. In (1.8), m and n are chosen, such that the lowest critical stress is obtained. The trivial solution to the problem corresponds to the prebuckled configuration, and therefore the nontrivial solution is sought and obtained in rearranged form in terms of the critical stress:

$$\sigma_{cr} = \frac{E}{\sqrt{3(1-\nu^2)}} \frac{t}{r} \quad (1.9)$$

where

σ_{cr}	Critical buckling stress [Pa]
E	Young's modulus [Pa]
t	Thickness [m]

This is known as the classical solution of the critical buckling stress for an axially compressed cylindrical shell, and is in many applications used as a reference point to more complex theories. In the following section, a state-of-the-art review of imperfect cylindrical shells under axial compression will be presented.

1.4 State-of-the-art review of simulating geometric imperfections

This thesis will focus on modeling geometric imperfection of axial loaded cylindrical shells and therefore this state-of-the-art review will focus on this area. Other types of investigation in this field could include; load combinations [Winterstetter & Schmidt, 2002] [Mathon & Limam, 2006], composite materials [Orifici & Bisagni, 2013] and influence of boundary conditions [Schmidt, 2000].

Recent work on modeling geometric imperfection include [Castro et al., 2013], where five different methods, used to create geometric imperfections and knock down factors, were compared for a composite cylindrical shell. The five methods were;

- Linear buckling mode-shaped imperfection (LBMI)
- Single perturbation load imperfection (SPLI)
- Geometrical dimple imperfection (GDI)
- Axisymmetric imperfections (ASI)
- Mid-surface imperfections (MSI)

The idea of implementing linear buckling mode-shaped imperfection (LBMI), is to calculate the eigenmodes in a LBA and apply them to the perfect model, as initial imperfections. The scaling factor in this method is the imperfection amplitude. Another method, the single perturbation load imperfection (SPLI), leads to a local displacement at a given position of the cylinder.

The displacement field of the geometrical dimple imperfection (GDI), see Figure 1.14, is given as radial displacements, see (1.10), and is defined as a dimple cosine with wavelengths along the circumference (a) and the meridian (b)

$$\Delta r(\varphi, \zeta) = \frac{w_0}{4} \left[1 - \cos \left(\frac{2\pi r}{a} \varphi \right) \right] \left[1 - \cos \left(\frac{2\pi}{b} \zeta \right) \right] \quad (1.10)$$

where

w_0	Imperfection amplitude [m]
a	Wavelength along the circumference [m]
b	Wavelength along the meridian [m]
r	Radius [m]

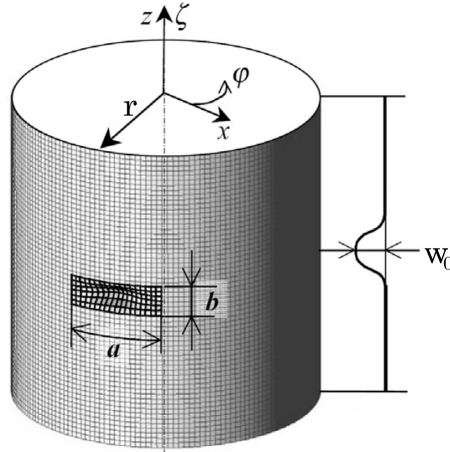


Figure 1.14: Imperfection pattern for a GDI. [Castro et al., 2013]

The axisymmetric imperfections ASI differs from the GDI, when implementing it as initial geometric imperfection, by only taking the meridional wavelength (b) into account, and (1.10) reduces to (1.11);

$$\Delta r(\varphi, \zeta) = \frac{w_0}{2} \left[1 - \cos \left(\frac{2\pi}{b} \zeta \right) \right] \quad (1.11)$$

The imperfection pattern for the mid-surface imperfections (MSI) was measured on real laminated composite cylinders by [Degenhardt et al., 2008], and implemented as initial imperfections.

[Castro et al., 2013] stated that the fairly simply SPLI method gave the lowest “knock-down” factors *i.e.* the largest buckling stress and was preferred by the authors.

A similar conclusion was made by [Wang et al., 2013], where analyses were made on aluminum cylindrical shells, and it was stated by the authors, that the dimple imperfections were more realistic and physical meaningful compared to the eigenmode shape imperfections.

A similar approach to MSI to predict the geometrical imperfection of cylindrical shell structures was made by [De Paor et al., 2012], where the authors obtained detailed measurements of 39 small-scale steel cylindrical cans by scanning the objects. Through the obtained data it was stated that the magnitude of the radial deviation approximately could be represented by a Gaussian distribution. Further a two dimensional random field of radial deviation was generated by use of the Monte Carlo method and validated with experimental results. [De Paor et al., 2012] suggested to implement these random fields into a geometrical and material non-linear finite element analysis to predict the buckling stress.

Investigation on “axially imperfect” cylinders, *i.e.* imperfections in the length direction, has been carried out by [Blachut, 2010] and [Broggi et al., 2011]. [Blachut, 2010] introduced the axial imperfection by varying the length sinusoidally, whereas [Broggi et al., 2011] introduced the axial imperfection by a random field. Common to both investigations was that the axial imperfection have a remarkable influence on the critical buckling load. [Blachut, 2010] shows that “axially imperfect” cylinders can have a load carrying capacity that is up to five time smaller than the load carrying capacity of an “eigenmode-imperfect” cylinder.

1.5 Thesis statement

It has been shown through history review and state-of-the-art that the buckling phenomenon is very complex and even though a lot of research has been carried out in this field a lot of questions are still unanswered. Especially the simulation of initial imperfections and the influence on the load-carrying capacity will be investigated. The following questions are sought answered in this thesis:

- In which way can the geometrical imperfection be simulated?
- How does the simulated imperfections influence the load-carrying capacity (critical buckling resistance) and reliability level?

To narrow down the focus area, limitations have been made. The cylindrical shells will be made of steel, modeled under axial compression and with boundary conditions corresponding to a middle section of a given structure. The radius-thickness ratio (r/t), is chosen to be 250. A detailed description of the finite element model is presented in the following chapter.

It is of interest to calculate the model uncertainty, of selected methods, and since no test results are available for the certain conditions mentioned above, test results from [Batterman, 1965](cylindrical aluminum shells) will be used. Results from numerical models, will be compared with the semi-empirical methods suggested in [DS/EN-1993-1-6, 2007] and [DNV-RP-C202, 2013].

2 Finite Element Model

In the present chapter, the finite element model used in this thesis will be presented. The model is created in the commercial finite element program Abaqus [Simulia Corp., 2013]. First, the different analysis methods will be described. Secondly, the geometry and material properties will be determined along with boundary and load conditions. Subsequently, a convergence analysis will be conducted in order to determine element type and mesh size.

2.1 Numerical analyses

In this thesis, mainly three types of analyses will be performed, namely linear bifurcation analysis (LBA) and geometrically and materially non-linear analysis of a perfect (GMNA) and imperfect structure (GMNIA).

2.1.1 Linear bifurcation analysis

Linear bifurcation analysis is carried out to obtain the elastic critical buckling resistance of the perfect structure. In Abaqus the elastic critical buckling resistance is obtained through the eigenvalue problem given in (2.1), where the load, for which the stiffness matrix becomes singular, is sought [Simulia Corp., 2013].

$$(\lambda_i \mathbf{K}) \bar{v}_i = 0 \tag{2.1}$$

where

λ_i		Eigenvalue (elastic critical buckling resistance)
\mathbf{K}		Tangent stiffness matrix
\bar{v}_i		Buckling mode shapes (eigenvectors)

The obtained buckling mode shapes does not represent real magnitudes of deformation at the critical buckling load since they are normalised, such that the maximum displacement is 1.0 [Simulia Corp., 2013].

2.1.2 Geometrically and materially non-linear analysis

Geometrically and materially non-linear analysis is carried out to obtain the elastic-plastic buckling resistance of the perfect structure (GMNA) and the imperfect structure (GMNIA). In contrast to the LBA, these analyses use non-linear large deflection theory and nonlinear elastic plastic material law. Therefore a non-linear solution algorithm is required to solve the non-linear equilibrium equations.

Newton Raphson method

As standard setting, Abaqus uses the *force-residual based method* Newton Raphson, which is the most common iterative solution scheme. One of the reasons for this, is due to the high rate of convergence, *i.e.* few iterations are needed to solve the non-linear equations [Ottosen & Ristinmaa, 2005]. Figure 2.1 shows the procedure of calculating a non-linear equation be means of Newton Raphson. The idea is to obtain a solution that satisfy the

equilibrium equations. This is done by ensuring that the external forces are equal to the internal forces.

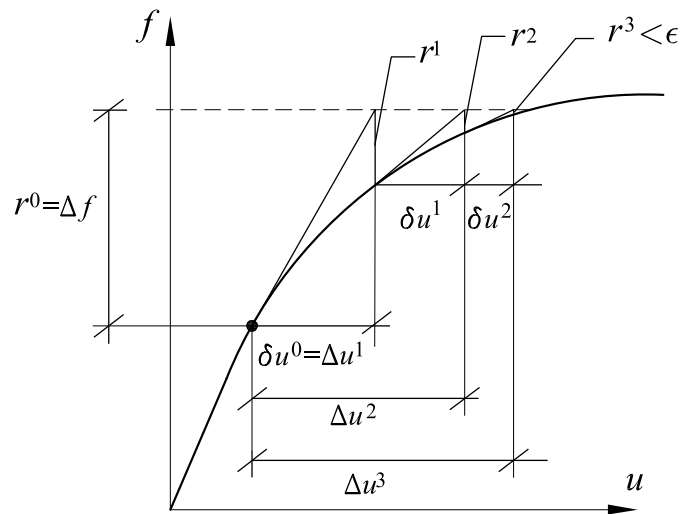


Figure 2.1: Solution of one-dimensional nonlinear equation by Newton-Raphson [Krabbenhøft, 2002].

The method begins at the last known point of equilibrium, where a new increment in force is applied. This is done by linearising the equation by use of the tangent stiffness from the known point and it leads to a solution that generates a residual external force r rather than satisfying the non-linear equation. The equation is linearized once again from the new point, and this procedure is repeated until equilibrium is reached *i.e.* the selected error ϵ is sufficiently small [Krabbenhøft, 2002].

However since the behavior of a cylindrical shell under axial compression can be highly unstable, *i.e.* a decrease in load and/or displacement as the non-linear equilibrium path evolves, the Newton Raphson method is not suitable, as illustrated in Figure 2.2. The iterative approach used in Newton Raphson would only be able to predict the response of ABDE, *i.e.* only a part of the real solution is obtained [Ottosen & Ristinmaa, 2005].

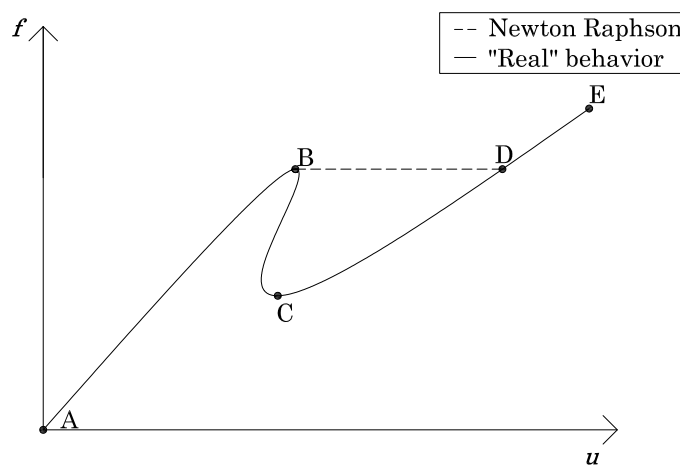


Figure 2.2: Load-displacements curve of a typical unstable behavior for a given structure, where flaws of the Newton Raphson are illustrated.

In order to be able to trace the response shown in Figure 2.2 another iterative scheme is needed, and the *arc-length* method is very suitable of predicting the behavior, due to the use of combined load and displacement control. [Ottosen & Ristinmaa, 2005]

Riks method

The modified Riks method is used to solve the non-linear equations, since it has been proven to be the most successful method [Simulia Corp., 2013]. The Riks method is a linearised version of the arc-length method, where instead of using a constraint arc surface, the iterative change is made orthogonal to the predictor solution, shown by the normal plane, n_i in Figure 2.3.

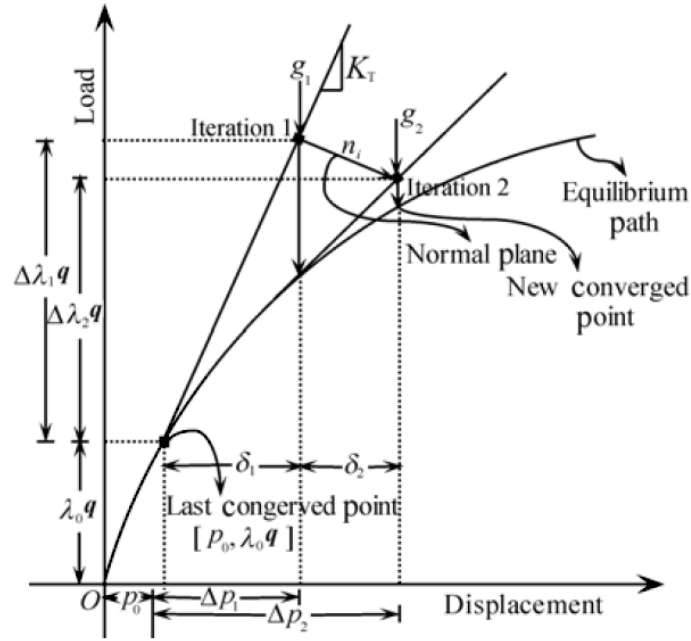


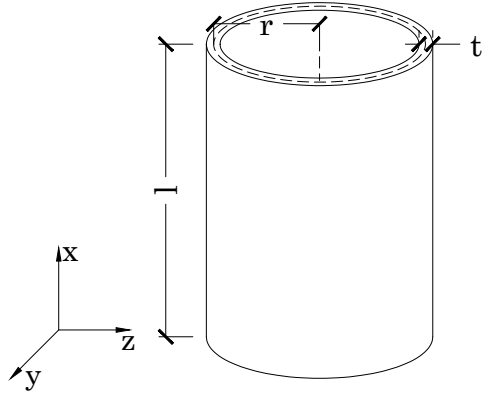
Figure 2.3: Solution of nonlinear equation by Riks [Memon & Su, 2004].

The method searches a solution in a space defined by the displacement p , and a load state λq , where λ is a load proportionality factor. In contrast to the Newton Raphson method, the Riks method solves the loads and displacements simultaneously, which makes it possible to pass any limit point. The iteration stops when the out of balance force vector g_i becomes sufficiently small. Initially, an arc length is defined and thereby the initial load proportionality factor λ . In Abaqus, the following increment size is automatically selected by an incrementation algorithm [Simulia Corp., 2013].

Due to the highly unstable behavior of a cylindrical shell under axial loading, the Riks method will be used as the non-linear solver in this thesis.

2.2 Geometry

The geometry of the cylindrical shell is defined as shown in Figure 2.4, whereas the characteristic geometry parameters are listed in Table 2.1.



Notation	Symbol	Value	Unit
Length	l	10	[m]
Radius	r	2.5	[m]
Thickness	t	0.01	[m]
Radius-thickness ratio	r/t	250	[-]

Table 2.1: Characteristic geometry parameters.

Figure 2.4: Geometric parameters of the cylinder.

The selected radius-thickness ratio is, from a civil engineering point of view, an upper bound. The reason for this choice, is to ensure that buckling occur rather than yielding in the material. Furthermore the geometry is selected such that the cylinder is categorized as *medium* according to [DS/EN-1993-1-6, 2007], and it is ensured that r, t is placed at a reasonable distance from the boundary line between long and medium, as illustrated in Figure 2.5.

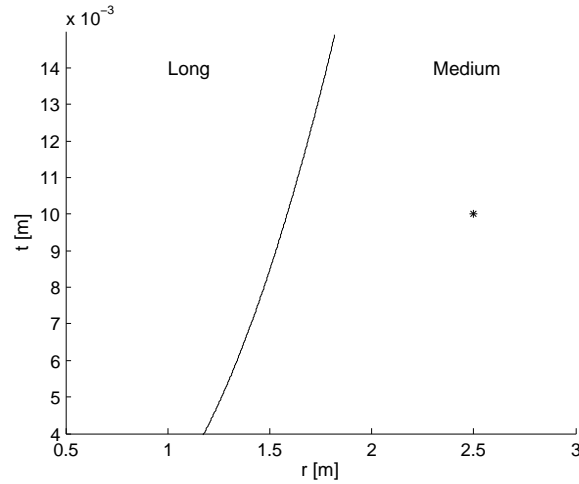


Figure 2.5: Illustration of medium and long categories with a length of 10 m according to [DS/EN-1993-1-6, 2007]. (*) represents the selected r, t .

The reason for selecting a *medium* cylinder is that, according to [Teng & Rotter, 2004], most civil engineering structures under axial compression can be placed into the category of medium cylinders.

2.3 Material properties

The material used for the model is steel with an ideal elastic perfect plastic material model as shown in Figure 2.6 along with characteristic material properties listed in Table 2.2. The multi-axial stress yield criterion is assumed to be von Mises with associated flow rule for plastic strain increment since this criteria is commonly used for steel.

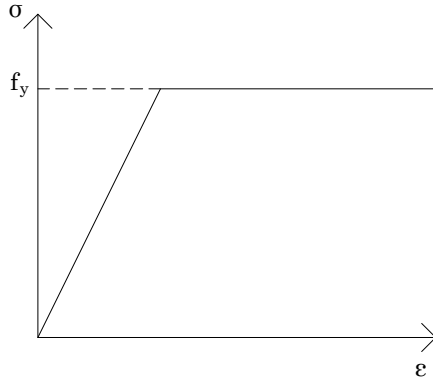


Figure 2.6: Stress-strain curve for selected material model.

Notation	Symbol	Value	Unit
Young's modulus	E	$210 \cdot 10^9$	[Pa]
Poisson's ratio	ν	0.3	[-]
Yield stress	f_{yc}	$235 \cdot 10^6$	[Pa]

Table 2.2: Characteristic values of material properties.

2.4 Boundary conditions

In this section it is investigated, in which way the boundary conditions can be modeled to simulate a middle section of a given civil engineering structure. Three boundary conditions are selected and shown in Figure 2.7. BC1 and BC2 are selected such that they represent two ways of modeling a simple supported cylinder. BC3 is selected to investigate the influence of fixed rotations at the boundaries. Since BC1 is similar to a simple support, it allows rotation in all directions. Furthermore it is axially loaded in the top and bottom. BC2 is axially loaded at the top, and is fixed against displacements in the x -direction at the bottom. Theoretically, the load-carrying capacity of a cylinder with BC1 and BC2, should be equal. BC3 is similar to a fixed-fixed support, which restraints it from rotation at the boundaries. The load conditions are similar to BC1.

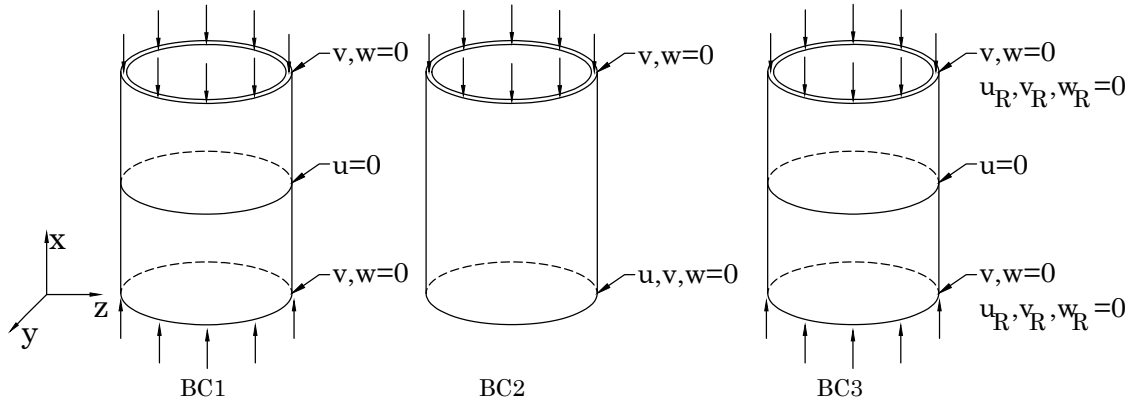


Figure 2.7: Selected boundary conditions for the cylinder. u, v and w are displacements in the x, y and z -directions, while lower case R represents rotation. The arrows represent the applied axial force.

In order to compare the influence of the three boundary conditions, the critical buckling resistance is obtained through a linear bifurcation analysis (LBA) along with the first mode shape. The critical buckling resistances are listed in Table 2.3 and Figure 2.8 shows the mode shapes.

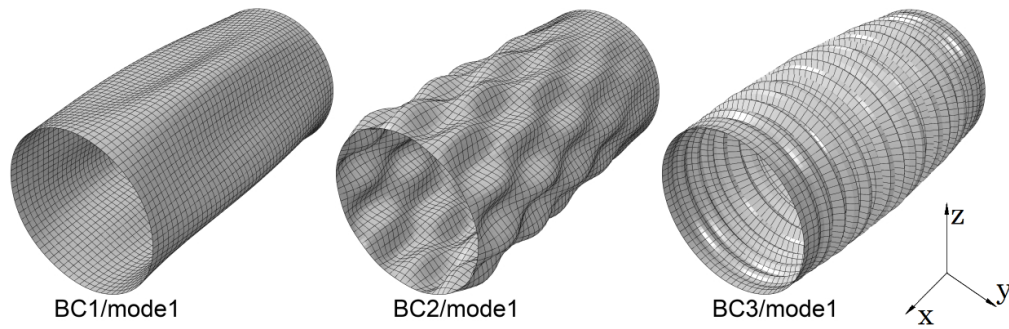


Figure 2.8: First mode shape for BC1, BC2 and BC3 obtained through LBA. Scale=0.3

It is seen that the mode shapes obtained for the cylinder with BC1 and BC3 are symmetric, while the mode shape for BC2 is asymmetric. The reason for this asymmetry is that the force is applied at the top. Additionally it is observed that mode shape 1 for BC1 only develops $\frac{1}{2}$ wave in the meridional direction, while BC2 develops $2\frac{1}{2}$ waves and BC3 develops more than 10 waves. These observations correspond well with the critical buckling resistances listed in Table 2.3, where BC2 and BC3 needs to be exposed to a larger amount of energy to excite the first mode.

	BC1	BC2	BC3
σ_{cr} [MPa]	479	508	505

Table 2.3: Critical buckling resistances for the three boundary conditions obtained through LBA.

For further comparison of the influence of BC1, BC2 and BC3, material and geometrical non-linearity is taken into account through a GMNA. The displacement fields, shown in Figure 2.10, are extracted at a post buckling state, corresponding to an axial shortening of 0.02 m, shown in Figure 2.9.

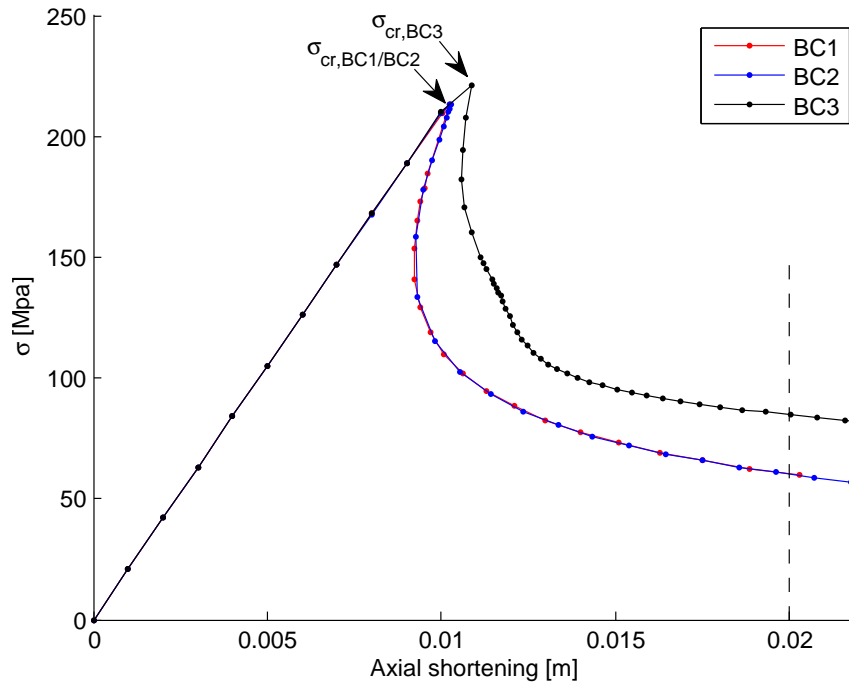


Figure 2.9: Axial shortening versus axial stress for the GMNA with BC1, BC2 and BC3. The dashed line represents the axial shortening where the displacement fields in Figure 2.10 are extracted.

From Figure 2.9 it is clear that the equilibrium path for BC1 and BC2 are close to identical, while BC3 in general obtains higher stresses, to reach the same axial shortening.

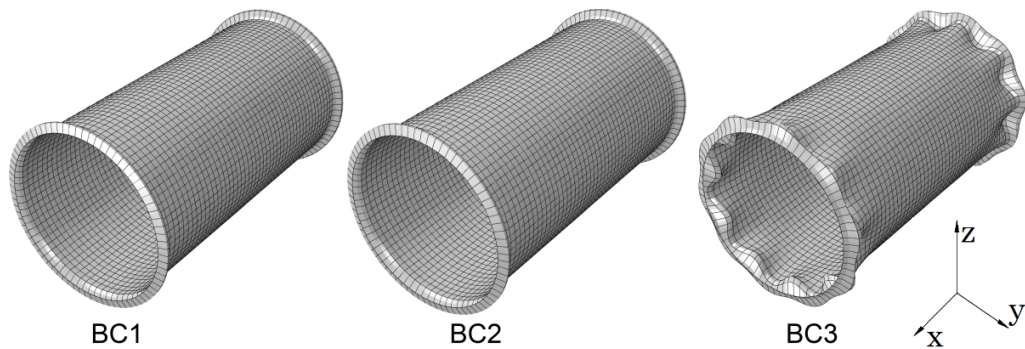


Figure 2.10: Displacement fields obtained through GMNA with BC1, BC2 and BC3. Scale=25

From Figure 2.10, it is seen that the displacement field of the cylinder with BC1 and BC2 are identical. This is also the case for the critical buckling resistances listed in Table 2.4. The cylinder with BC3 develops a wave pattern around the edges, caused by the fix of rotational degrees of freedom at the boundaries. Therefore a larger amount of energy is necessary to cause the same axial shortening, compared to the cylinder with BC1 and BC2, leading to a larger critical buckling resistance.

	BC1	BC2	BC3
σ_{cr} [MPa]	213	213	221

Table 2.4: Critical buckling resistances for the three boundary conditions obtained through GMNA.

Since it is of interest to investigate the influence of geometrical imperfections, a boundary condition which leads to symmetric displacement fields in both the linear bifurcation analysis and the geometrically and materially non-linear analysis is selected. This eliminates BC2, since asymmetry is obtained through the linear bifurcation analysis.

In a real design process, the boundary condition is most likely a mixture of BC1 and BC3 since they are both extremes in relation to rotation. In this thesis, BC1 is selected since it is the most conservative and to ensure buckling rather than yielding in the material.

2.5 Convergence analysis

In this section a convergence analysis will be conducted in order to determine element type and mesh size. Abaqus has several different element types, and since the thickness of the cylinder is significantly smaller than the other dimensions, shell elements are the most reasonable choice of element in this thesis. The shell elements have displacements and rotation degrees of freedom and the thickness is defined through section property definition [Simulia Corp., 2013]. Two different shell element types will be compared in this section, namely the linear *4-node general-purpose shell, reduced integration with hourglass control, finite membrane strains* (S4R) and the quadratic *8-node doubly curved thick shell, reduced integration* (S8R). The two shell elements are visualized in Figure 2.11 and 2.12.

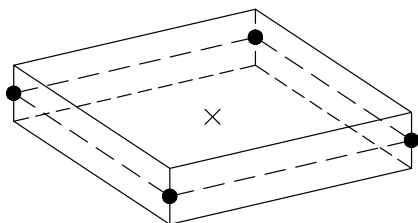


Figure 2.11: S4R element. The black dots represents each node and the cross represents the integration point.

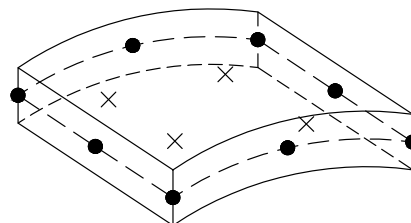


Figure 2.12: S8R element. The black dots represents each node and the crosses represent the integration points.

The convergence analysis is based on the linear bifurcation analysis (LBA) with geometry, material properties and boundary conditions determined in section 2.2, 2.4 and 2.3. The LBA is used due to the reasonable fast computational time and since a specific value for the critical buckling (bifurcation) load is obtained.

Three mode shapes are used in the convergence analysis and named MS1, MS2 and MS3 as shown in Figure 2.13 since they will be referred to several times through the analysis.

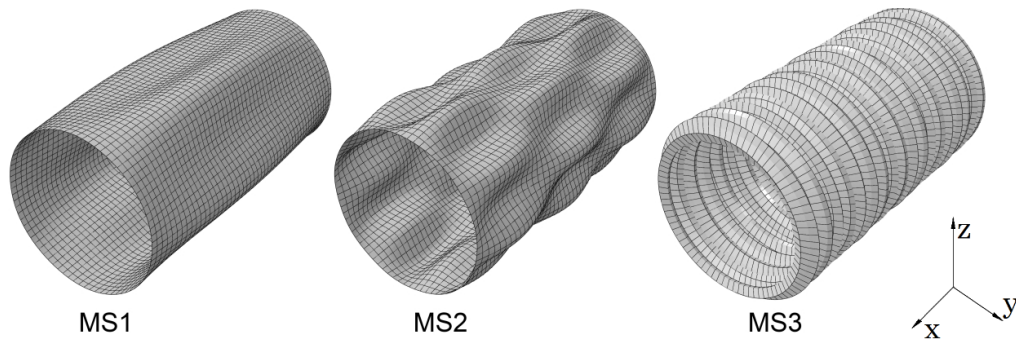


Figure 2.13: Visualization of the three used mode shapes MS1, MS2 and MS3. Scale=0.3.

First an analysis is carried out, where the lowest buckling load *i.e.* the 1st mode is used, thereby neglecting possible mode shifts. The results of this analysis for number of elements and number of nodes with S4R and S8R elements are shown in Figure 2.14 and 2.15.

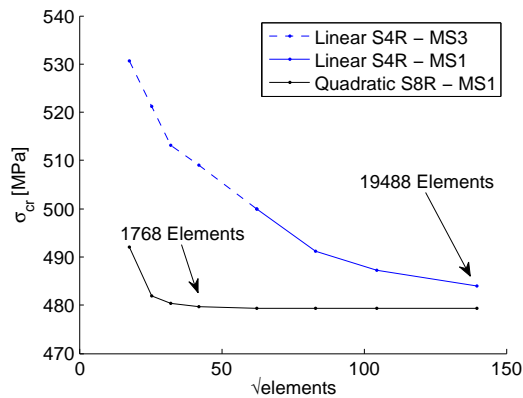


Figure 2.14: Convergence analysis for S4R and S8R elements with varying number of elements. All values are extracted from the 1st mode.

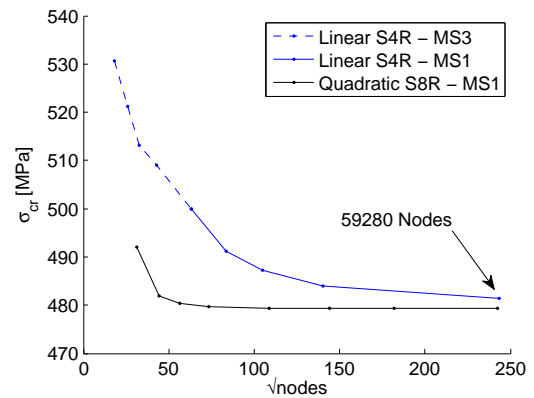


Figure 2.15: Convergence analysis for S4R and S8R elements with varying number of nodes. All values are extracted from the 1st mode.

From Figure 2.14 and 2.15 it can be concluded that the linear S4R elements not are converged, even with use of 59280 nodes. Additionally a mode shift is observed, visualized by the shift between the dashed and solid blue lines corresponding to a mode shift between MS3 and MS1. The two mode shapes are shown in Figure 2.16 and 2.17.

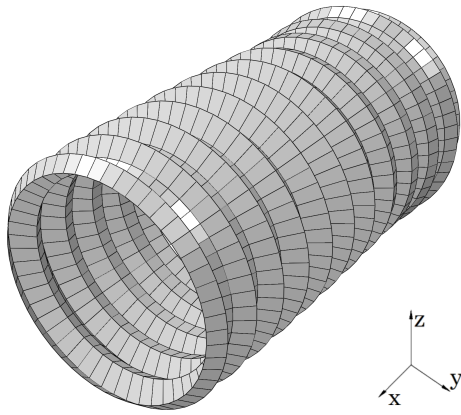


Figure 2.16: MS3 calculated with LBA using 1768 S4R elements. Scale=0.3.

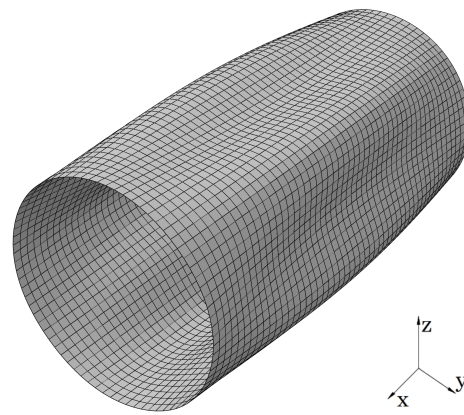


Figure 2.17: MS1 calculated with LBA using 3900 S4R elements. Scale=0.3.

It is clear that the mode shapes are highly non-linear and therefore a large amount of linear elements is necessary. In contrast to this, the quadratic S8R elements are converged at 1768 elements and will therefore be the preferred element.

To ensure that the mesh is sufficiently fine, a higher order mode (MS2) is chosen for comparison, see Figure 2.18.

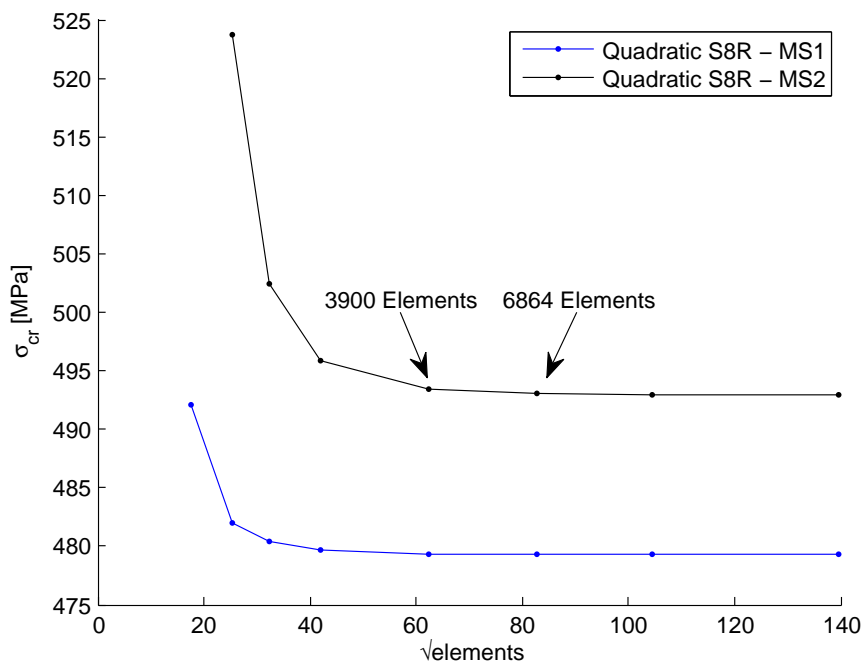


Figure 2.18: Convergence analysis for S8R elements with mode shape MS1 and MS2.

It is seen that more elements (3900) are needed for the model to converge. To ensure that the model is accurate at higher modes, a more refined mesh should be considered, but due to the computational time difference for the LBA (117s with 3900 elements and 212s with 6864 elements) a mesh size of 3900 elements is selected.

In the following a summarisation of the finite element model will be given.

2.6 Model summary

A summary of the selected analysis parameters from previous sections are listed in Table 2.5 and a flow diagram which shows the connection between Matlab, Python and Abaqus is shown in Figure 2.19. The reason for this approach is that it is of interest to calculate multiple numerical models, where properties, such as the imperfection amplitude, are changed several times, and therefore a large amount of time can be saved, since it is not necessary to reconstruct the model in Abaqus each time.

FEA solver	Abaqus version 6.13
Non-linear algorithm	Riks method
Element type	S8R
Number of elements/nodes	3900/11856
Element size	0.2 m·0.2 m
Integration points per element	4
Boundary condition	BC1, see Figure 2.7 on page 19
Length	10 m
Radius	2.5 m
Thickness	0.01 m
Young's modulus	$210 \cdot 10^9$ Pa
Poisson's ratio	0.3
Yield stress	$235 \cdot 10^6$ Pa

Table 2.5: Analysis parameters along with characteristic material and geometrical values used in the numerical model.

The flow diagram is made in order to facilitate the understanding of the connection between the used programs. The following steps, corresponding to the steps in Figure 2.19, are used in the approach;

1. A main script is written in Matlab, where all properties that needs to vary are defined. This could for instance be r, t, l, f_y, E, ν etc.
2. The properties are printed to a Python file (*Input.py*), which is the program language used in Abaqus.
3. A Python file (*MDB.py*) is written by editing the *Model Database* file created from the *Graphical User Interface* in Abaqus. This file contains all information about the model, and therefor it uses (*Input.py*) from step (2) as input.
4. A Python file (*ODB.py*) is written by editing the *Output Database* file created from the *Graphical User Interface* in Abaqus. This file contains information about which results that subsequently will be printed in step (6).
5. In this step, Abaqus is executed from the main file in step (1) and uses (*Input.py*) and (*MDB.py*) to create the model which is then analysed.
6. The result file is printed from the information given in (*ODB.py*).
7. The results are saved/plotted in the main file. The whole process is repeated i times.

The above procedure applies to a model with perfect geometry. If imperfections needs to be applied to the model, the following steps are introduced.

- 1*. A model is created in the *Graphical User Interface* in Abaqus with a wanted imperfection pattern.
- 2*. The displacement field of the model in step (1*) is extracted and saved in a (*IMP.fil*)
- 3 . Step (2*) and (2) are implemented in (3) and the process is similar to the one above.

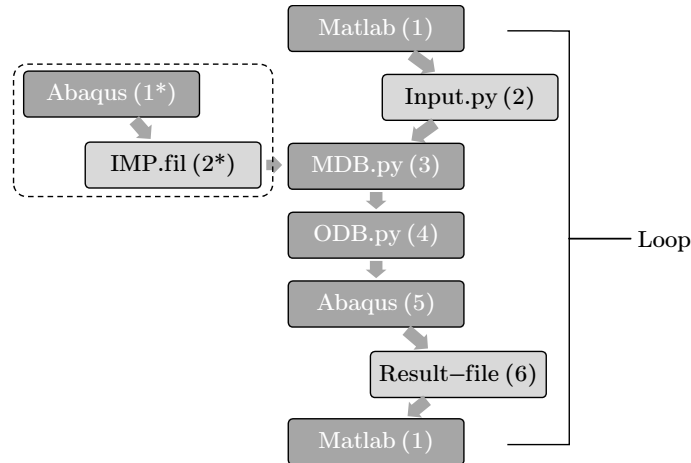


Figure 2.19: Flow diagram which shows the connection between Matlab, Python and Abaqus. The dashed area shows an example of implementing imperfections.

The following chapter presents three ways of simulating geometric imperfections, where the preceding finite element model will be used. The imperfection patterns are inspired by the methods presented in the state-of-the-art review on page 12 and throughout the chapter, different imperfection amplitudes will be investigated.

3 Simulation of Imperfections

In this chapter it will be determined in which way the geometric imperfections will be implemented to the model described in chapter 2.

In the field of buckling of shell structures, numerous ways of implementing geometrical imperfections has been carried out. According to [Schmidt, 2000] three ways of implementing geometrical imperfections are thinkable;

- “Realistic” geometric imperfections
- “Stimulating” geometric imperfections
- “Worst” geometric imperfections

To simulate “Realistic” geometric imperfections, it is in principle necessary to scan the geometry for each model, and implement this in the FE model. When a sufficient number of measurements has been made, it is possible to model the imperfections stochastically, which is also carried out by [De Paor et al., 2012]. This approach however, is not economically viable to a civil engineering shell structure.

“Stimulating” geometric imperfections are simulated by starting from the failure mode of the perfect shell, *i.e.* the results of a GMNA. The pattern of this analysis reveals the weak points of the structure and the idea is to create an initial deformation at these points. This method however, is more appropriate, if several load cases are investigated.

The basic idea of “Worst” geometric imperfections is to implement a geometric imperfection that gives the lowest buckling resistance. In this thesis, weight will be put on these “Worst” geometric imperfections and primarily three approaches will be investigated, namely the linear buckling mode-shaped imperfection (LBMI), the single perturbation displacement imperfection (SPDI) and two perturbation displacements imperfection (TPDI). [DS/EN-1993-1-6, 2007] suggests that the LBMI approach is used, unless other unfavorable patterns can be justified, and is therefore selected as a way of implementing geometric imperfections. The SPDI (and TPDI) approach is selected rather than the SPLI (TPLI) approach investigated by [Castro et al., 2013], since it is more convenient to compare imperfection amplitudes of the LBMI and the SPDI. The difference between SPDI and SPLI is the use of a displacement rather than a load to cause the perturbation of the geometry.

In the end of this chapter, a comparison of the different approaches and results will be conducted.

3.1 Geometrical perfect cylinder

In order to have a reference value, *i.e.* a critical buckling resistance for a model without imperfections, a geometrically and materially non-linear analysis (GMNA) is carried out. Figure 3.1 shows axial shortening versus axial stress for the GMNA, and three points are highlighted to visualise the displacement fields shown in Figure 3.2.

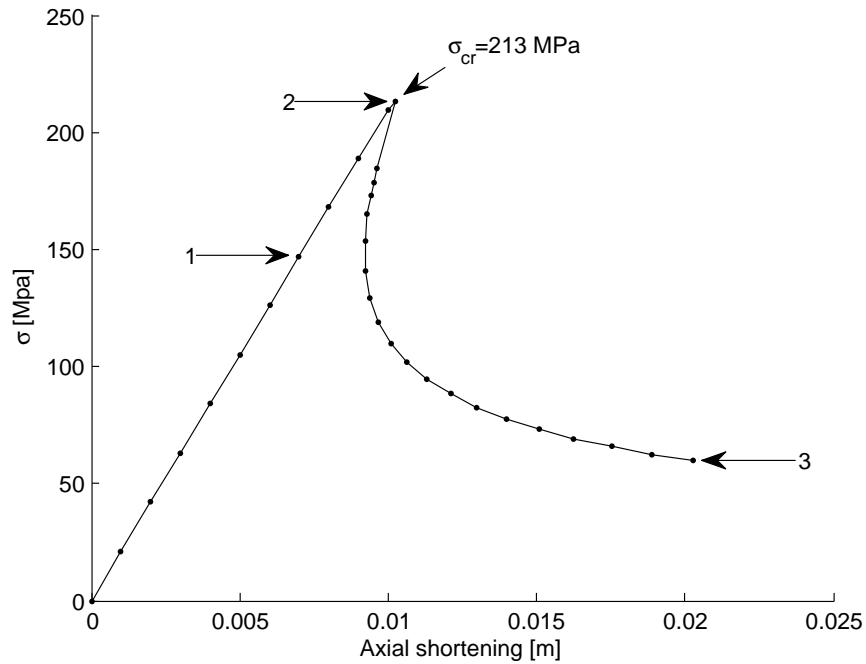


Figure 3.1: Axial shortening versus axial stress for the GMNA. The three points are selected to visualize the displacement fields in Figure 3.2.

First a stable equilibrium path is observed at (1) in Figure 3.1 and corresponds to the displacement field in Figure 3.2 (1). At (2) the cylinder reaches the critical buckling resistance and the deformations begins to concentrate at the edges. At (3) large deformations is observed at the edges.

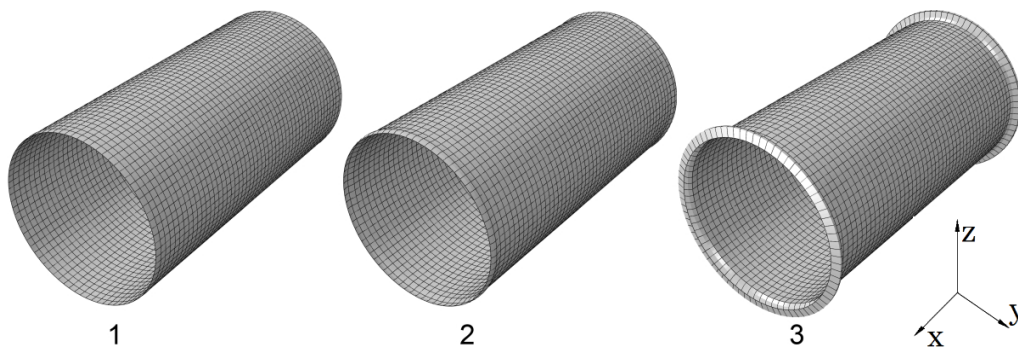


Figure 3.2: Displacement field obtained through GMNA corresponding to point 1, 2 and 3 in Figure 3.1. Scale=25.

3.2 Geometrical imperfections by means of linear buckling mode-shapes

To implement linear buckling mode-shaped imperfections, two steps are needed. First a LBA is performed, and displacements from a given mode is extracted. These displacements are then implemented as initial geometric imperfections in a fully non-linear analysis (GMNIA).

3.2.1 LBA

A linear bifurcation analysis is performed to obtain the mode shapes of the first 35 modes. Each of the mode shapes are visualised in Appendix C and will in the following section be implemented as geometric imperfections in a GMNIA. The critical buckling resistances obtained through linear bifurcation analyses, are shown in Figure 3.3, while the three selected mode shapes corresponding to the red bars, are shown in Figure 3.4.

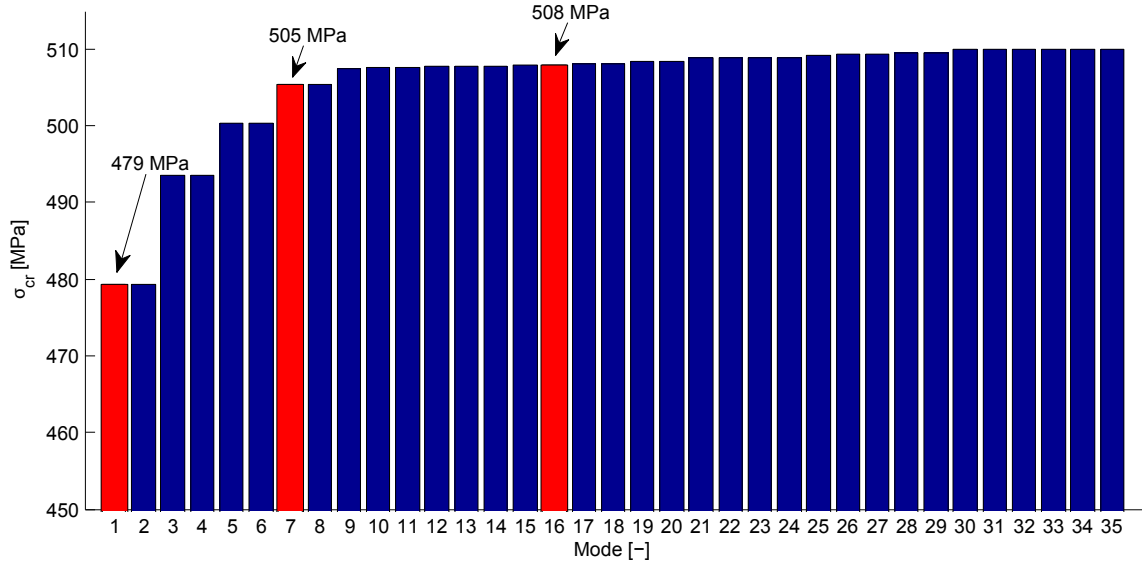


Figure 3.3: Critical buckling resistance for 35 eigenmodes obtained through LBA. Red bars indicate modes for further investigation.

From Figure 3.3, it is observed that the mode shapes appear in pairs, which is caused by symmetry. This is also clearly visualised in Appendix C. From mode 1 to mode 7, the critical buckling resistance is increased from ≈ 480 MPa to ≈ 505 MPa, corresponding to an increase of 5%. However, another development is observed from mode 9 to mode 35, where only a slight increase in the critical buckling resistance is observed. These results indicates that a unique critical buckling resistance is difficult to select, due to the relatively similar values, which also is mentioned in section 1.2 on page 9.

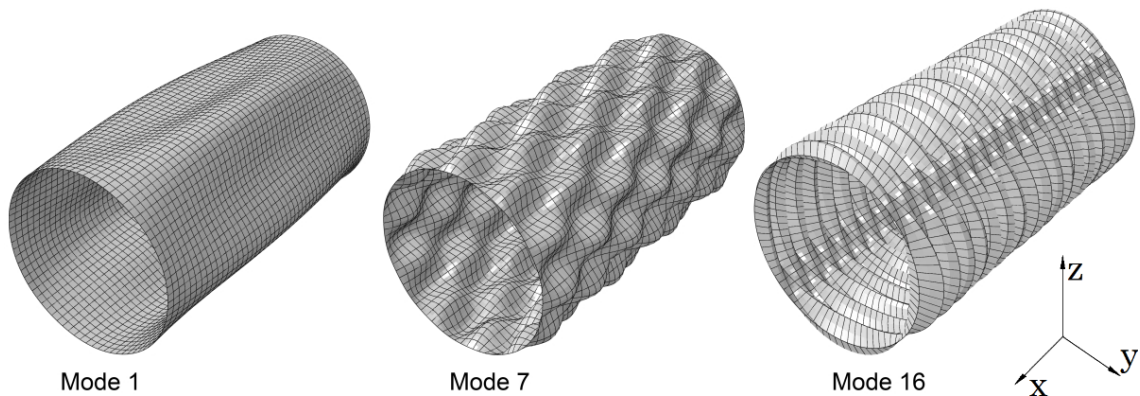


Figure 3.4: Mode shapes obtained from LBA for mode 1,7 and 16. Scale=0.3.

3.2.2 GMNIA

An analysis is performed to identify which of the 35 mode shapes obtained through the linear bifurcation analysis, when implemented as geometrical imperfections, has the lowest buckling resistance. For convenience purposes, the imperfection amplitude w_0 is, in the following, normalised for the thickness t . In the present analysis w_0/t is selected to 1, *i.e.* corresponding to a maximum displacement of one wall thickness. Results of this analysis are shown in Figure 3.5.

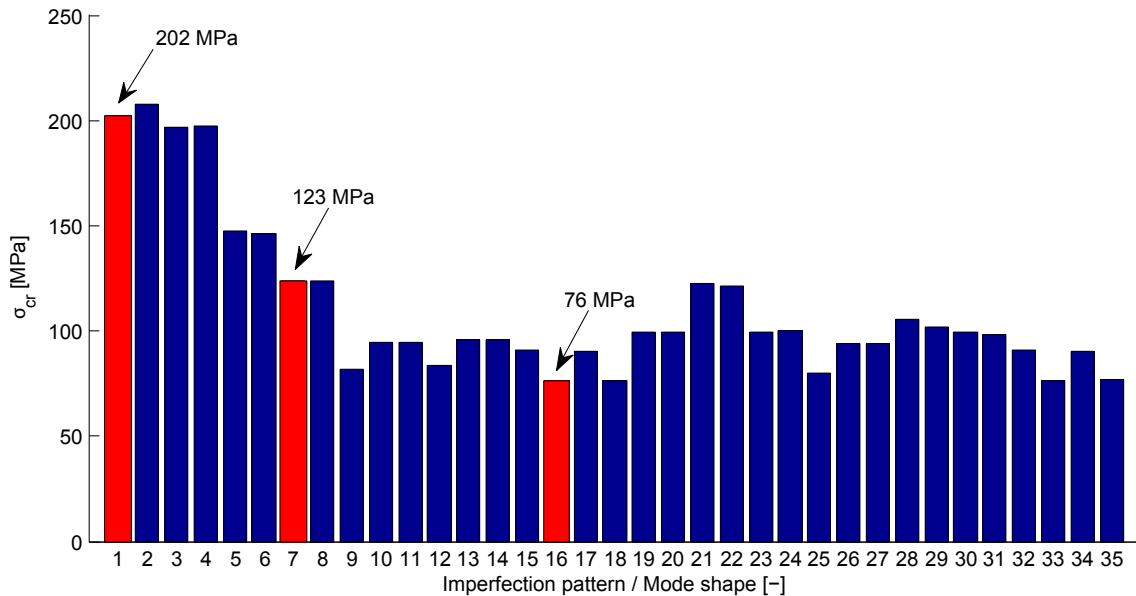


Figure 3.5: Critical buckling resistance obtained through GMNIA with constant imperfection amplitude $w_0/t = 1$. The initial geometric imperfection pattern is obtained from the first 35 eigenmodes obtained through LBA. Red bars indicate mode shapes for further investigation.

A large variety is observed, meaning that it is of great influence which mode is chosen, to represent the initial imperfections. To investigate the influence of the selected imperfection amplitude w_0 three mode shapes are chosen (1,7,16), represented by the red bars in Figure 3.5.

The buckling point is defined by the crosses shown in Figure 3.6, which corresponds to the maximum. It is assessed that the three mode shapes chosen, represent all 35 mode shapes, *i.e.* has a fairly similar equilibrium path as the rest of the 32 mode shapes. Furthermore it is seen that the pre- and post buckling paths depend highly on the mode shape selected as initial geometric imperfection.

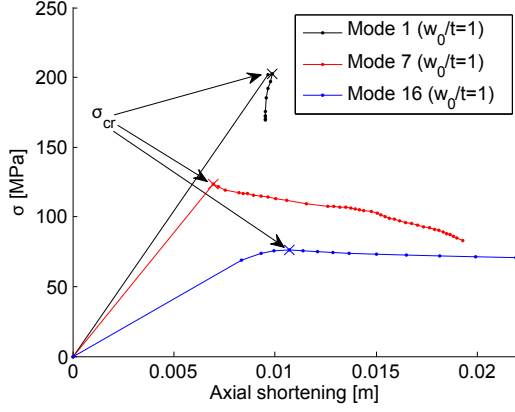


Figure 3.6: Axial stress versus axial shortening with imperfection amplitude $w_0/t = 1$.

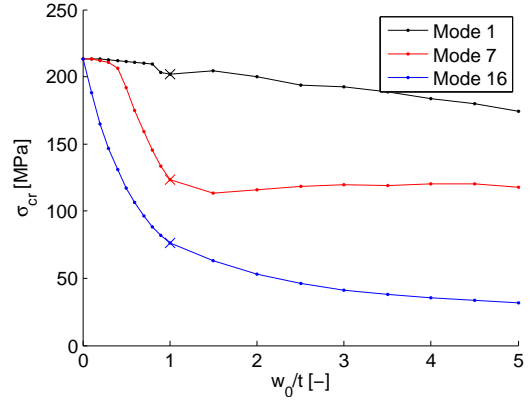


Figure 3.7: Critical buckling resistances with increasing imperfection amplitude for mode shape 1, 7 and 16.

Critical buckling resistances σ_{cr} versus imperfection amplitudes normalised for the thickness w_0/t are plotted in Figure 3.7. It is observed that w_0 at mode shape 1 has a minor effect on the buckling resistance compared to mode shape 7 and 16. Even with $w_0/t = 0.2$ at mode shape 16, a lower buckling resistance is observed than with $w_0/t = 5$ at mode shape 1.

To visualize the displacement field of the cylinder, three points (shown in Figure 3.8) are extracted from the equilibrium path for mode shape 16 in Figure 3.6.

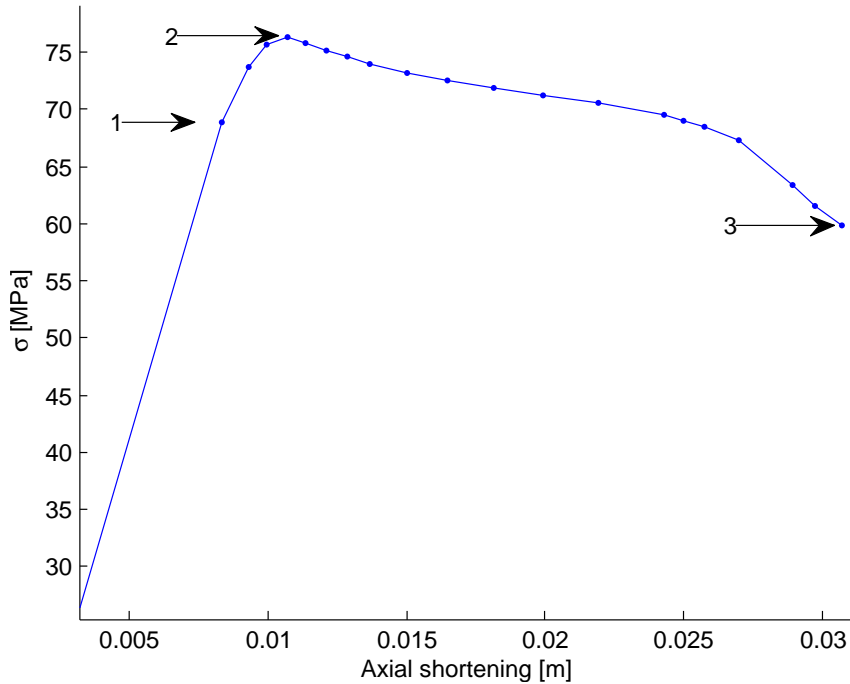


Figure 3.8: Axial shortening versus axial stress for mode shape 16 with $w_0/t = 1$. The three points are selected to visualize the displacement fields in Figure 3.9.

Figure 3.9 shows the displacement fields of the cylinder for each of the three points. First a stable equilibrium path is observed in Figure 3.8 and corresponds to the displacement field in Figure 3.9 (1), until a bifurcation point occurs at (2). At the last point (3) the

displacement field resembles a mixture of mode shape 1 and 16. This shows that the cylinder, even with mode shape 16 as initial imperfection, transforms into a displacement field, which shows traces of both mode shape 1 and 16. Furthermore the displacements are concentrated at the boundaries, which indicates the importance of the modeled boundary conditions.

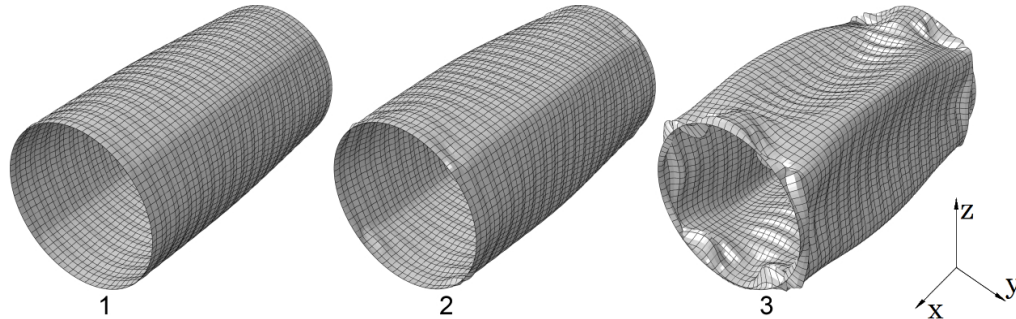


Figure 3.9: Displacement field corresponding to point 1, 2 and 3 in Figure 3.8. Scale=10

3.3 Geometrical imperfections by means of a single perturbation displacement

Similar to the linear buckling mode-shaped imperfection, two steps are needed to implement the single perturbation displacement imperfection. First a point displacement is applied as shown in Figure 3.11, and a static calculation with geometrically and materially non-linear theory is performed. Secondly the displacements for the whole model are extracted, visualised in Figure 3.10, and are then implemented as initial geometric imperfections in a geometrical and material non-linear analysis (GMNIA).

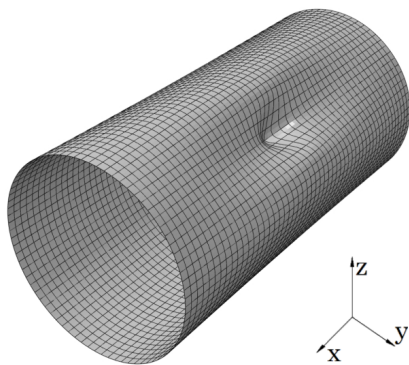


Figure 3.10: Initial displacement field for the single perturbation displacement with $w_0/t = 5$ and scale=20.

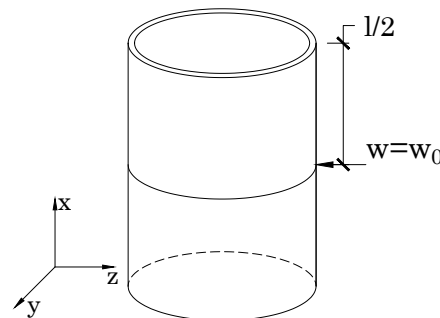


Figure 3.11: Position of applied displacement for the single perturbation displacement.

To show the effects of the single perturbation displacement imperfection on the geometry, displacements of the circumferential and meridional directions are shown in Figure 3.12 and 3.14 respectively. It is seen that a great part of the geometry is influenced by the single perturbation displacement.

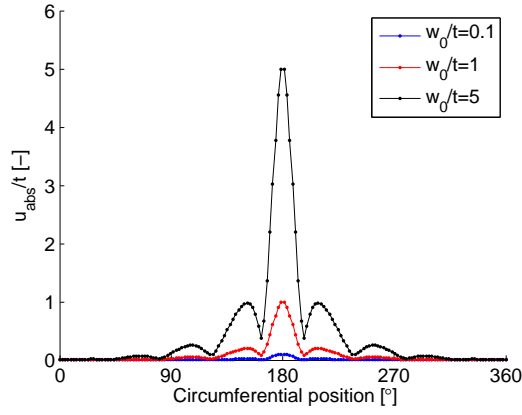


Figure 3.12: Absolute displacements normalised to the thickness in the circumferential direction.

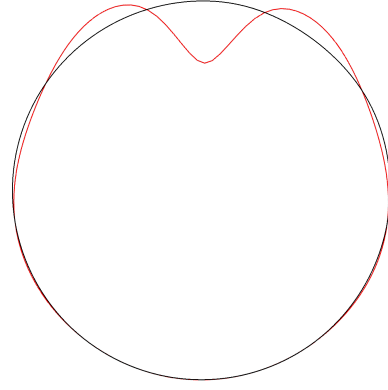


Figure 3.13: Principle sketch of undeformed (black) and deformed (red) circumferential cross section.

A principle sketch of the undeformed and deformed cross section in the circumferential direction is shown in Figure 3.13.

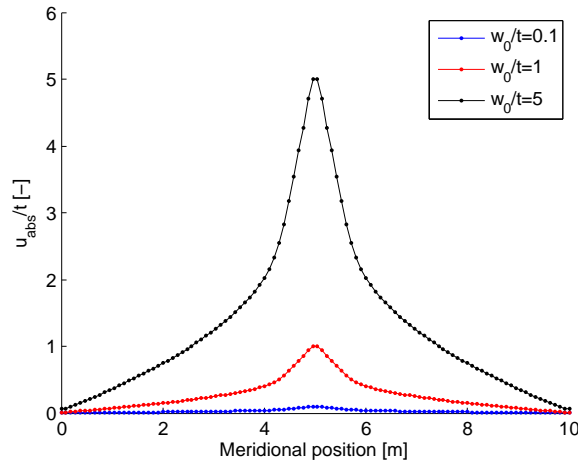


Figure 3.14: Absolute displacements normalised for the thickness in the meridional direction.

In contrast to the equilibrium paths obtained using linear buckling mode-shaped imperfections, the equilibrium path is more complex *i.e.* one or more local maxima occur, as shown in Figure 3.15. This makes the buckling point more difficult to define, and it is chosen to use the first maximum as critical buckling resistance, shown by the blue cross.

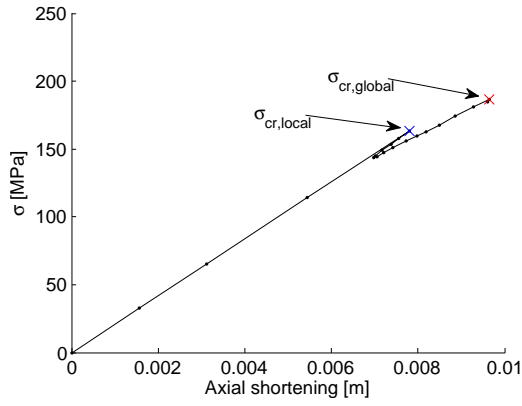


Figure 3.15: Axial stress versus axial shortening with imperfection amplitude $w_0/t = 1.5$. The cross represents the selected critical buckling point.

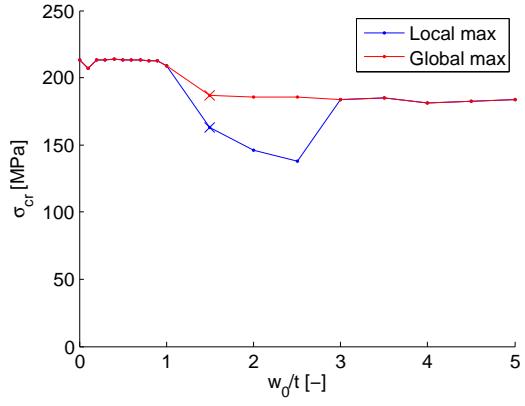


Figure 3.16: Critical buckling resistance versus imperfection amplitude normalised for the thickness. Values are extracted for the first maximum and the global maximum.

Critical buckling resistances σ_{cr} versus imperfection amplitudes w_0/t are plotted in Figure 3.16. From the figure it is observed that a rather high imperfection amplitude is needed ($w_0/t \geq 1$) to influence the critical buckling resistance. However in the range of $w_0/t = [1; 3]$ a high reduction is observed. When $w_0/t \geq 3$ a constant critical buckling resistance, corresponding to a 15% reduction of the critical buckling resistance compared to $w_0/t = 0$, is observed.

Six points (shown in Figure 3.17) are extracted from the equilibrium path in Figure 3.15, to visualise the displacement fields of the cylinder in Figure 3.18.

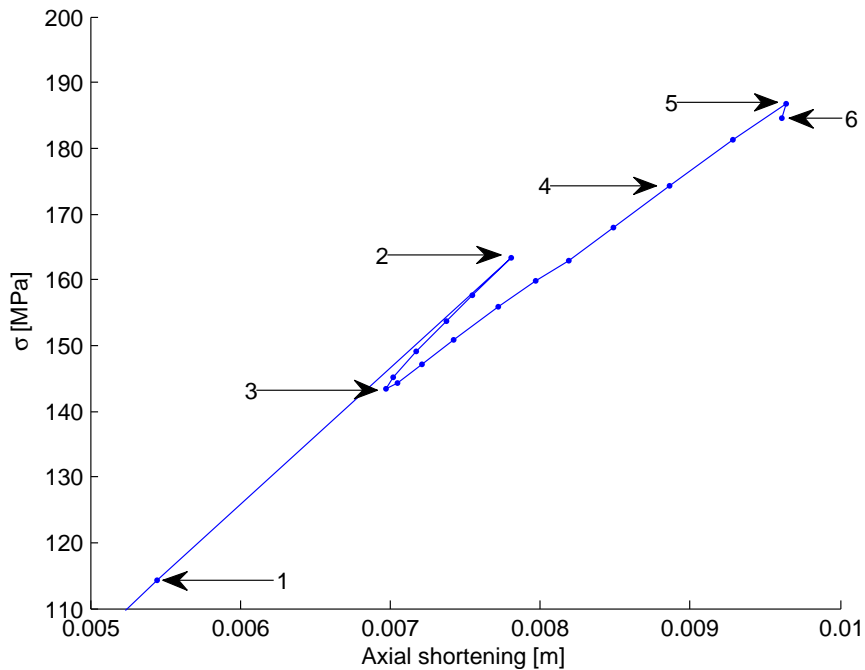


Figure 3.17: Axial stress versus axial shortening for a single perturbation displacement imperfection with $w_0/t = 1.5$. The six points are selected to visualize the displacement fields in Figure 3.18.

From the displacement fields in Figure 3.18, it can be observed that a major part of the

displacements are observed around the initial imperfection. In contrast to the displacement field in Figure 3.9, the single perturbation displacement imperfection does not cause any other displacement field than the one initially given. It should be noted that the selected critical buckling point corresponds to (2).

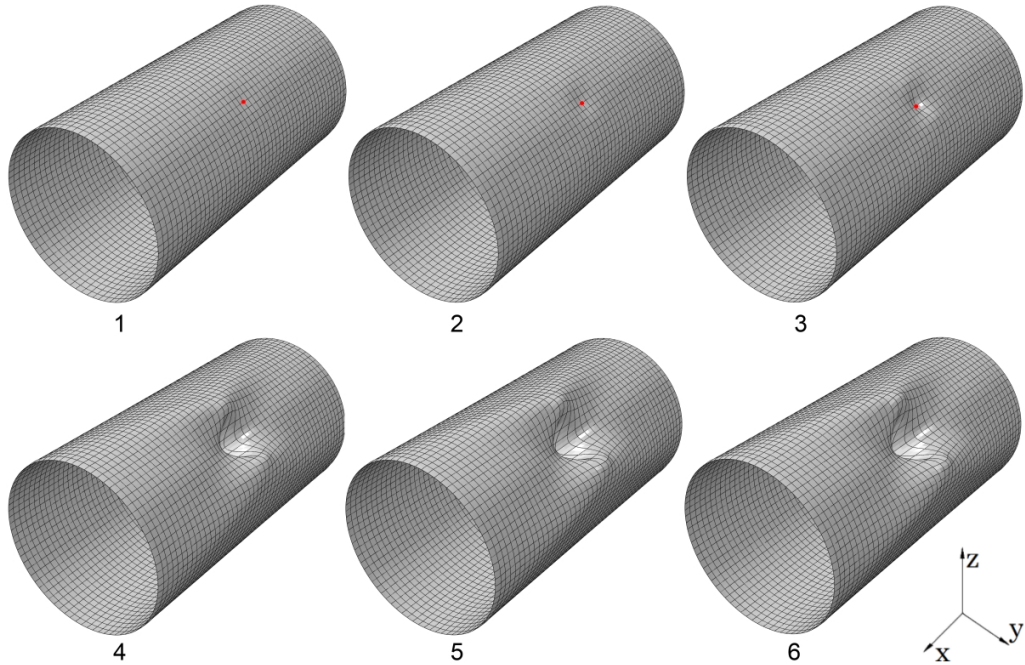


Figure 3.18: Displacement field corresponding to point 1, 2, 3, 4, 5 and 6 in Figure 3.17. The red dots represent the positions of the initial perturbation displacements. Scale=25.

3.4 Geometrical imperfections by means of two perturbation displacements

In this section, the effect of adding two initial displacement imperfections is investigated. The procedure is similar to the one described in section 3.3. Two displacements are applied as shown in Figure 3.20, and correspond to the displacement field in Figure 3.19.

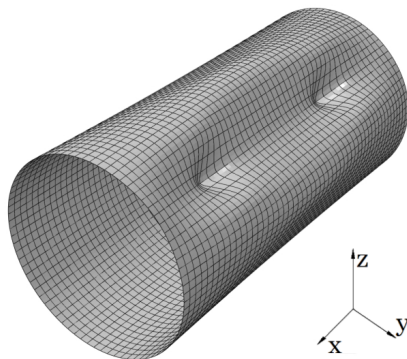


Figure 3.19: Initial displacement field for the two perturbation displacements with $w_0/t = 5$ and scale=20.

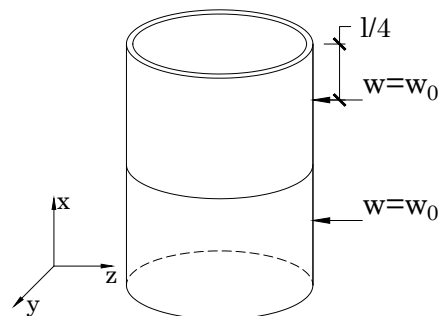


Figure 3.20: Positions of applied displacements for the two perturbation displacement.

Again the effects of the two displacement imperfections on the geometry are visualised by

showing the displacements of the circumferential and meridional directions in Figure 3.21 and 3.22 respectively. It is seen that a great part of the geometry is influenced by the two perturbation displacements.

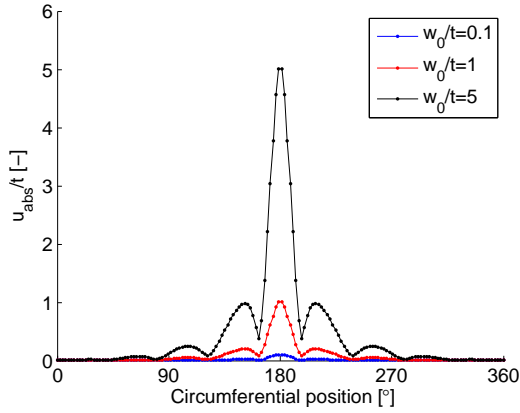


Figure 3.21: Absolute displacements normalised for the thickness in the circumferential direction.

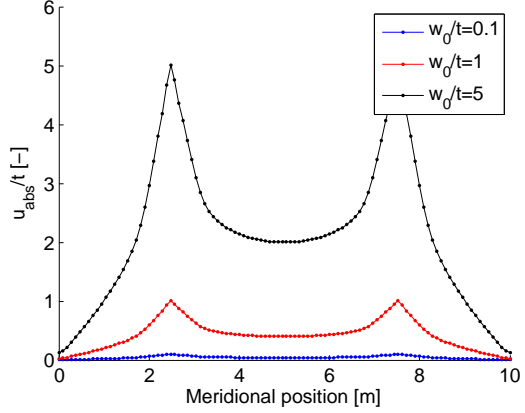


Figure 3.22: Absolute displacements normalised for the thickness in the meridional direction.

The critical buckling resistance is again chosen as the first maximum, shown by the blue cross in Figure 3.23.

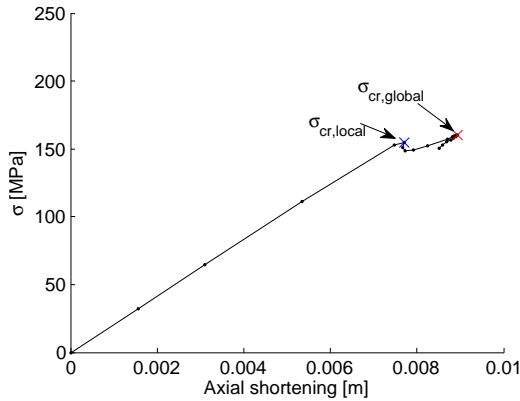


Figure 3.23: Axial stress versus axial shortening with imperfection amplitude $w_0/t = 1$. The cross represents the selected critical buckling point.

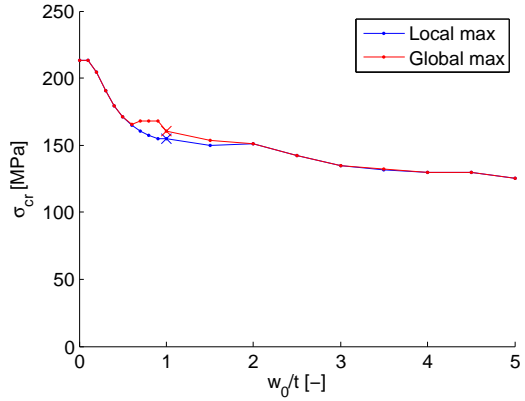


Figure 3.24: Critical buckling resistance versus imperfection amplitude normalised for the thickness. Values are extracted for the first maximum and the global maximum.

In order to investigate the effect of the imperfection amplitudes w_0 , critical buckling resistances σ_{cr} versus imperfection amplitudes w_0/t are plotted in Figure 3.24. It is observed that the imperfection amplitude has a high influence on the buckling resistance for $w_0/t = [0; 1]$ and is reduced with about 30%. The imperfection amplitude has less influence on the buckling resistance for $w_0/t = [1; 5]$ where a reduction of only 5% is observed.

Six points (shown in Figure 3.25) are extracted from the equilibrium path in Figure 3.23, to visualise the displacement fields of the cylinder in Figure 3.26.

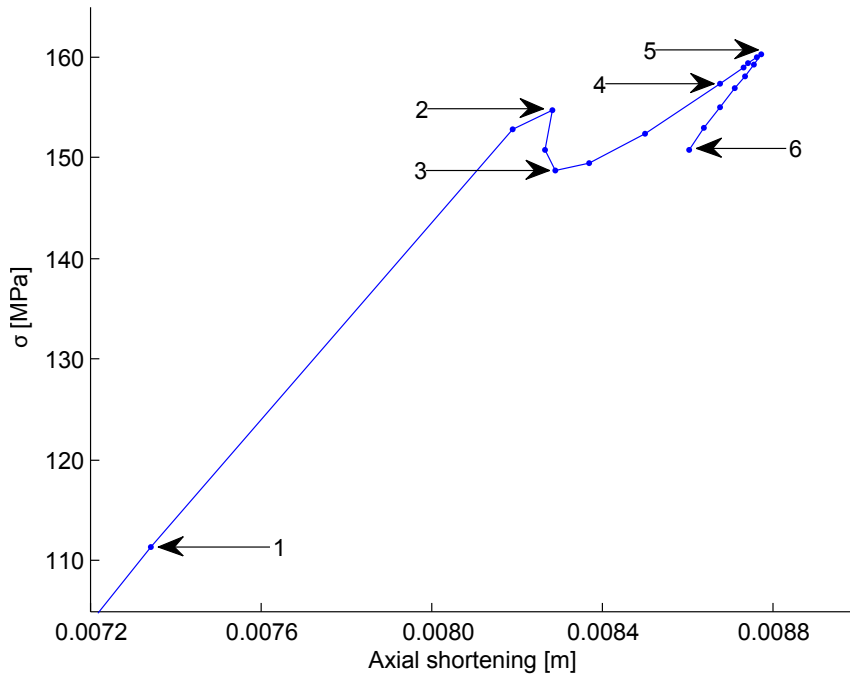


Figure 3.25: Axial shortening versus axial stress for the two perturbation displacement imperfections with $w_0/t = 1$. The six points are selected to visualize the displacement fields in Figure 3.26.

Figure 3.26 shows the displacement fields of the cylinder for each of the six points.

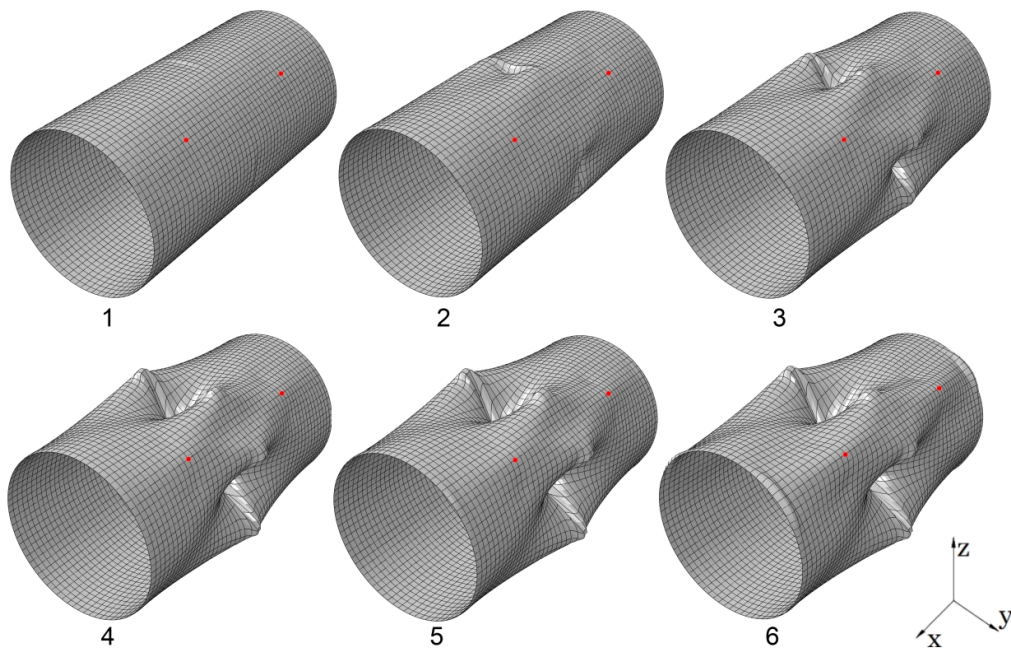


Figure 3.26: Displacement field corresponding to point 1, 2, 3, 4, 5 and 6 in Figure 3.25. The red dots represent the positions of the initial perturbation displacements. Scale=25

First a stable equilibrium path is observed in Figure 3.25 and corresponds to the displacement field in Figure 3.26 (1), until a bifurcation point occurs at (2), which also

is selected as the critical buckling point. At point (3) a local minimum is observed and the cylinder regains strength and follows a stable path through point (4) until it reaches a new bifurcation point (5). At the last point (6) the deformations are now observed at the boundaries. Generally it is observed, in contrast to the single perturbation displacement imperfection, that the displacements does not develop at the position of the initial imperfection, which is unexpected. This leads to the conclusion, it can be very difficult to predict how the cylinder is influenced by the different imperfections.

3.5 Comparison/summarising of imperfections

In this section, the equilibrium path, and thereby the critical buckling resistance, of models with geometric imperfections as presented in section 3.2, 3.3 and 3.4 will be compared. Furthermore the influence on the critical buckling resistance by increasing the imperfection amplitude is compared. The initial geometric imperfection shapes are shown in Figure 3.27.

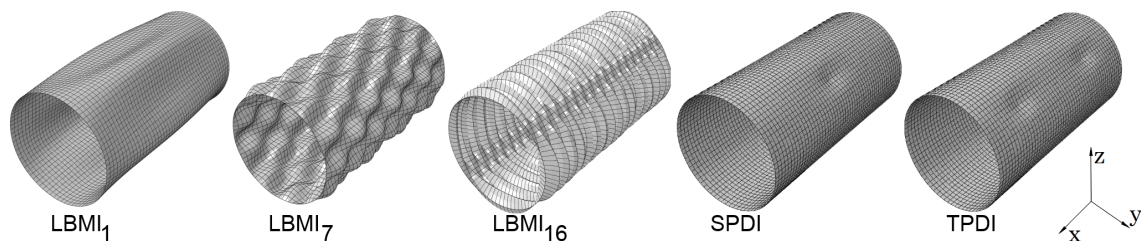


Figure 3.27: Initial geometric imperfection shapes. LBMI₁, LBMI₇ and LBMI₁₆ represents the linear buckling mode shaped imperfection for mode 1, 7 and 16, respectively. SPDI represents imperfections simulated by single perturbation displacement imperfection, while TPDI represents imperfections simulated by two perturbation displacement imperfections. All shapes are scaled corresponding to a maximum displacement $w_0 = 0.3m$.

The equilibrium paths of each numerical model with imperfection amplitude $w_0/t = 1.0$, are shown in Figure 3.28. It is seen that the different methods to simulate geometric imperfections provide a very scattered result. However all models with geometric imperfections give lower critical buckling resistances, compared to the perfect cylinder (GMNA), which is expected. The LBMI for mode 16 gives the lowest critical buckling resistance, and it is observed that the stiffness is reduced dramatically. The LBMI for mode 1 and the SPDI gives results very close to the perfect model, and this indicates that these imperfection patterns does not have a significant effect on the critical buckling resistance.

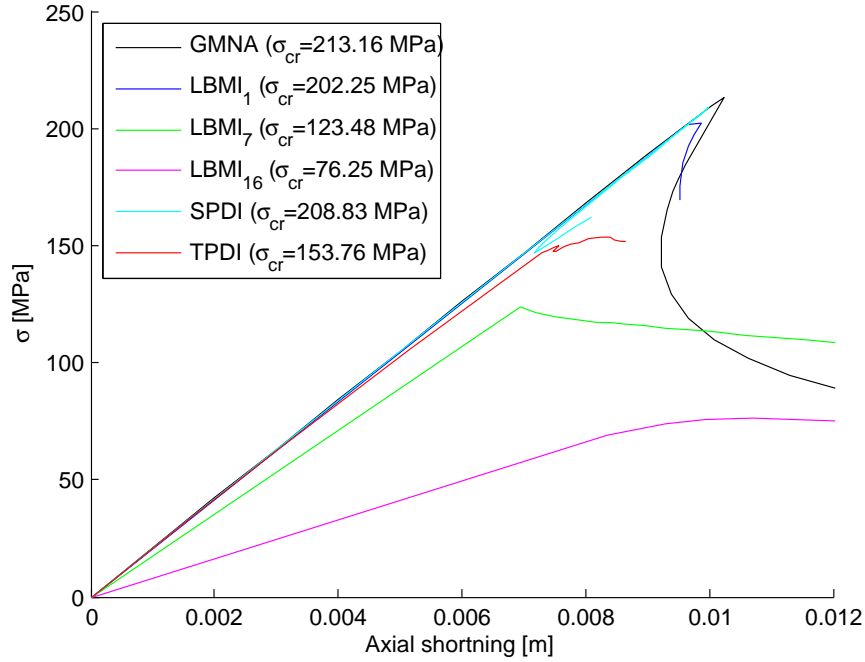


Figure 3.28: Axial stress versus axial shortening with imperfection amplitude $w_0/t = 1.0$ for all the simulated imperfections. GMNA represents the model without imperfections.

The large difference in the critical buckling resistance is caused by the large difference in the initial imperfection pattern. This is clearly visualised by the difference in the initial imperfection pattern between LBMI₁₆ and SPDI in Figure 3.27. With the initial imperfection pattern for LBMI₁₆, almost all of the geometry is changed while only a part is changed in SPDI. This is also reflected in the results of the critical buckling resistance, where a 60% difference is observed.

The critical buckling resistance versus imperfection amplitude for all the simulated imperfections, are shown in Figure 3.29. In general, there are no connection between the five methods. However, similar developments are observed for LBMI₇, LBMI₁₆ and TPD1, where there is a high reduction in the critical buckling resistance in the range $w_0/t = [0; 1]$. This indicates that the critical buckling resistance for these three methods are very sensitive to small imperfections. In contrast to this, it is observed that LBMI₁ and SPDI almost are unaffected by imperfection amplitudes $w_0/t < 1$.

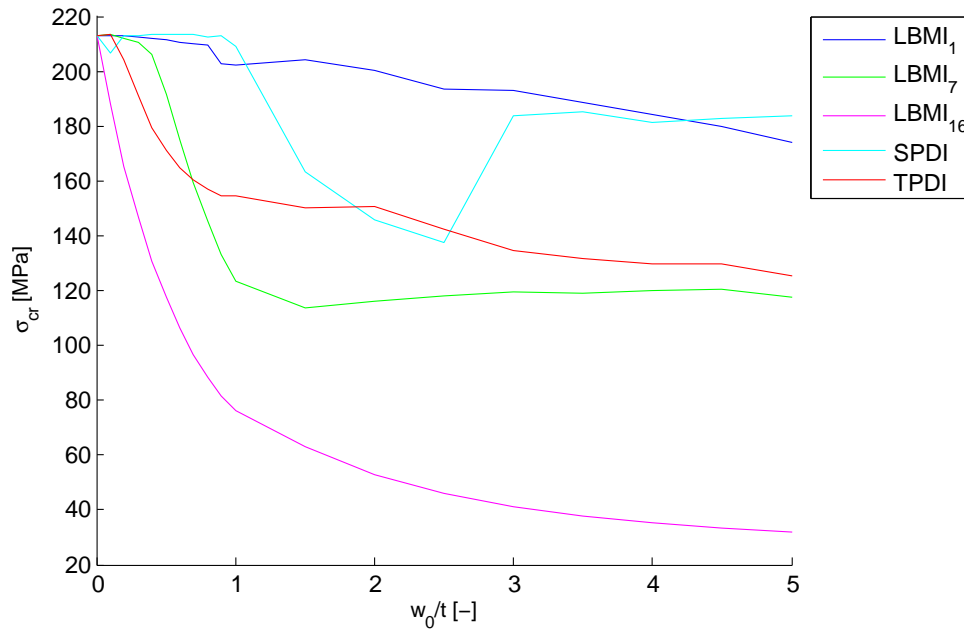


Figure 3.29: Critical buckling resistance versus imperfection amplitude normalised for the thickness for all the simulated imperfections.

Since predicting the behavior of thin cylindrical shell structures is complex, it is necessary to be conservative, when choosing the initial imperfection pattern and the imperfection amplitude. Therefore it is of interest to investigate the uncertainties related to a perfect as well as an imperfect cylinder, and the reliability of the given methods to simulate geometric imperfections.

4 Uncertainties related to the Critical Buckling Resistance

In general, uncertainty related to structures can be divided in four groups, which further can be divided in aleatory and epistemic uncertainty;

- Aleatory uncertainty
 - Physical uncertainty.
- Epistemic uncertainty
 - Model uncertainty.
 - Statistical uncertainty.
 - Measurement uncertainty.

Physical uncertainty is the uncertainty related to the natural randomness of a given quantity, such as the uncertainty in the yield stress due to production variation or the uncertainty of the annual maximum mean wind speed.

Model uncertainty is the uncertainty related to the approximated mathematical models used as well as the uncertainty of the choice of distribution functions used for the stochastic variables.

Statistical uncertainty is the uncertainty related to the limited number of data available and thereby the uncertainty of estimating statistical parameters.

Measurement uncertainty is the uncertainty related to imperfect measurements of physical parameters, such as a geometrical quantity.

These four types of uncertainties are usually used by the reliability methods, which will be presented in the following. Uncertainties like gross errors and human errors are not treated directly in the the reliability methods, but the reliability index will typically depend on, *consequences* and *class of failure*, [DNV-Note-30.6, 2013] and *safety class*, [DS/EN-1990, 2007].

In this thesis, physical uncertainty is accounted for by modeling stiffness- and strength parameters stochastically. The model uncertainty is accounted for by using experimental data from [Batterman, 1965], and in the following, the finite element model used to represent the experimental setup is presented. Statistical and measurement uncertainties are disregarded in this thesis.

4.1 Finite element model representing experimental setup from Batterman

In this section, the model setup from [Batterman, 1965] is presented. In 1965, [Batterman, 1965] studied the plastic buckling of cylindrical shells under axial compression experimentally. The cylindrical shells was made of 2024-T4 aluminum with material and geometrical parameters listed in Table 4.1.

Notation	Symbol	Value	Unit
Young's modulus	E	$0.745 \cdot 10^9$	[Pa]
Poisson's ratio	ν	0.33	[-]
Yield stress	f_y	$415 \cdot 10^6$	[Pa]
Number of specimens	-	17	[-]
Length	l	25 - 50	[mm]
Radius	r	33 - 35	[mm]
Thickness	t	0.3 - 3.5	[mm]
Radius-thickness ratio	r/t	10 - 120	[-]

Table 4.1: Material and geometrical parameters used by [Batterman, 1965].

In the article, the stress-strain curve of the material in compression was obtained by experiments as shown in Figure 4.1. The data is extracted and used in the numerical models.

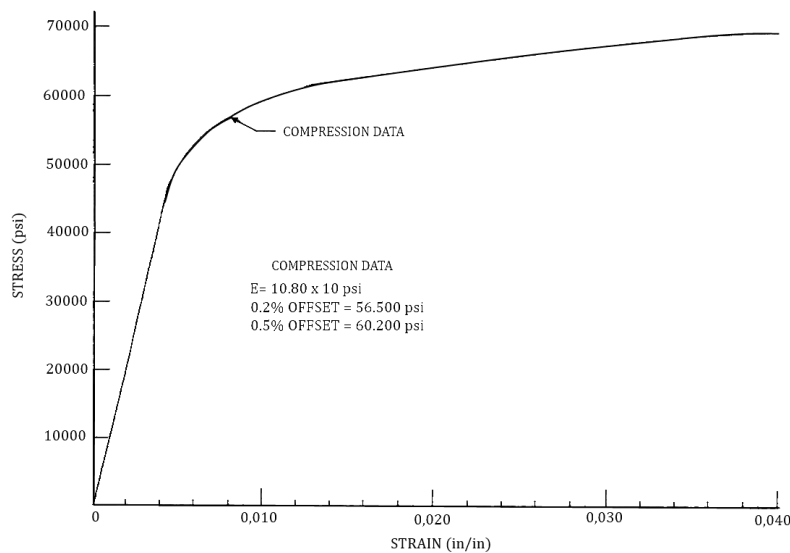


Figure 4.1: Stress-strain curve of 2024-T4 aluminum obtained by [Batterman, 1965]

Three end conditions were used in the article, namely *abrupt*, *tapered* and *uniform*, shown in Figure 4.2. In this section, data will only be extracted for specimens with *uniform* end conditions *i.e.* the specimens are flat ended between smooth bearing blocks.

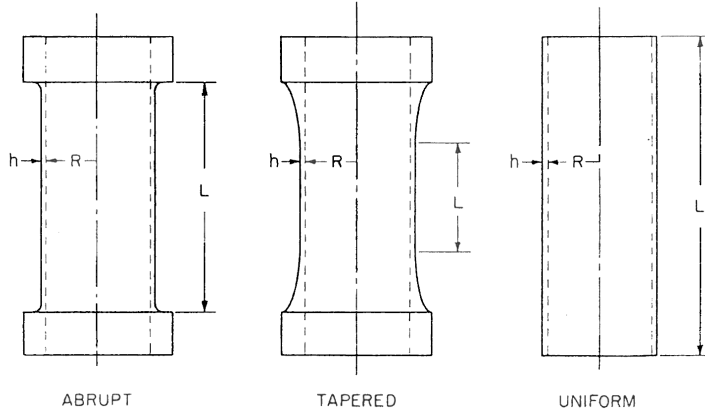


Figure 4.2: Three end conditions presented in [Batterman, 1965].

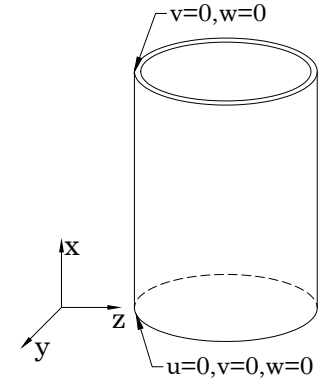


Figure 4.3: Applied boundary conditions similar to uniform.

The uniform boundary condition is applied to the FE model as shown in Figure 4.3, which is similar to BC2 in section 2.4. Parameters used in the FE model, are shown in Table 4.2.

FEA solver	Abaqus version 6.13
Non-linear algorithm	Riks method
Element type	S8R
Number of elements/nodes	Varying
Element size	2 mm·2 mm
Integration points per element	4

Table 4.2: Analysis parameters.

4.2 Estimation of model uncertainty according to DS/EN-1990

In order to take the model uncertainties related to different mathematical models into account, the method in annex D in [DS/EN-1990, 2007] is used.

As mentioned in the history review, the buckling resistance is difficult to describe through a mathematical model. Therefore, it is of interest to calculate the model uncertainty for selected methods, which in this case will be:

- Semi-empirical method suggested by [DS/EN-1993-1-6, 2007]
- Semi-empirical method suggested by [DNV-RP-C202, 2013]
- Geometrically and materially non-linear analysis (GMNA)
- Geometrically and materially non-linear analysis with imperfections (GMNIA)

The semi-empirical method suggested in [DS/EN-1993-1-6, 2007] and [DNV-RP-C202, 2013] are selected in order to compare these two approaches. The GMNA and GMNIA suggested in [DS/EN-1993-1-6, 2007] are selected since they are the methods with highest complexity and are therefore expected to give the lowest model uncertainties.

For a mathematical model h the resistance Y can be written as

$$Y = f(X) \cong X_R h(X, R_1, \dots, R_m) \quad (4.1)$$

where

Y	Buckling resistances
h	Mathematical model
X_R	Model uncertainty
X	Physical parameters
R_1, \dots, R_m	Regression parameters

In the approach suggested by [DS/EN-1990, 2007], annex D, (4.1) is rewritten:

$$Y = f(X) \cong b \Delta h(X) \quad (4.2)$$

where

b	Constant corresponding to the mean value of R_0 (bias)
Δ	Log-normal distributed stochastic variable with mean 1 and standard deviation σ_Δ

Further it is assumed that R_1, \dots, R_m are included in the model $h(X)$.

Test results from [Batterman, 1965] is assumed to be statistical independent and the bias, b , can be estimated using the “Least squares method”

$$b = \frac{\sum_{i=1}^N y_i h(x_i)}{\sum_{i=1}^N h(x_i)^2} \quad (4.3)$$

where

y_i	Realizations of buckling resistances
x_i	Realizations of physical and geometrical parameters

For each test result, a realization of the lognormal distributed variable X_R , is obtained from

$$\Delta_i = \ln \left(\frac{y_i}{b h(x_i)} \right) \quad (4.4)$$

The mean value $\bar{\Delta}$ and standard deviation σ_Δ can be estimated from

$$\bar{\Delta} = \frac{1}{N} \sum_{i=1}^N \Delta_i \quad (4.5)$$

$$\sigma_\Delta = \sqrt{\frac{1}{N-1} \sum_{i=1}^N (\Delta_i - \bar{\Delta})^2} \quad (4.6)$$

Subsequently the coefficient of variation of the model uncertainty can be found

$$V_{\Delta} = \sqrt{\exp(\sigma_{\Delta}^2) - 1} \quad (4.7)$$

In order to visualise the difference between the results obtained, observed buckling resistances in experiments versus estimated buckling resistance from the models has been plotted in Figure 4.4, 4.5, and 4.6. The blue line in the plots represents $b = 1.0$, and the red line represents the calculated bias.

The semi-empirical method suggested by [DS/EN-1993-1-6, 2007] versus the experimental data from [Batterman, 1965] is plotted in Figure 4.4. A fairly high bias is observed, which is expected since the Eurocode is conservative. Additionally it can be observed that non of the points are below $b = 1.0$ corresponding to a safe estimate of the buckling resistance for all tests. Furthermore the coefficient of variation of the model uncertainty is calculated to be $V_{\Delta} = 0.04$, illustrated by the points being closely concentrated around the red line.

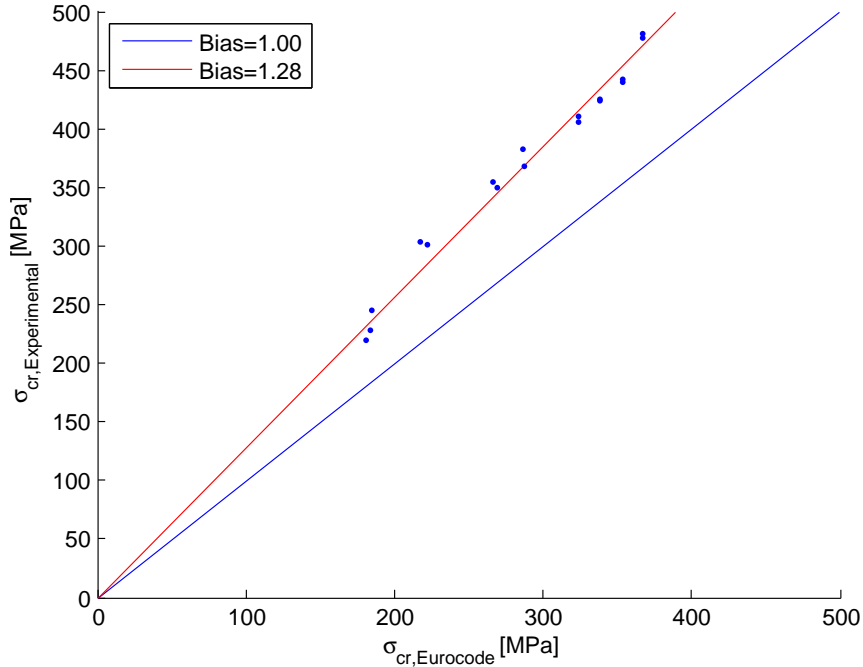


Figure 4.4: Observed buckling resistance in experiments versus estimated buckling resistance from the semi-empirical method suggested by [DS/EN-1993-1-6, 2007]. The coefficient of variation of the model uncertainty $V_{\Delta} = 0.04$.

In Figure 4.5, the semi-empirical method suggested by [DNV-RP-C202, 2013] versus the experimental data from [Batterman, 1965] is plotted. Similar to [DS/EN-1993-1-6, 2007], a fairly high bias is observed, which again is expected. In contrast to [DS/EN-1993-1-6, 2007], the coefficient of variation of the model uncertainty is calculated to $V_{\Delta} = 0.15$, which indicates a higher deviation between the individual points.

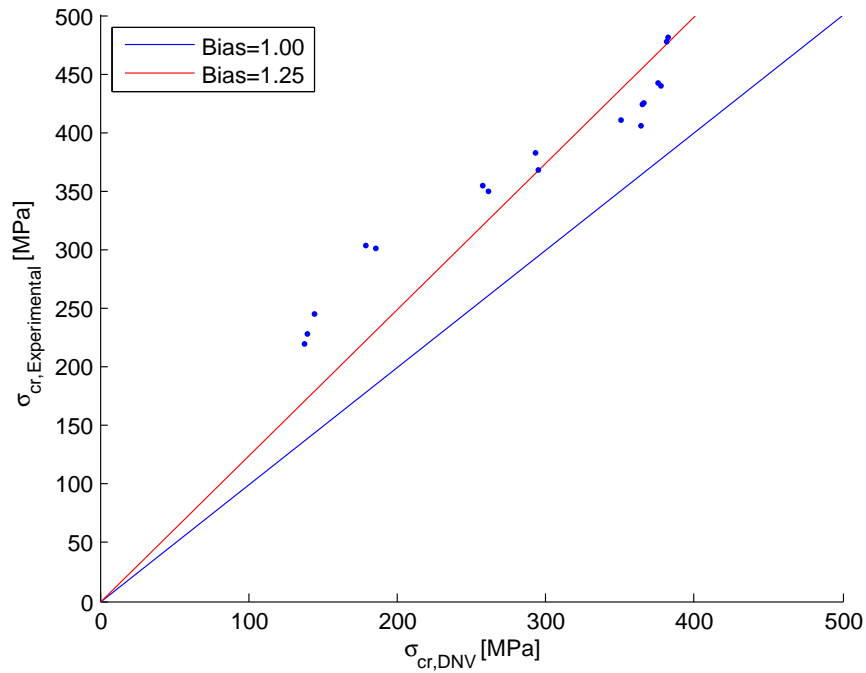


Figure 4.5: Observed buckling resistance in experiments versus estimated buckling resistance from the semi-empirical method suggested by [DNV-RP-C202, 2013]. The coefficient of variation of the model uncertainty $V_{\Delta} = 0.15$.

The numerical GMNA method suggested by [DS/EN-1993-1-6, 2007] versus the experimental data from [Batterman, 1965] is plotted in Figure 4.6. In contrast to the semi-empirical methods, a bias $b = 1.08$ is calculated which is less conservative. The coefficient of variation of the model uncertainty is calculated to $V_{\Delta} = 0.10$, which is highly influenced by the three points below the blue line. In general it is seen that the GMNA is good at predicting the critical buckling resistance, but imperfections are not considered, which could be the reason for the points marked with crosses lying under $b = 1.00$.

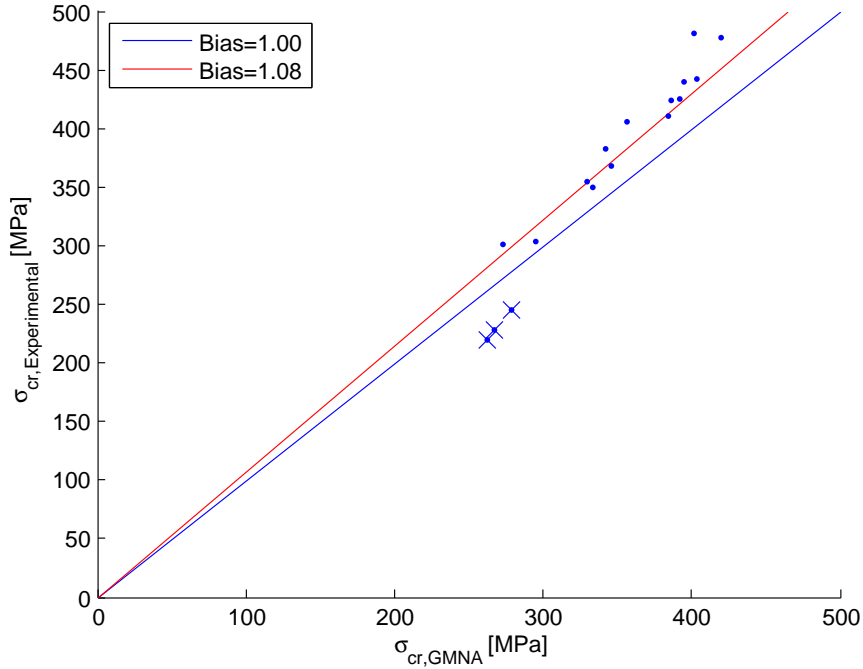


Figure 4.6: Observed buckling resistance in experiments versus estimated buckling resistance from numerical GMNA method suggested by [DS/EN-1993-1-6, 2007]. The coefficient of variation of the model uncertainty $V_{\Delta} = 0.10$. The crosses refers to test specimens with $r/t > 100$

Results from the models are shown in Table 4.3.

Model	b	V_{Δ}
Eurocode 1993-1-6	1.28	0.04
DNV-RP-C202	1.25	0.15
GMNA	1.08	0.10

Table 4.3: Bias b and coefficient of variation of the model uncertainty V_{Δ} for the three selected models.

It is investigated whether there is a relation between the three points below the blue line, and it is observed that they all have a r/t higher than 100, illustrated in Figure 4.7.

To take into account the length l of the test specimens, the *Batdorf-parameter*, Z is introduced;

$$Z = \sqrt{(1 - \nu^2)} \frac{l^2}{rt} \quad (4.8)$$

The normalised buckling resistance versus Z is plotted in Figure 4.8. It is concluded that the length has little influence on the buckling resistance.

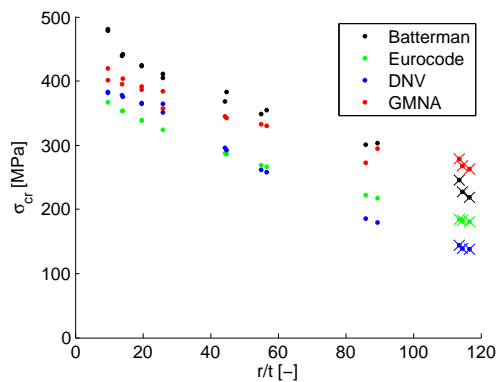


Figure 4.7: Observed buckling resistance in experiments versus r/t . The crosses refers to test specimens with $r/t > 100$

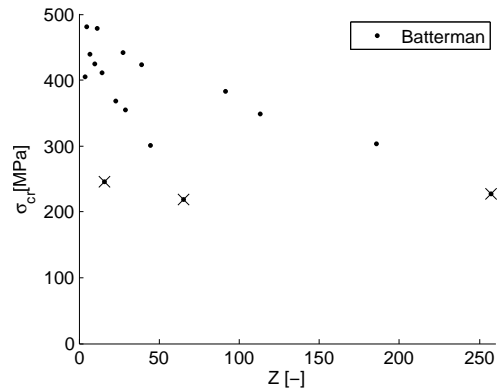


Figure 4.8: Observed buckling resistance in experiments versus Z . The crosses refers to test specimens with $r/t > 100$

To create an even better numerical model, a numerical GMNIA method suggested by [DS/EN-1993-1-6, 2007] is implemented on test specimens with r/t higher than 100. However, the remaining test specimens with r/t lower than 100 will not be given an initial imperfection, but will be similar to results obtained through the GMNA. The geometry and critical buckling resistance of the three test specimens, obtained by [Batterman, 1965], are listed in Table 4.4.

	l [mm]	r [mm]	t [mm]	r/t [-]	$\sigma_{cr,Experimental}$ [MPa]
Cylinder 3	50.80	33.17	0.29	114.56	227.73
Cylinder 4	25.40	33.17	0.28	116.61	219.05
Cylinder 5	12.70	33.18	0.29	113.60	245.45

Table 4.4: Geometrical parameters for the three test specimens with r/t higher than 100, along with $\sigma_{cr,Experimental}$.

The linear buckling mode-shaped imperfection (LBMI) is used to simulate the imperfections. First the lowest critical buckling resistance of the first 35 modes is obtained through a geometrically and materially non-linear analysis with an imperfection amplitude $w_0/t = 1$, shown in Figure 4.9, 4.10 and 4.11.

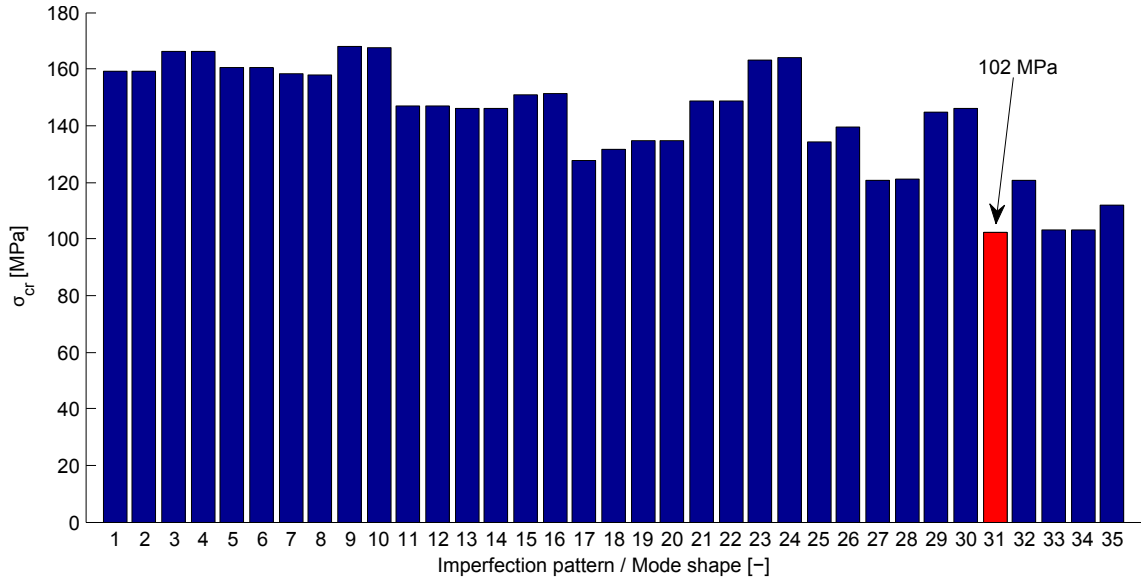


Figure 4.9: Critical buckling resistances for 35 eigenmodes obtained through GMNIA. The analysis is performed for cylinder 3, with constant imperfection amplitude $w_0/t = 1$. The red bar indicates the lowest buckling resistance.

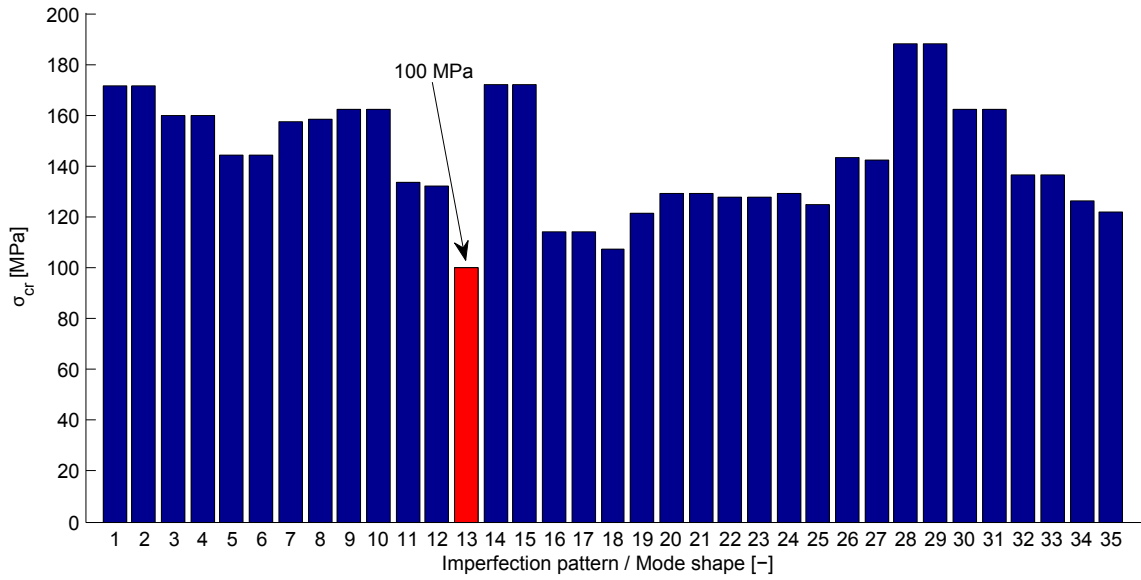


Figure 4.10: Critical buckling resistances for 35 eigenmodes obtained through GMNIA. The analysis is performed for cylinder 4, with constant imperfection amplitude $w_0/t = 1$. The red bar indicates the lowest buckling resistance.

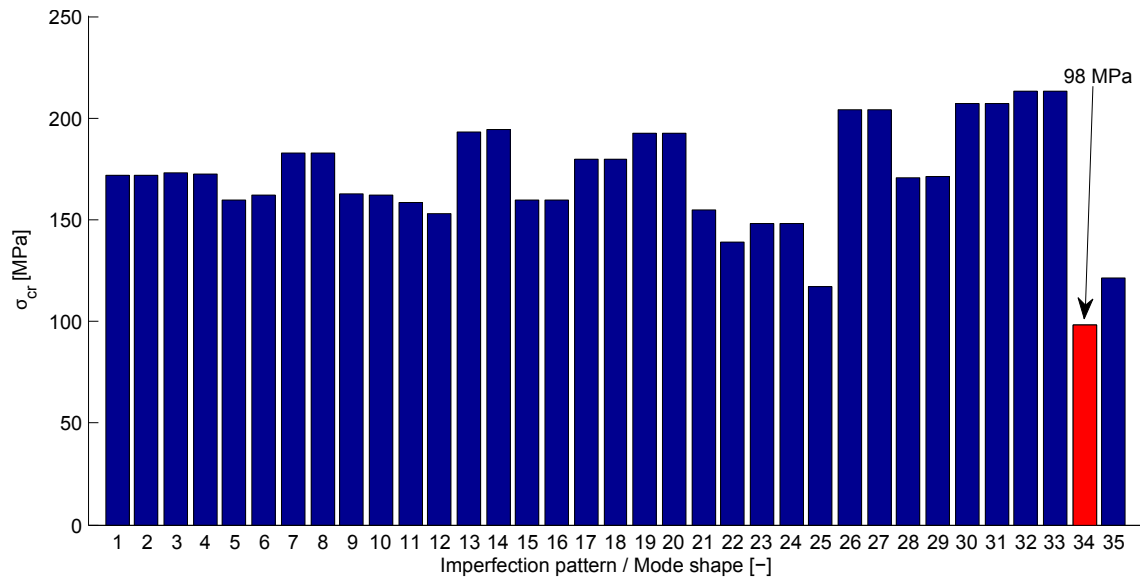


Figure 4.11: Critical buckling resistances for 35 eigenmodes obtained through GMNIA. The analysis is performed for cylinder 5, with constant imperfection amplitude $w_0/t = 1$. The red bar indicates the lowest buckling resistance.

It is observed that, when applying $w_0/t = 1$, the buckling resistances are reduced with $\approx 60\%$ and is therefore much lower than the results obtained by [Batterman, 1965]. Additionally it is investigated whether there is a connection between the three modes shapes that gives the lowest critical buckling resistance. The three mode shapes are visualised in Figure 4.12.

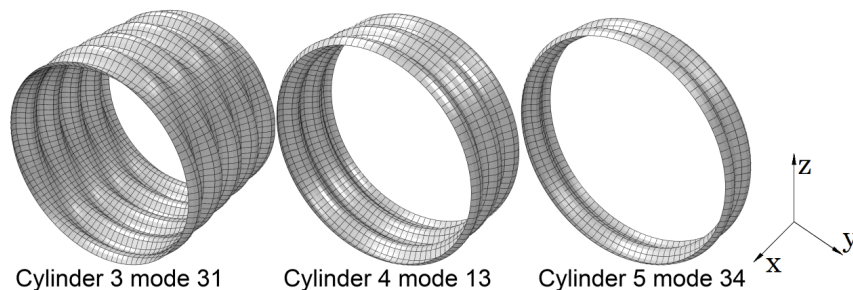


Figure 4.12: Mode shapes corresponding to the lowest critical buckling resistances for cylinder 3, 4 and 5.

The mode shapes are, despite the large difference in length, relatively similar and resembles mode shape 16 found Figure 3.4 on page 29. This “ring buckling” pattern seems to be the most critical for an axially compressed cylindrical shell.

It is of interest to calculate the size of w_0 , so that the results from the GMNIA corresponds to the experimental data, in order to obtain a low coefficient of variation of the model uncertainty. An analysis is carried out in the interval $w_0/t = [0.01; 0.075]$ to investigate the influence of the imperfection amplitude on the critical buckling resistance, see Figure 4.13.

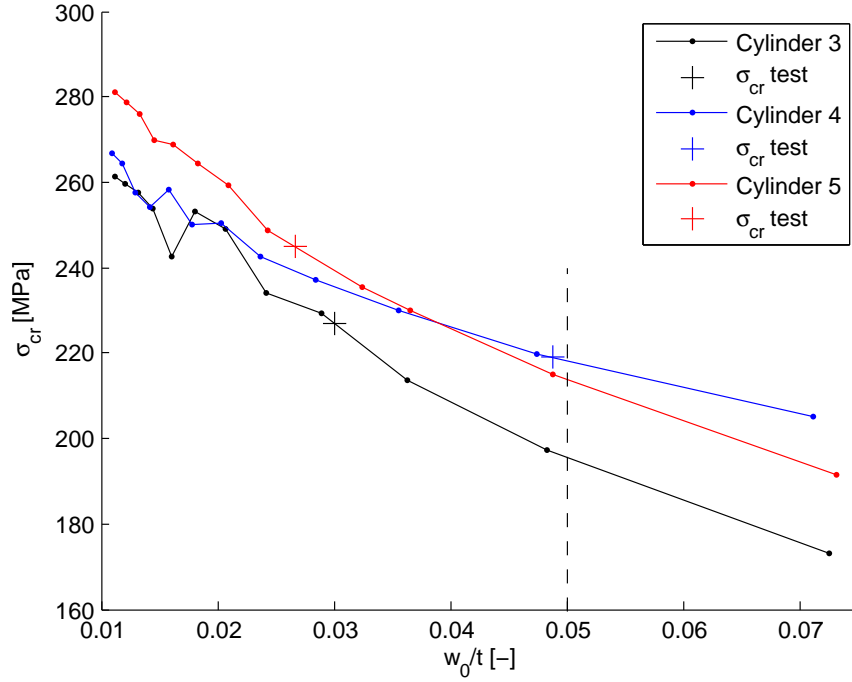


Figure 4.13: Critical buckling resistances versus imperfection amplitude normalised for the thickness, for each of the three cylinders. The crosses represent test results.

It is clear from Figure 4.13 that a very small w_0 has great influence on the buckling resistance. It is chosen to use an identical w_0 for the three test specimens, and to ensure that all $\sigma_{cr,GMNIA}$ are lower than $\sigma_{cr,Experimental}$, an imperfection amplitude normalised for the thickness is selected to $w_0/t = 0.05$. The results are listed in Table 4.5.

	$\sigma_{cr,Experimental}$ [MPa]	$\sigma_{cr,GMNIA}$ [MPa]
Cylinder 3	227.73	196.10
Cylinder 4	219.05	217.05
Cylinder 5	245.45	214.24

Table 4.5: Critical buckling resistance obtained from [Batterman, 1965] and GMNIA for the three test specimens.

The results are implemented in the approach suggested by [DS/EN-1990, 2007], annex D, while results from cylinders with $r/t < 100$ remain without imperfection, *i.e.* results from GMNA. The numerical GMNIA method suggested by [DS/EN-1993-1-6, 2007] versus the experimental data from [Batterman, 1965] is plotted in Figure 4.14

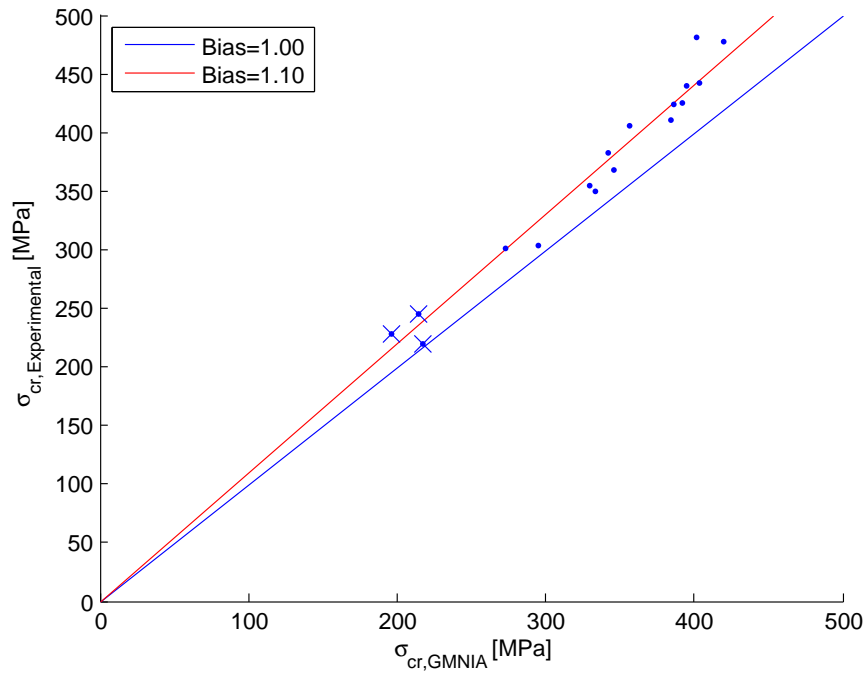


Figure 4.14: Observed buckling resistance in experiments versus estimated buckling resistance from numerical GMNIA method suggested by [DS/EN-1993-1-6, 2007]. The coefficient of variation of the model uncertainty $V_{\Delta} = 0.04$. The crosses refers to test specimens with $r/t > 100$

It is observed that the three points are above $b = 1.0$ and the coefficient of variation of the model uncertainty is calculated to $\Delta V = 0.04$. However, if the model should be used to calculate a realistic reliability index, and in order to be consistent, all test specimens have to be modeled with imperfections. This has not been done, since the test results correspond well to the GMNA, which could indicate that the geometry of the test specimens are nearly perfect. Therefore, the model uncertainty for GMNA is used in the following when estimating the reliability level for GMNIA.

5 Reliability Estimation of the Critical Buckling Resistance

In this chapter, the reliability index of the earlier presented methods to calculate the critical buckling resistance is estimated. The estimated reliability index is compared with a target reliability level β_{target} , and based on this, a calibration of the partial safety factor γ_M is performed. The following steps, inspired by [Sørensen, 2004], are performed:

- Selection of the target reliability level.
- Formulation of the failure function (limit-state function).
- Identification of stochastic variables and deterministic parameters in the failure function, along with specification of the distribution types and parameters for the stochastic variables.
- Estimation of the reliability index through a first order reliability analysis (FORM), which is validated through a crude Monte Carlo simulation (MCS).
- Comparison of the estimated reliability with the target reliability level.
- Calibration of partial safety factors in order to reach the target reliability level.

The target reliability level is selected to $\beta_{target} = 4.7$ with a reference period of 1 year. This is based on a comparison of [DS/EN-1990, 2007] and [DNV-Note-30.6, 2013], where $\beta_{target} = 4.7$ corresponds to a structure with safety class (or reliability class) RC2 in [DS/EN-1990, 2007] and a *non-redundant structure - no warning before failure* with serious consequences in [DNV-Note-30.6, 2013], see Table 1.1 and 1.2 on page 5. The 1 year reference period is selected since the distributions in the Eurocode are based on 1 year periods.

In the following, an introduction of the used methods to estimate the reliability index is presented.

5.1 General reliability estimation

In order to estimate the reliability of cylindrical shell structures, a limit-state function is required. In the present case, a collapse limit state (ultimate limit state) is considered, *i.e.* the structure is just at the point where it becomes unstable (buckles). The limit state is given as a function of realisations \mathbf{x} of the stochastic variables \mathbf{X} ;

$$g(\mathbf{x}) = g(x_1, x_2, x_3, \dots, x_n) \leq 0 \quad (5.1)$$

where positive values of $g(\mathbf{x})$ denotes the safe state, while the negative values denotes failure [Ditlevsen & Madsen, 1996]. A safety margin M is obtained by replacing realisations \mathbf{x} in the limit state function with stochastic variables \mathbf{X} ;

$$M = g(\mathbf{X}) \quad (5.2)$$

The probability of failure P_F of the limit-state function (5.1) is given as;

$$P_F = P(g(x) \leq 0) = P(M \leq 0) = \Phi(-\beta) \quad (5.3)$$

where Φ is the standard normal distribution function.

Calculations in this chapter are performed in the open-source Matlab toolbox called Finite Element Reliability Using Matlab (FERUM). The developments of the code started in 1999 at the University of California at Berkeley and consist of various structural reliability methods, but only First-Order Reliability Method (FORM) and crude Monte Carlo simulation (MCS) will be used in this thesis, and is introduced in the following.

5.1.1 First-Order Reliability Method

In order to estimate the reliability index, the First-Order Reliability Method (FORM) is used. The method uses a first-order approximation of the limit-state function (5.1) in the u -space at the failure point \mathbf{u}^* . The u -space is a normalised space, where the stochastic variables u_1, u_2, \dots, u_n are Normal distributed with mean value $\mu = 0$ and standard deviation $\sigma = 1$. The failure point, also called the design point, is defined as the point on the limit-state surface, which is closest to the origin, and the distance is defined as the the Hasofer & Lind reliability index β . An illustration of the method is shown in Figure 5.1.

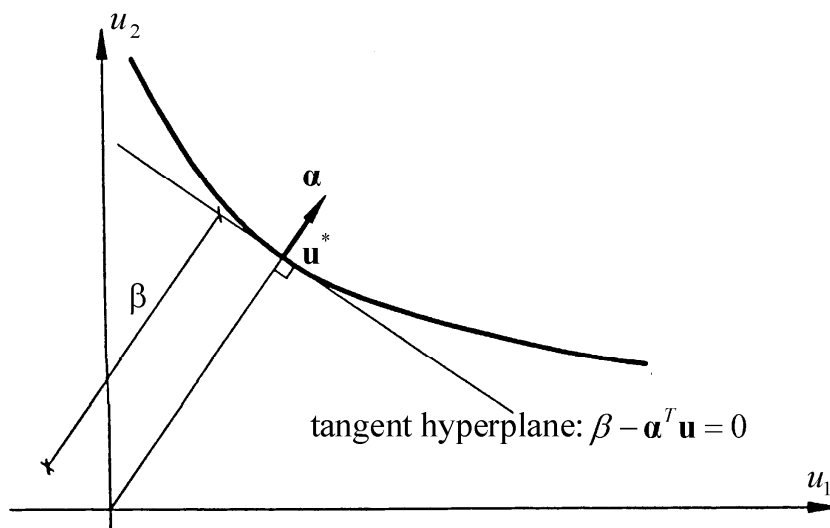


Figure 5.1: Geometrical illustration of the reliability index β in u -space [Sørensen, 2004].

To obtain the reliability index β the optimization problem (5.4) has to be solved.

$$\beta = \min_{g_u(\mathbf{u})=0} \sqrt{\sum_{i=1}^n u_i^2} \quad (5.4)$$

There are several numerical algorithms to solve this optimization problem, but the standard algorithm in FERUM will be used in the present examples without further considerations.

As seen in Figure 5.1, α is defined as a normal vector to the failure surface at the failure

point and is given as:

$$\alpha_i = \left. \frac{d\beta}{du_i} \right|_{u=u^*} \quad (5.5)$$

where

$$\begin{array}{l|l} \alpha & \text{Unit normal to the failure surface at the } \beta\text{-point} \\ u^* & \beta\text{-point in the } u\text{-space} \end{array}$$

The α -vector can be used as a measure of how the individual stochastic variables influence the reliability index β . The variance of the linear safety margin $M = \beta - \alpha^T \mathbf{U}$ is given as;

$$\sigma_M^2 = \alpha_1^2 + \alpha_2^2 + \dots + \alpha_n^2 = 1 \quad (5.6)$$

If the stochastic variables U_i and X_i are independent, α_i^2 gives the percentage of the total uncertainty. Another important sensitivity measure is the *omission sensitivity factor* ζ given as;

$$\zeta_i = \frac{1}{\sqrt{1 - \alpha_i^2}} \quad (5.7)$$

The omission sensitivity factor is a measure of the importance on the reliability index if a given stochastic variable is assumed deterministic [Sørensen, 2004].

5.1.2 Crude Monte Carlo simulation and Importance Sampling

When performing a Monte Carlo simulation, distinctions is made between *crude* estimation (MCS) and *importance sampling* (MCSIS). In MCS the probability of failure \hat{P}_f is estimated in a statistical sense, that is, N independent samples $\hat{\mathbf{u}}_j$ are randomly sampled in the u -space.

$$\hat{P}_f = \frac{1}{N} \sum_{j=1}^N I[g(\hat{\mathbf{u}}_j)] \quad (5.8)$$

where $I[g(\mathbf{u})]$ is the indicator function defined as;

$$I[g(\mathbf{u})] = \begin{cases} 0 & \text{if } g(\mathbf{u}) > 0 \text{ (safe)} \\ 1 & \text{if } g(\mathbf{u}) \leq 0 \text{ (unsafe)} \end{cases} \quad (5.9)$$

MCS is visualised in Figure 5.2 for a simple case with two stochastic variables X_1 and X_2 representing load and strength respectively.

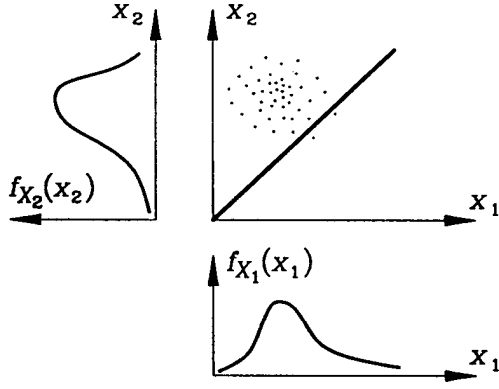


Figure 5.2: Crude Monte Carlo [Sørensen, 2004].

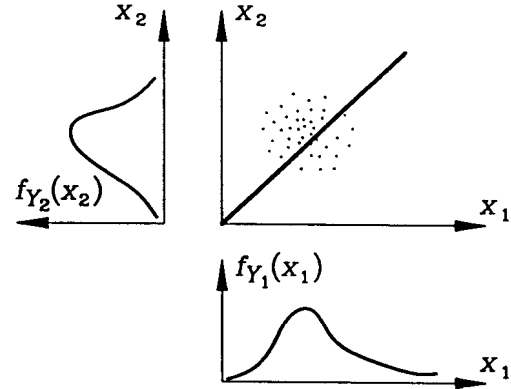


Figure 5.3: Monte Carlo with importance sampling [Sørensen, 2004].

When estimating the probability of failure by MCSIS, the idea is to concentrate the simulations in the area with the greatest contribution on the probability of failure, see Figure 5.3. (5.8) is rewritten and the probability of failure is estimated by:

$$\hat{P}_f = \frac{1}{N} \sum_{j=1}^N I[g(\hat{\mathbf{y}}_j)] \frac{f_U(\hat{\mathbf{y}}_j)}{f_S(\hat{\mathbf{y}}_j)} \quad (5.10)$$

where $f_S(\hat{\mathbf{y}}_j)$ is called the sampling density and $f_U(\hat{\mathbf{y}}_j)$ is the standard normal density function for \mathbf{U} .

The advantage of the MCSIS is that a smaller amount of simulations is needed, compared to MCS. However, if the FORM analysis provides inaccurate results, the importance sampling uses inaccurate information and therefore a large number of simulations is required to obtain accurate results. In the present calculations, the MCS will be used, since it is wanted as a verification tool to the FORM results.

5.2 Design equation and limit state function

In the following, the reliability of the cylindrical shell is estimated from only one failure mode, whereas in a real design process all thinkable failure modes, such as yielding in the material or rupture due to fatigue, should be taken into account.

Two loads are considered, namely the permanent dead load and the variable wind load and are combined through the load combinations STR (*strength*) (6.10a) and (6.10b) in [DS/EN-1990, 2007]. To investigate the influence of the ratio between the permanent and variable load, a parameter η is introduced and (6.10a) and (6.10b) is rewritten, as suggested in [DS/INF-172, 2009], leading to the following design equations;

$$G = z_B \frac{h(\mathbf{x}_c, R_1, \dots, R_n)}{\gamma_{M1}} - ((1 - \eta)\gamma_{GB, sup} G_{Uc}) \quad (6.10a) \quad (5.11)$$

$$G = z_A \frac{h(\mathbf{x}_c, R_1, \dots, R_n)}{\gamma_{M1}} - ((1 - \eta)\gamma_{GA, sup} G_{Uc} + \eta\gamma_Q Q_c) \quad (6.10b) \quad (5.12)$$

where

z_A, z_B	Design parameters
h	Mathematical model of the critical buckling resistance
\mathbf{x}_c	Characteristic values
R_i	Regression parameters
γ_{M1}	Partial safety factor for shell stability
η	Parameter controlling the ratio between permanent and variable load [0;1]
$\gamma_{G,sup}$	Partial safety factor for permanent load
γ_Q	Partial safety factor for variable load
G_{Uc}	Characteristic permanent load that acts unfavorable
Q_c	Characteristic variable load

The less favorable of (5.11) and (5.12) is selected based on the choice of η , where $\eta = 0$ corresponds to no variable load and $\eta = 1$ corresponds to no permanent load.

The limit-state function corresponding to the design equation can be written;

$$g = zX_R h(\mathbf{X}, R_1, \dots, R_n) - ((1 - \eta)G + \eta Q X_Q) \quad (5.13)$$

where

X_R	Model uncertainty of h
\mathbf{X}	Stochastic variables
X_Q	Model uncertainty of Q

Negative values of g in (5.13) represents the buckled state *i.e.* failure, while positive values denotes the safe state. The design parameter z is selected as the maximum of z_A and z_B in (5.11) and (5.12).

5.2.1 Stochastic variables

The stochastic variables \mathbf{X} used in (5.13) are presented in Table 5.1. The uncertainties and characteristic values are based on different references shown in the table, while model uncertainties are based on section 4.1. The initial imperfection amplitude w_0/t is assumed to be normal distributed with mean value $\mu = 0$ and standard deviation $\sigma_{w_0/t} = 0.1 - 0.5$. The reason for the varying standard deviation is that it is of interest to investigate the influence of $\sigma_{w_0/t}$ on the reliability index.

Variable	μ	σ	V	Distr.	Quantile	X_c	Reference
f_y [MPa]	264.3	18.5	0.07	LN	5%	235	[JCSS, 2001]
E [GPa]	210	6.3	0.03	LN	μ	210	[JCSS, 2001]
ν	0.3	0.009	0.03	LN	μ	0.3	[JCSS, 2001]
w_0/t	0	0.1-0.5	-	N	-	-	-
$X_{R,DS/EN}$	1.28	0.05	0.04	LN	-	-	Tabel 4.3 on page 47
$X_{R,DNV}$	1.25	0.18	0.15	LN	-	-	Tabel 4.3 on page 47
$X_{R,GMNA}$	1.08	0.108	0.10	LN	-	-	Tabel 4.3 on page 47
Q_{wind}	1.00	0.25	0.25	G	98%	1.65	[Sørensen et al., 2001]
$X_{Q,wind}$	1.00	0.22	0.22	G	72%	1.10	[Sørensen et al., 2001]
G	1.00	0.10	0.10	N	50%	1.00	[DS/INF-172, 2009]

Table 5.1: Stochastic variables. N~Normal, LN~LogNormal, G~Gumbel.

The mean value of the loads in Tabel 5.1 is selected to be 1.00, as they are accounted for in the design parameter z .

5.3 Reliability estimation

In the following, FORM is used to estimate the reliability index β for a number of η -values, while MCS is used as a verification tool. The advantage of MCS is that no approximations is made, while the disadvantage is that it is significantly slower compared to FORM. Two approaches are conducted;

- **Method 1:** The critical buckling resistance in the design equations, (5.11)/(5.12), is calculated by the semi-empirical method in [DS/EN-1993-1-6, 2007], see Appendix A.
- **Method 2:** The critical buckling resistance in the design equations, (5.11)/(5.12), is calculated by the semi-empirical method in [DNV-RP-C202, 2013], see Appendix B.

Besides the difference in the characteristic critical buckling resistance ($\sigma_{c,Eurocode} = 152$ MPa and $\sigma_{c,DNV} = 130$ MPa), also the partial safety factor γ_M differs. All used partial safety factors are listed in Table 5.2. It should be noted, that the partial safety factors related to the load term ($\gamma_{Gj,sup}, \gamma_{Q,1}$) in (5.11)/(5.12) entirely are selected from [DS/EN-1990, 2007].

Partial safety factor	Equation (5.11)	Equation (5.12)
$\gamma_{M1,DS/EN}$	1.20	1.20
$\gamma_{M,DNV}$	1.45	1.45
$\gamma_{Gj,sup,DS/EN}$	1.20	1.00
$\gamma_{Q,1,DS/EN}$	-	1.50

Table 5.2: Partial safety factors.

It is seen from Table 5.2, that a large difference is observed in γ_M which is caused by the different approaches in the design codes.

In [DS/EN-1993-1-6, 2007] γ_M is selected on the basis of a consequence class, chosen to CC2 equivalent to *medium consequence class*. In the present case, $\gamma_{M1,DS/EN} = 1.20$ is selected based on the Danish national annex. In contrast to this, γ_M in [DNV-RP-C202, 2013] is calculated directly from the *reduced shell slenderness*, $\bar{\lambda}_s$.

5.3.1 Semi-empirical models

In the following, results from the two approaches are presented. In Figure 5.4, β versus η is plotted for method 1 using the semi-empirical mathematical model in [DS/EN-1993-1-6, 2007] and method 2 using the semi-empirical mathematical model in [DNV-RP-C202, 2013]. It is observed that β estimated through FORM and Monte Carlo almost are identical, and it is concluded, that in this case, FORM is a reasonable tool to estimate the reliability index.

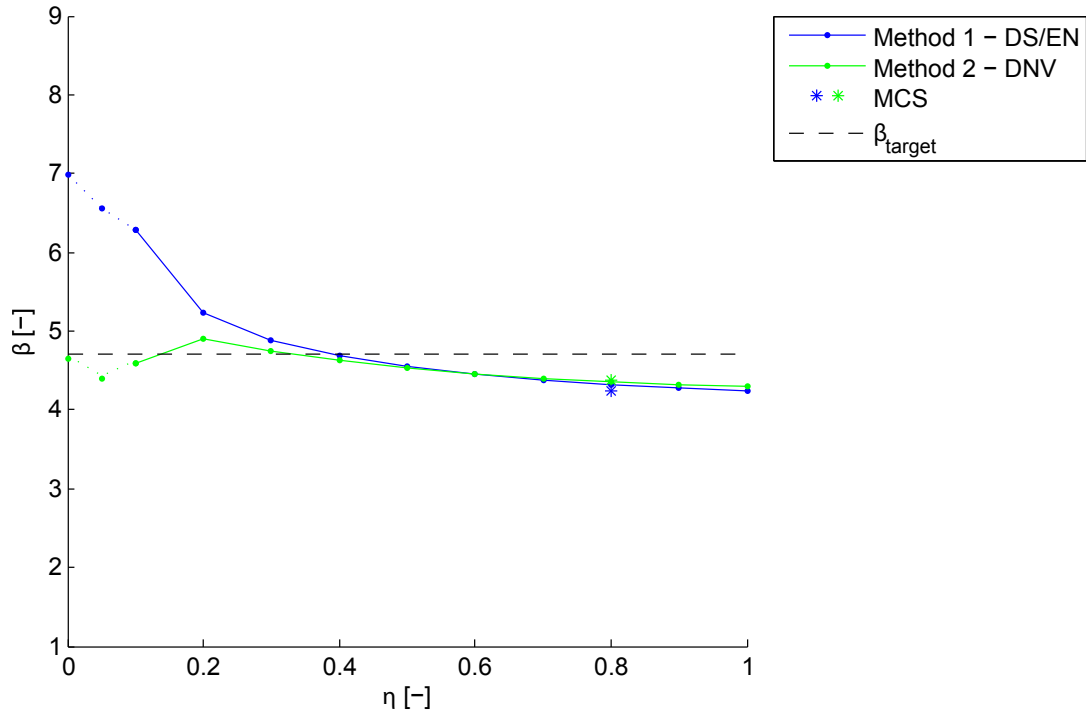


Figure 5.4: Reliability index β versus the parameter η for method 1 using the semi-empirical mathematical model in [DS/EN-1993-1-6, 2007] and method 2 using the semi-empirical mathematical model in [DNV-RP-C202, 2013]. The points at the dashed lines represent use of (5.11), while the points at the solid lines represent use of (5.12).

From Figure 5.4, a large difference in β is observed with $\eta < 0.3$. This is caused by the large difference in the model uncertainty of the two methods, see Table 5.1. β is almost the same with $\eta > 0.3$. This is due to the fact, that the importance of the uncertainty on the variable load increases with η and since they are equal in the two methods the reliability index becomes close to equal. The importance of the stochastic variables are listed as α^2 -values in Table 5.3 and 5.4.

Eurocode	$\alpha_{\eta=0}^2$	$\alpha_{\eta=0.1}^2$	$\alpha_{\eta=0.2}^2$	$\alpha_{\eta=1}^2$	DNV	$\alpha_{\eta=0}^2$	$\alpha_{\eta=0.1}^2$	$\alpha_{\eta=0.2}^2$	$\alpha_{\eta=1}^2$
f_y	0.44	0.26	0.08	0.02	f_y	0.01	0.01	0	0
X_R	0.10	0.08	0.02	0	X_R	0.73	0.72	0.36	0.11
G	0.42	0.18	0.02	0	G	0.24	0.19	0.04	0
Q_{wind}	0	0.25	0.45	0.51	Q_{wind}	0	0.02	0.30	0.47
$X_{Q,wind}$	0	0.22	0.41	0.45	$X_{Q,wind}$	0	0.01	0.27	0.41

Table 5.3: α^2 -values for method 1 using the semi-empirical mathematical model in [DS/EN-1993-1-6, 2007].

Table 5.4: α^2 -values for method 2 using the semi-empirical mathematical model in [DNV-RP-C202, 2013].

It is clearly seen from Table 5.3 and 5.4, that the importance of the model uncertainty X_R reduces with increasing η . When comparing the estimated β -values with the selected target reliability level, a larger deviation is observed, when using method 1 with the semi-empirical mathematical model in [DS/EN-1993-1-6, 2007] compared to method 2 using the semi-empirical mathematical model in [DNV-RP-C202, 2013].

5.3.2 Numerical models

In order to calculate the reliability index for the mathematical models (GMNA and GMNIA) used in Abaqus, simplifications have to be made. The reason for the simplifications is, that when calculating the reliability index in FERUM, a large number of calls (typical more than 50) to the failure function is necessary. This procedure is computationally heavy, since a calculation to obtain the critical buckling resistance in Abaqus is needed for each call to the failure function. As an example, a GMNA calculation of the critical buckling resistance in Abaqus takes approximately 200 seconds, corresponding to approximately 3 hours to obtain a single value of β . Additionally, a Monte Carlo simulation is virtually impossible to perform, if the critical buckling resistance needs to be obtained in Abaqus.

To overcome the problem, a mathematical simplification for the numerical models is conducted. Basically the simplification is based on knocking down the critical buckling resistance obtained in the linear bifurcation analysis. The parameters included in the knock down factors are determined from the α^2 -vector, where it is observed that, by only looking at the physical parameters, the yield stress, f_y , and the imperfection amplitude, w_0/t , has the most influence on the reliability index. The simplified mathematical models used to calculate the critical buckling resistance for GMNA and GMNIA can then be written as;

$$\sigma_{cr,GMNA} = X_{R,GMNA}(f_y)\sigma_{cr,LBA} \quad (5.14)$$

$$\sigma_{cr,GMNIA} = X_{R,GMNA}(f_y)X_{R,imp}(w_0/t)\sigma_{cr,LBA} \quad (5.15)$$

where

$X_{R,GMNA}$		Knock down factor determined as $\sigma_{cr,GMNA}/\sigma_{cr,LBA}$
$\sigma_{cr,LBA}$		Critical buckling resistance obtained through LBA
$X_{R,imp}$		Knock down factor for imperfections determined as $\sigma_{cr,GMNIA}/\sigma_{cr,GMNA}$

The knock down factors as function of f_y and w_0/t are shown in Figure 5.5 and 5.6 respectively.

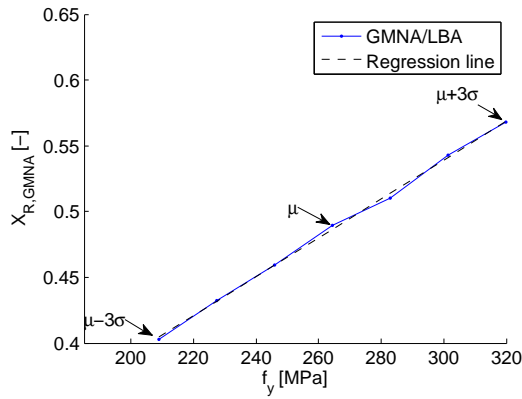


Figure 5.5: Knock down factor $X_{R,GMNA}$ versus yield stress f_y .

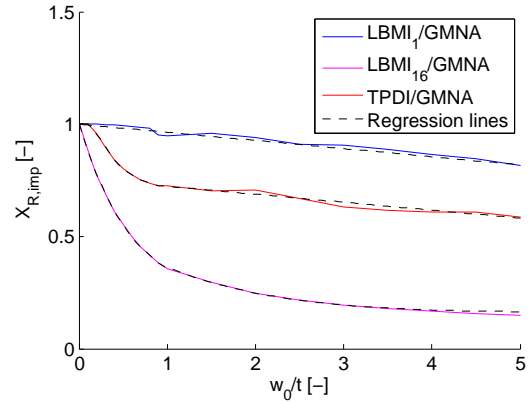


Figure 5.6: Knock down factor $X_{R,imp}$ versus imperfection amplitude w_0/t for LBMI₁, LBMI₁₆ and TPDI.

The large difference between the critical buckling resistance obtained in LBA and GMNA is reflected in the large knock down factor $X_{R,GMNA}$ in Figure 5.5. It should be noted, that the simplification makes f_y and w_0/t independent. Three initial imperfection patterns are selected for further investigation, namely; LBMI₁, LBMI₁₆ and TPDI. The LBMI patterns are selected since they are suggested as initial imperfections in [DS/EN-1993-1-6, 2007], while the TPDI is selected as an alternative. The initial imperfection pattern for each model; LBMI₁, LBMI₁₆ and TPDI is shown in Figure 3.27 on page 38. In order to implement the knock down factor $X_{R,imp}$ in FERUM, different regression lines, shown in Figure 5.6, are made depending on the imperfection pattern.

Figure 5.7 shows the reliability index β versus the parameter η for method 1 and 2 using the mathematical GMNA model. It is seen that β estimated through FORM and MCS coincides, and the FORM results are therefore considered valid.

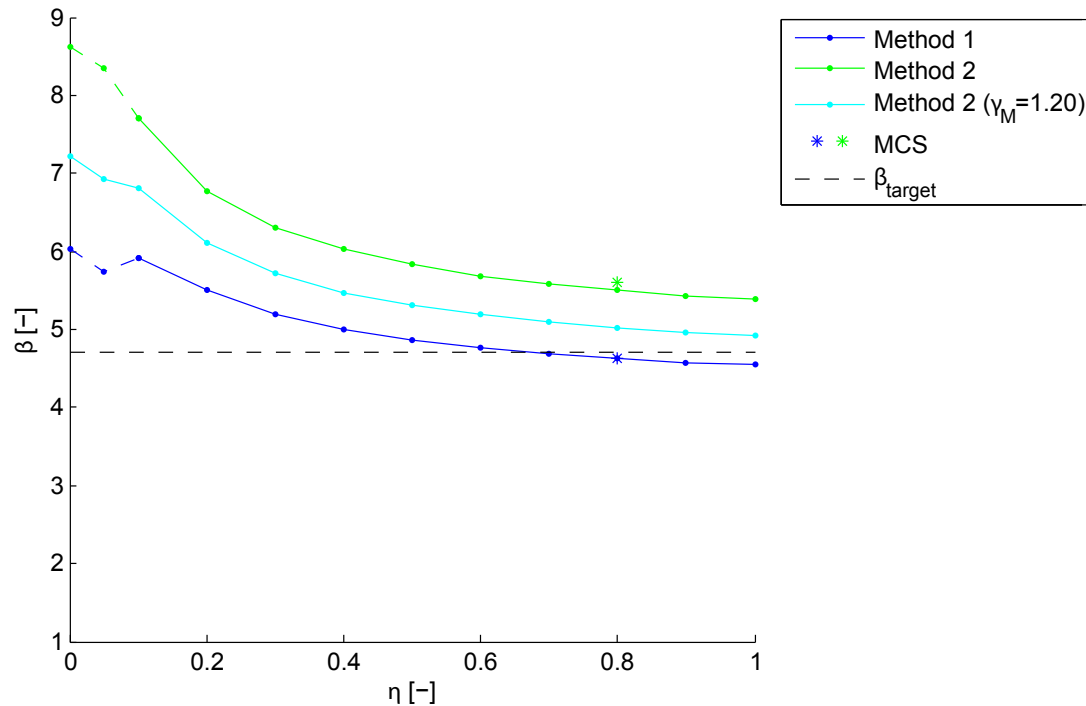


Figure 5.7: Reliability index β versus the parameter η for method 1 and 2 using the mathematical GMNA model. The points at the dashed lines represent use of (5.11), while the points at the solid lines represent use of (5.12).

Generally, method 1 gives a lower reliability level compared to method 2 when using the mathematical GMNA model and the reliability level for both methods is above the target reliability. The reason for the difference between the two methods is, that a lower partial safety factor and a higher characteristic critical buckling resistance is used in the design equation for method 2. It is assessed, that the difference in the partial safety factor has the highest influence on the reliability index. Therefore it is investigated how the reliability level will change when the partial safety factor in the resistance term in method 2 is selected to $\gamma_M = 1.20$ *i.e.* the partial safety factor from [DS/EN-1993-1-6, 2007]. As shown in Figure 5.7, the reliability level decreases when using $\gamma_M = 1.20$ in method 2, and the difference is solely caused by difference in the characteristic critical buckling resistance used in the design equations.

In order to investigate the influence of the imperfection amplitude on the reliability index, three different standard divisions is selected namely; $\sigma_{w_0/t}=0.1$, $\sigma_{w_0/t}=0.3$ and $\sigma_{w_0/t}=0.5$, which is shown for method 1, while only $\sigma_{w_0/t}=0.3$ is shown for method 2. Reliability index β versus the parameter η for method 1 and 2 using the mathematical GMNIA model with initial imperfection pattern $LBMI_1$ is shown in Figure 5.8.

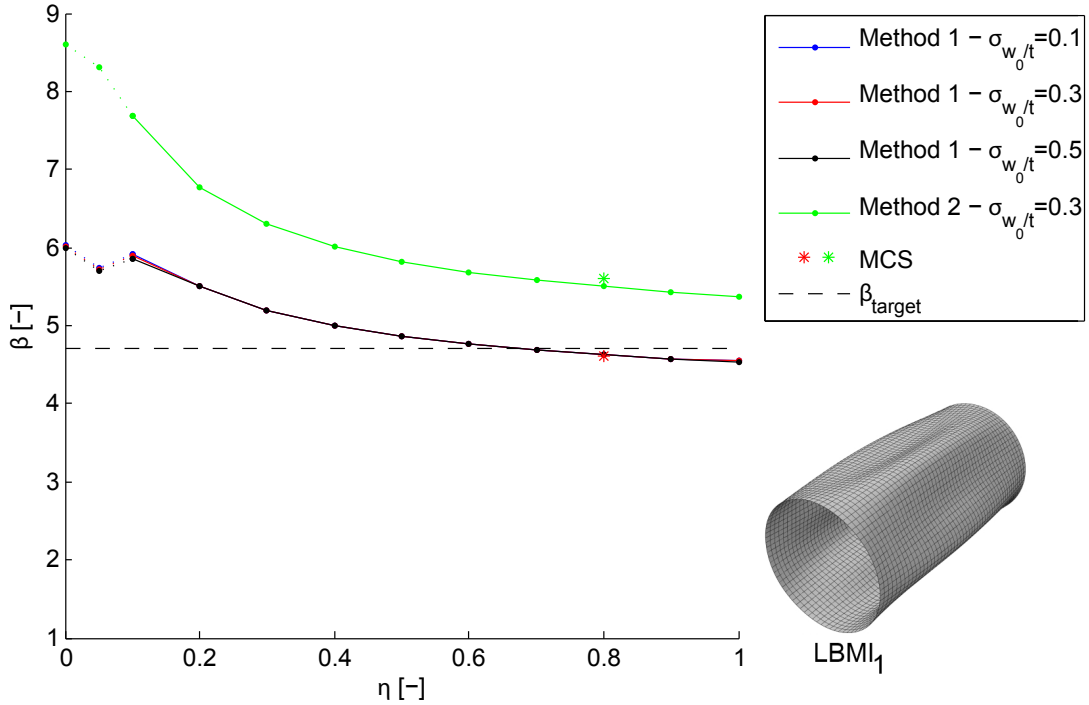


Figure 5.8: Reliability index β versus the parameter η for method 1 and 2 using the mathematical GMNIA model with initial imperfections from LBMI_1 with varying standard deviation $\sigma_{w_0/t}$. The points at the dashed lines represent use of (5.11), while the points at the solid lines represent use of (5.12).

The estimated β -values are almost identical to the β -values in Figure 5.7, which is due to the low knock down factor, $X_{R,imp}$ for LBMI_1 . It is therefore concluded that a rather high $\sigma_{w_0/t}$ is needed to have an influence on the reliability index when modeling the imperfection as LBMI_1 .

Figure 5.9 shows the reliability index β versus the parameter η for method 1 and 2 using the mathematical GMNIA model with initial imperfection pattern LBMI_{16} . In contrast to the previous results, the β estimated from FORM deviates from the β estimated from MCS. This indicates that the FORM-results not are reliable, and is likely caused by the regression lines used to approximate the knock down factors $X_{R,GMNA}$ and $X_{R,imp}$. Three MCS are performed, and it is seen that the trend is similar, and that it is likely that the β -level is lower than shown in Figure 5.9. Only method 1 with $\sigma_{w_0/t} = 0.1$ has a reliability level close to the target reliability, which indicates that when using LBMI_{16} as the initial imperfection pattern, low reliability levels are achieved.

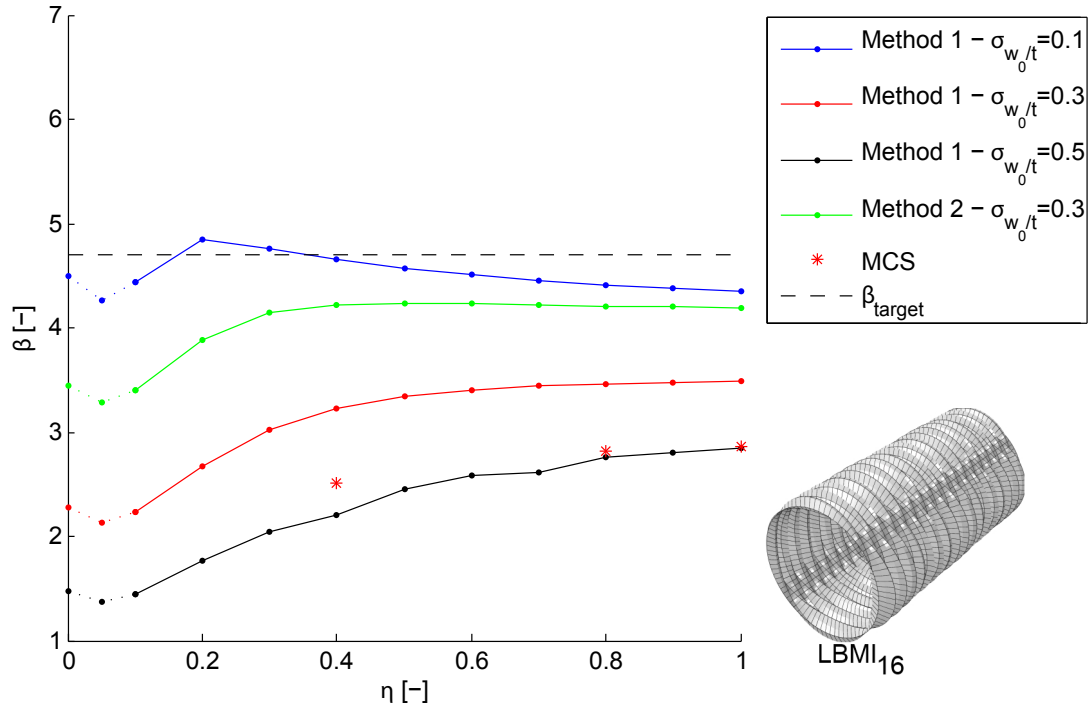


Figure 5.9: Reliability index β versus the parameter η for method 1 and 2 using the mathematical GMNIA model with initial imperfections from LBMI₁₆ with varying standard deviation $\sigma_{w_0/t}$. The points at the dashed lines represent use of (5.11), while the points at the solid lines represent use of (5.12).

From Figure 5.9 it is seen that the $\sigma_{w_0/t}$ have a high influence on the reliability level, which also is shown by the α^2 -values in Table 5.5 and 5.6. Even with $\eta = 1$, the imperfection has an influence on the reliability index, especially when $\sigma_{w_0/t} = 0.5$.

	$\alpha^2_{\eta=0}$	$\alpha^2_{\eta=0.1}$	$\alpha^2_{\eta=0.2}$	$\alpha^2_{\eta=1}$
f_y	0.07	0.07	0.06	0.01
X_R	0.28	0.28	0.24	0.05
G	0.21	0.18	0.10	0
Q_{wind}	0	0.01	0.12	0.45
$X_{Q,wind}$	0	0.01	0.09	0.39
w_0/t	0.42	0.43	0.36	0.08

Table 5.5: α^2 -values for method 1 using the mathematical GMNIA model with initial imperfections from LBMI₁₆ with standard deviation $\sigma_{w_0/t} = 0.1$.

	$\alpha^2_{\eta=0}$	$\alpha^2_{\eta=0.1}$	$\alpha^2_{\eta=0.2}$	$\alpha^2_{\eta=1}$
f_y	0	0	0	0
X_R	0.03	0.03	0.03	0.03
G	0.02	0.02	0.02	0
Q_{wind}	0	0	0	0.23
$X_{Q,wind}$	0	0	0	0.18
w_0/t	0.93	0.93	0.92	0.53

Table 5.6: α^2 -values for method 1 using the mathematical GMNIA model with initial imperfections from LBMI₁₆ with standard deviation $\sigma_{w_0/t} = 0.5$.

In Figure 5.10, reliability index β versus the parameter η for method 1 and 2 using the mathematical GMNIA model is shown with TPDI as the initial imperfection pattern. Deviations in β estimated from FORM and β estimated from MCS is observed. Again three MCS are performed to show that the trend of the FORM is similar to the trend of the MCS, but is generally lower as shown in Figure 5.10.

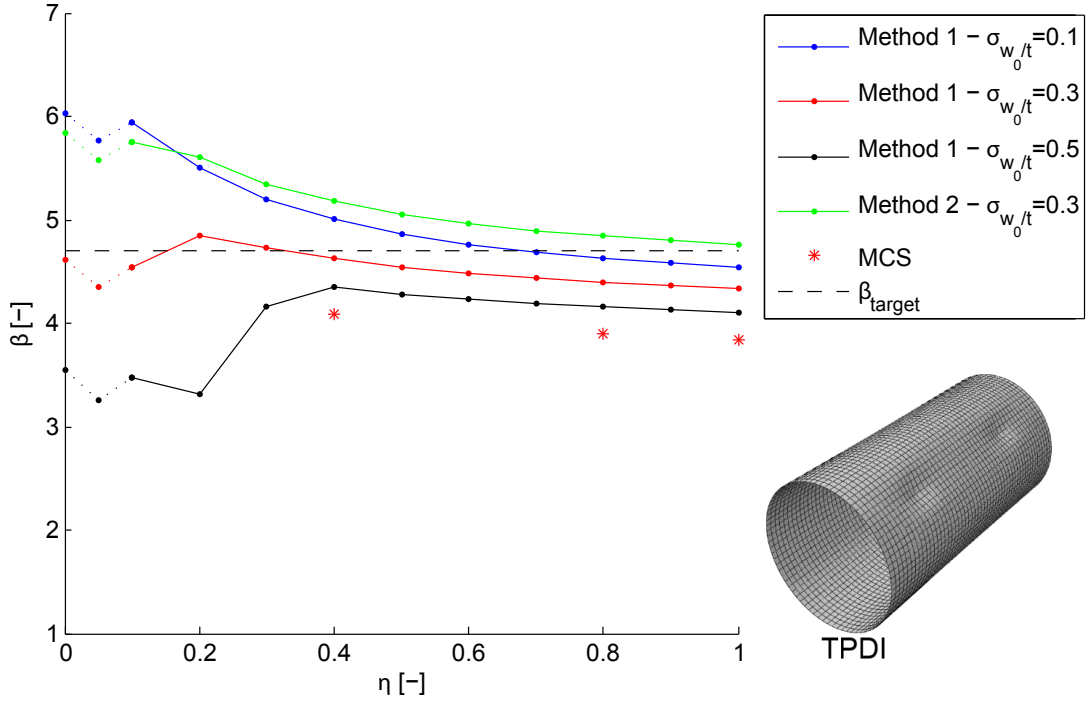


Figure 5.10: Reliability index β versus the parameter η for method 1 and 2 using the mathematical GMNIA model with initial imperfections from TPDI with varying standard deviation $\sigma_{w_0/t}$. The points at the dashed lines represent use of (5.11), while the points at the solid lines represent use of (5.12).

It is seen from Figure 5.10 that large differences are observed when $\eta < 0.4$, and is caused by the uncertainty related to w_0/t . For $\eta > 0.4$ the reliability level is nearly linear and is only decreasing slightly with increasing η . Furthermore it is observed that method 1 with $\sigma_{w_0/t} = 0.3$ has the most stable reliability level and is also close to the target reliability.

5.4 Calibration of partial safety factors

In this section, the partial safety factor γ_M is calibrated for the Eurocode, *i.e.* method 1 using the semi-empirical mathematical model in [DS/EN-1993-1-6, 2007]. Furthermore the partial safety factor γ_M is calibrated for method 1 using the mathematical model GMNIA with imperfection patterns LBMI₁, LBMI₁₆ and TPDI. It is chosen to calibrate γ_M in the design code in order to investigate whether it is possible to optimise it. The imperfection patterns LBMI₁, LBMI₁₆ and TPDI are chosen for further investigation since LBMI₁ is assessed to be the first choice in a real design case, while LBMI₁₆ is the “worst” and in principle is recommended in [DS/EN-1993-1-6, 2007]. TPDI is assessed as a reasonable alternative of simulating the initial imperfections.

To calibrate the partial safety factor, an optimisation problem is introduced:

$$\min W(\gamma) = \sum_{j=1}^L w_j (\beta_j(\gamma) - \beta_{target})^2 \quad (5.16)$$

where W is the error *i.e.* the sum of the distance from β_j to β_{target} squared. w_j is a weight factor which defines the importance of each design case, and in the present example, all design cases are equally weighted. The partial safety factor is selected such that the error

is minimum, thereby giving the best fit. It should be mentioned that this method does not take into account a β_{min} , which in some cases is necessary to fulfill the requirements.

Calibration of the partial safety factor γ_M for method 1 using the semi-empirical mathematical model in [DS/EN-1993-1-6, 2007] is shown in Figure 5.11. It is seen, that to obtain a reliability level that is close to the target, *i.e.* use of (5.16), the partial safety factor is reduced from 1.20 to 1.05 in method 1. This corresponds well with the recommended partial safety factor in [DS/EN-1993-1-6, 2007] ($\gamma_{M1} = 1.10$) and indicates that in this case, the Danish national annex might be too conservative.

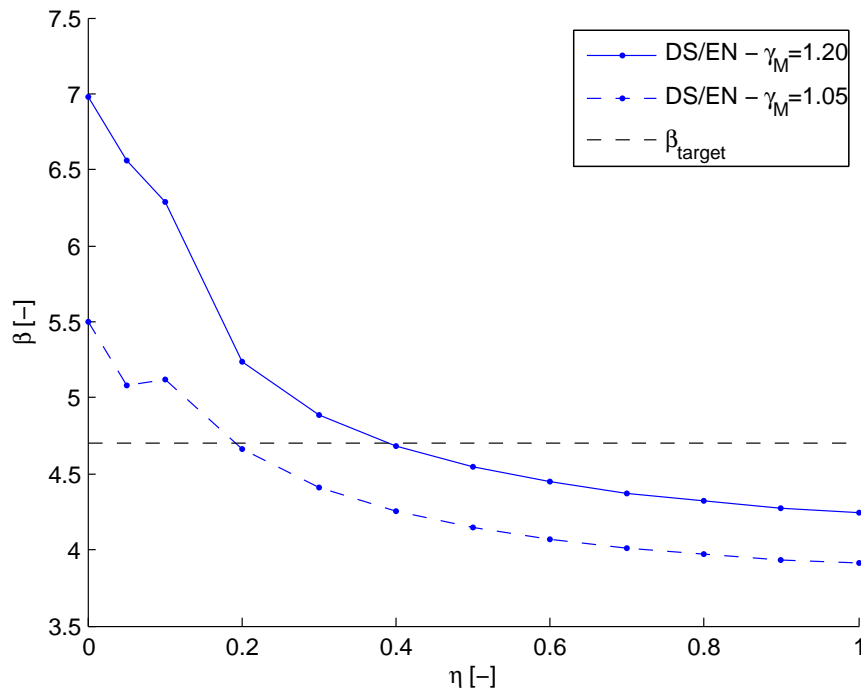


Figure 5.11: Reliability index β versus the parameter η for method 1 using the semi-empirical mathematical model in [DS/EN-1993-1-6, 2007] with varying partial safety factor.

Calibration of the partial safety factor for the mathematical GMNIA model is done with initial imperfections from LBMI₁, LBMI₁₆ and TPDI. When implementing the initial imperfection pattern from LBMI₁₆, the standard deviation of the imperfection amplitude is selected to $\sigma_{w_0/t} = 0.1$, while it is selected to $\sigma_{w_0/t} = 0.3$ for LBMI₁ and TPDI. The reason for selecting these standard deviations is that it is assessed that they provide the most reasonable imperfection amplitude while taking the imperfection pattern into account.

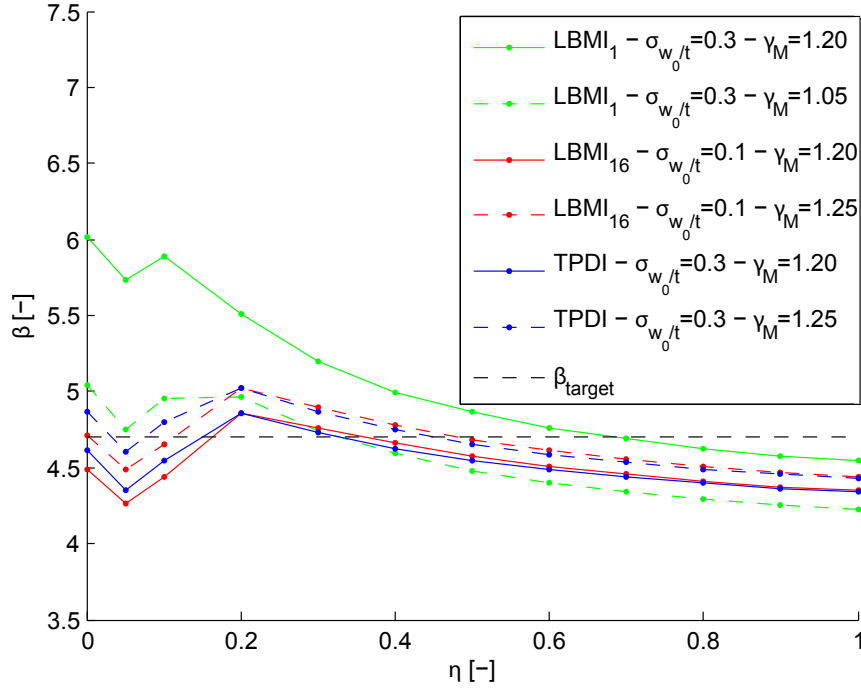


Figure 5.12: Reliability index β versus the parameter η for method 1 using the GMNIA model with initial imperfections from LBMI₁, LBMI₁₆ and TPDI with varying partial safety factor.

As shown in Figure 5.12, the estimated reliability levels for LBMI₁₆ and TPDI are fairly similar for the selected standard deviations and the partial safety factor increases from 1.20 to 1.25 in both models. It is obvious that the partial safety factor is closely related to the standard deviation of the imperfection amplitude and imperfection pattern. Furthermore, it is seen that it is possible to reduce the partial safety factor from 1.20 to 1.05 when using LBMI₁ as the initial geometric imperfection. This is similar to the result obtained with method 1 using the semi-empirical mathematical model in [DS/EN-1993-1-6, 2007].

From the results, it could be of interest for further studies to estimate the probability of the occurrence of each individual imperfection pattern and implement this into the reliability analysis.

6 Conclusions

In the present thesis, buckling of axially compressed cylindrical steel shells is investigated, where the main focus is put on simulating initial geometric imperfections and the influence of these on the reliability level.

In order to estimate the critical buckling resistance both analytical, semi-empirical and numerical methods are used. It is shown through historical review, that the classical solution of the critical buckling stress gives unrealistic results, which is due to the linear assumptions made in the solution along with the assumption of a perfect geometry. To overcome this problem, [DS/EN-1993-1-6, 2007] and [DNV-RP-C202, 2013] uses semi-empirical approaches to estimate the critical buckling resistance. However, it can be concluded, when comparing with test results from [Batterman, 1965], that results obtained through these approaches are conservative.

Another approach to estimate the critical buckling resistance is numerical finite element analyses with different complexity, which also is recommended in [DS/EN-1993-1-6, 2007]. By use of this approach, a geometric and material non-linear analysis (GMNA) can be taken into account and this analysis coincides well with test results in [Batterman, 1965]. It can therefore be concluded that the numerical GMNA approach is very useful when estimating the critical buckling resistance. This conclusion though, is only valid when the cylindrical shell has a nearly perfect geometry, which is very unlikely for a cylindrical shell used in typical civil engineering structures.

Through state-of-the-art review, it is shown that numerous ways of simulating geometrical imperfections exist. Three different approaches of simulating initial geometric imperfections are compared, namely the linear buckling mode-shaped imperfection (LBMI), the single perturbation displacement imperfection (SPDI) and two perturbation displacements imperfection (TPDI). Through the investigation of the different approaches, it is shown that the imperfection pattern as well as the imperfection amplitude has a high influence on the critical buckling resistance. By implementing the LBMI patterns as initial geometric imperfection through a geometric and material non-linear analysis (GMNIA), it is concluded that the choice of the initial mode shape is of great importance. This is clearly shown by comparing the reduction of the critical buckling resistance obtained with the linear buckling mode-shaped imperfection for mode 1 (LBMI₁) and mode 16 (LBMI₁₆). With use of an imperfection amplitude corresponding to 1 wall thickness ($w_0/t = 1$), a reduction of 5% and 60% compared to GMNA, is calculated when using LBMI₁ and LBMI₁₆ respectively.

A similar result is obtained when implementing SPDI and TPDI as the initial geometric imperfection. When using $w_0/t = 1$, the SPDI pattern reduces the critical buckling resistance with 2%, while a reduction of 30% is seen for TPDI compared to the result obtained through the GMNA.

Since the geometrical imperfections are modeled as “worst”, it is obvious that large reductions are observed, and this approach might be too conservative. Furthermore, it is questionable how realistic the mode shaped patterns are as initial geometric imperfections, especially when high order modes are considered. It could therefore be of interest, for

further studies, to take the probability of the occurrence of the mode shaped imperfections into account.

In order to take the model uncertainties into account, when estimating the reliability of the presented models, the method in annex D in [DS/EN-1990, 2007] are used with test results from [Batterman, 1965]. Furthermore, two methods to set up the design equations is introduced, one where the resistance term is based on the Eurocode and another based on DNV.

The reliability indices are calculated by use of the First-Order Reliability Method (FORM) and validated with crude Monte Carlo simulation (MCS). It can be concluded that FORM is a reliable tool when using the semi-empirical methods, the GMNA and the GMNIA with LBMI₁ as initial geometric imperfection. This conclusion however, does not apply when using the GMNIA with LBMI₁₆ and TPDI as initial geometric imperfection, which is due to the highly non-linear mathematical simplifications introduced to calculate the imperfection knock down factor $X_{R,imp}$. Through this investigation, MCS is used to validate the results and it is concluded that the reliability level in general is lower compared to FORM, when using the GMNIA with LBMI₁₆ and TPDI as initial geometric imperfection.

It is shown that a relatively high reliability level is estimated when using the semi-empirical mathematical model in [DS/EN-1993-1-6, 2007] both in the design and limit state equation. This corresponds well with the calculated low coefficient of variation of the model uncertainty and the fairly high bias. A calibration of the partial safety factor γ_M is performed through an optimisation problem and it is shown that in the present case, a reduction from 1.20 to 1.05 is possible.

Comparison of the reliability level between the model with perfect geometry (GMNA) and the models with simulated initial geometric imperfections (GMNIA), shows in general a large reduction. It is concluded, that the imperfection pattern and the selected standard deviation of imperfection amplitude influences the reliability level greatly. The partial safety factor γ_M is calibrated for the GMNIA model with initial imperfections LBMI₁, LBMI₁₆ and TPDI, when using the semi-empirical mathematical model in [DS/EN-1993-1-6, 2007] in the design equation. A reduction of the partial safety factor from 1.20 to 1.05 is possible when using LBMI₁ as initial imperfection pattern. However, an increase from 1.20 to 1.25 is necessary to reach the target reliability when using LBMI₁₆ and TPDI as initial imperfection pattern. It is questionable though, whether the reliability level and thereby the calibration of partial safety factor for the GMNIA models are accurate since the results are based on model uncertainties related to GMNA.

From these considerations, no final conclusions can be made regarding the partial safety factor, but since [DS/EN-1993-1-6, 2007] recommends $\gamma_M = 1.10$ and the Danish national annex recommends $\gamma_M = 1.20$, this could indicate that the Danish national annex might be too conservative. From the presented analyses, it is not possible to provide clear guidelines of which imperfection pattern should be selected as initial geometric imperfection as well as imperfection amplitude due to the large variations in the critical buckling resistance.

Bibliography

- S. Batterman (1965). 'Plastic Buckling of Axially Compressed Cylindrical Shells'. *American Institute of Aeronautics and Astronautics* .
- J. Blachut (2010). 'Buckling of axially compressed cylinders with imperfect length'. *Computers and Structures* .
- M. Broggi, et al. (2011). 'Reliability assessment of axially compressed composite cylindrical shells with random imperfections'. *International Journal of Structural Stability and Dynamics* .
- D. Brush & B. Almroth (1975). *Buckling of bars, plates and shells*. McGraw-Hill. 9780070327580.
- D. Bushnell (1981). 'Buckling of shells - Pitfall for Designers'. *American Institute of Aeronautics and Astronautics* .
- D. Bushnell (2011). 'Shell buckling'.
http://shellbuckling.com/presentations/buckledShells/pages/page_15.html.
accessed: 2014-02-14.
- S. G. Castro, et al. (2013). 'Geometric imperfections and lower-bound methods used to calculate knock-down factors for axially compressed composite cylindrical shells'. *Thin-Walled Structures* .
- C. De Paor, et al. (2012). 'Statistical characterisation and modelling of random geometric imperfections in cylindrical shells'. *Thin-Walled Structures* .
- R. Degenhardt, et al. (2008). 'Probabilistic approach for improved buckling knock-down factors of CFRP cylindrical shells'. *In proceeding of: First CEAS European Air and Space Conference* .
- O. Ditlevsen & H. Madsen (1996). *Structural Reliability Methods*. Wiley.
- DNV-Note-30.6 (2013). 'Structural Reliability Analysis of Marine Structures'.
- DNV-RP-C202 (2013). 'Buckling Strength of Shells'.
- DS/EN-1990 (2007). 'Basis of Structural Design'.
- DS/EN-1993-1-6 (2007). 'Strength and Stability of Shell Structures'.
- DS/INF-172 (2009). 'Background investigations in relation to the drafting of National Annexes to EN 1990 and EN 1991 - Reliability verification formats, combination of actions, partial coefficients, fatigue, snowload, windload, etc.'
- M. Farshad (2010). *Design and Analysis of Shell Structures*. Springer. 9789048142002.
- JCSS (2001). 'Probabilistic Model Code'. Joint Committee on Structural Safety.

- K. Krabbenhøft (2002). *Basic Computational Plasticity*. Department of Civil Engineering Technical University of Denmark.
- C. Mathon & A. Limam (2006). 'Experimental collapse of thin cylindrical shells submitted to internal pressure and pure bending'. *Thin-Walled Structures* .
- B.-A. Memon & X.-z. Su (2004). 'Arc-length technique for nonlinear finite element analysis.'. *J Zhejiang Univ Sci* .
- Network Rail (2012). 'Edinburgh Architecture'. http://www.edinburgharchitecture.co.uk/images/jpgs/forth_rail_bridge_s280512.jpg. accessed: 2014-02-18.
- A. C. Orifici & C. Bisagni (2013). 'Perturbation-based imperfection analysis for composite cylindrical shells buckling in compression'. *Composite Structures* .
- N. Ottosen & M. Ristinmaa (2005). *The Mechanics of Constitutive Modeling*. Elsevier Science.
- J. Rotter & H. Schmidt (2008). *Buckling of Steel Shells: European Design Recommendations ; [Eurocode 3, Part 1 - 6]*. European Convention for Constructional Steelwork. 9789291470099.
- H. Schmidt (2000). 'Stability of Steel Shell Structures - General Report'. *Journal of Constructional Steel Research* .
- Simulia Corp. (2013). *ABAQUS/CAE User's Manual*. Dassault Systemes.
- J. Singer, et al. (1998). *Buckling Experiments, Basic Concepts, Columns, Beams and Plates*. Wiley. 9780471956617.
- J. Singer, et al. (2002). *Buckling Experiments, Shells, Built-up Structures, Composites and Additional Topics*. Wiley. 9780471974505.
- J. D. Sørensen (2004). 'Notes in Structural Reliability Theory And Risk Analysis'.
- J. D. Sørensen, et al. (2001). *Calibration of Partial Safety Factors and Target Reliability Level in Danish Structural Codes*. Aalborg University. Department of Mechanical Engineering.
- J. G. Teng (1996). 'Buckling of thin shell: Recent advances and trends'. *American Society of Mechanical Engineers* .
- J. G. Teng & J. M. Rotter (2004). *Buckling of Thin Metal Shells*. Spon Press. 0419241906.
- B. Wang, et al. (2013). 'Determination of realistic worst imperfection for cylindrical shells using surrogate model'. *Structural and Multidisciplinary Optimization* .
- M. S. Williams & J. D. Todd (2000). *Structures Theory and Analysis*. Palgrave Macmillan. 9780333677605.
- T. Winterstetter & H. Schmidt (2002). 'Stability of circular cylindrical steel shells under combined loading'. *Thin-Walled Structures* .

- A. Zingoni (1997). *Shell Structures in Civil and Mechanical Engineering: Theory and Closed-form Analytical Solutions*. T. Telford Pub. 9780727725745.

A Buckling strength according to EN 1993-1-6

In this appendix the buckling strength will be determined using the semi-empirical method suggested by [DS/EN-1993-1-6, 2007]. Only axially compressed cylindrical shells will be considered. In the calculation following parameters needs to be determine;

- The elastic critical meridional buckling stress $\sigma_{x,Rcr}$
- The elastic imperfection reduction factor α
- The relative shell slenderness $\bar{\lambda}_x$ and the plastic limit slenderness $\bar{\lambda}_p$
- The buckling reduction factor χ_x

The elastic critical meridional buckling stress

To determine $\sigma_{x,Rcr}$ the method in [DS/EN-1993-1-6, 2007], annex D is used and is calculated from (A.1).

$$\sigma_{x,Rcr} = 0.605EC_x \frac{t}{r} \quad (\text{A.1})$$

where

$\sigma_{x,Rcr}$	Elastic critical meridional buckling stress [Pa]
E	Young's modulus [Pa]
C_x	Factor [-]
t	Thickness [m]
r	Radius [m]

The factor C_x is determined from the dimensionless length parameter ω which indicates if the cylinder is; short, medium or long. In this thesis only medium length cylinder is considered and therefore $C_x = 1.0$, and thereby (A.1) is similar to the derived classical solution (1.9) on page 12.

The elastic imperfection reduction factor

To take into account imperfection the reduction factor α is introduced.

$$\alpha = \frac{0.62}{1 + 1.9 \left(\frac{\Delta w_c}{t}\right)^{1.44}} \quad (\text{A.2})$$

where

α	Elastic imperfection reduction factor [-]
Δw_c	Characteristic imperfection amplitude [m]

Δw_c is determined from

$$\Delta w_c = \frac{1}{Q} \sqrt{\frac{r}{t}} \quad (\text{A.3})$$

Where Q is a fabrication quality parameter which is selected to be $Q = 40$ corresponding to a quality class A, since it is assumed that the cylinders in [Batterman, 1965] are close to perfect.

The relative shell slenderness $\bar{\lambda}_x$ and the plastic limit slenderness $\bar{\lambda}_p$

$\bar{\lambda}_p$ and $\bar{\lambda}_x$ is determined from (A.4) and (A.5) respectively.

$$\bar{\lambda}_p = \sqrt{\frac{\alpha}{1 - \beta}} \quad (\text{A.4})$$

$$\bar{\lambda}_x = \sqrt{\frac{f_{yc}}{\sigma_{x,Rcr}}} \quad (\text{A.5})$$

where

$\bar{\lambda}_p$	Plastic limit slenderness [-]
β	Plastic range factor (=0.60) [-]
$\bar{\lambda}_x$	Relative shell slenderness [-]
f_{yc}	Characteristic yield strength [Pa]

The buckling reduction factor χ_x

The buckling reduction factor is determined as a function of the relative slenderness of the shell and is given by;

$$\chi_x = 1 \quad \text{when} \quad \bar{\lambda}_x \leq \bar{\lambda}_0 \quad (\text{A.6})$$

$$\chi_x = 1 - \beta \left(\frac{\bar{\lambda}_x - \bar{\lambda}_0}{\bar{\lambda}_p - \bar{\lambda}_0} \right)^\eta \quad \text{when} \quad \bar{\lambda}_0 < \bar{\lambda}_x < \bar{\lambda}_p \quad (\text{A.7})$$

$$\chi_x = \frac{\alpha}{\bar{\lambda}_x^2} \quad \text{when} \quad \bar{\lambda}_p \leq \bar{\lambda}_x \quad (\text{A.8})$$

where

χ_x	Buckling reduction factor [-]
λ_0	Squash limit slenderness (=0.20) [-]
η	Interaction exponent(=1.0) [-]

The characteristic buckling stress can then be determined using (A.9)

$$\sigma_{x,Rc} = \chi_x f_{yc} \quad (\text{A.9})$$

The design buckling stress is determined as:

$$\sigma_{x,Rd} = \frac{\sigma_{x,Rc}}{\gamma_M} \quad (\text{A.10})$$

B Buckling strength according to DNV-RP-C202

In this appendix the buckling strength will be determined using the semi-empirical method suggested by [DNV-RP-C202, 2013]. Only axially compressed cylindrical shells will be considered. In the calculation following parameters needs to be determine;

- The elastic buckling strength f_E
- The reduced shell slenderness $\bar{\lambda}_s$

The elastic buckling strength

Since the cylinder in this thesis is unstiffened the elastic buckling strength is given by;

$$f_E = C \frac{\pi^2 E}{12(1 - \nu^2)} \left(\frac{t}{l} \right)^2 \quad (\text{B.1})$$

where

f_E	Elastic buckling strength stress [Pa]
C	Reduced buckling coefficient [-]
E	Young's modulus [Pa]
ν	Poisson's ratio [-]
t	Thickness [m]
l	Length [m]

The reduced buckling coefficient C is a function of the applied load on the cylinder and the dimensionless curvature parameter Z given by (B.2) and (B.3) respectively.

$$C = \psi \sqrt{1 + \left(\frac{\rho \xi}{\psi} \right)^2} \quad (\text{B.2})$$

$$Z = \frac{l^2}{rt} \sqrt{1 - \nu^2} \quad (\text{B.3})$$

where

ψ	Buckling coefficient (=1.0) [-]
$\rho = 0.5 \left(1 + \frac{r}{150t} \right)^{-0.5}$	Buckling coefficient [-]
$\xi = 0.702Z$	Buckling coefficient [-]
r	Radius [m]

The reduced shell slenderness

$\bar{\lambda}_s$ is a function of; the stresses, elastic buckling strength and the yield stress, and is defined by

$$\bar{\lambda}_s^2 = \frac{f_y}{\sigma_{j.Sd}} \left(\frac{\sigma_{a0.Sd}}{f_E} \right) \quad (\text{B.4})$$

where

$$\begin{array}{l|l} \bar{\lambda}_s & \text{Reduced shell slenderness [-]} \\ f_y & \text{Yield stress [Pa]} \\ \sigma_{j,Sd} = \sqrt{\sigma_{a0,Sd}^2} & \text{von Mises stress [Pa]} \\ \sigma_{a0,Sd} & \text{Axial stress [Pa]} \end{array}$$

The characteristic buckling strength f_{cs} can then be determined using (B.5)

$$f_{cs} = \frac{f_y}{\sqrt{1 + \bar{\lambda}_s^4}} \quad (\text{B.5})$$

The design buckling stress is determined as:

$$f_{ds} = \frac{f_{cs}}{\gamma_M} \quad (\text{B.6})$$

where

$$\begin{array}{ll} \gamma_M = 1.15 & \text{for } \bar{\lambda}_s < 0.5 \\ \gamma_M = 0.85 + 0.60\bar{\lambda}_s & \text{for } 0.5 \leq \bar{\lambda}_s \leq 1.0 \\ \gamma_M = 1.15 & \text{for } \bar{\lambda}_s > 1.0 \end{array} \quad (\text{B.7})$$

C Mode shapes

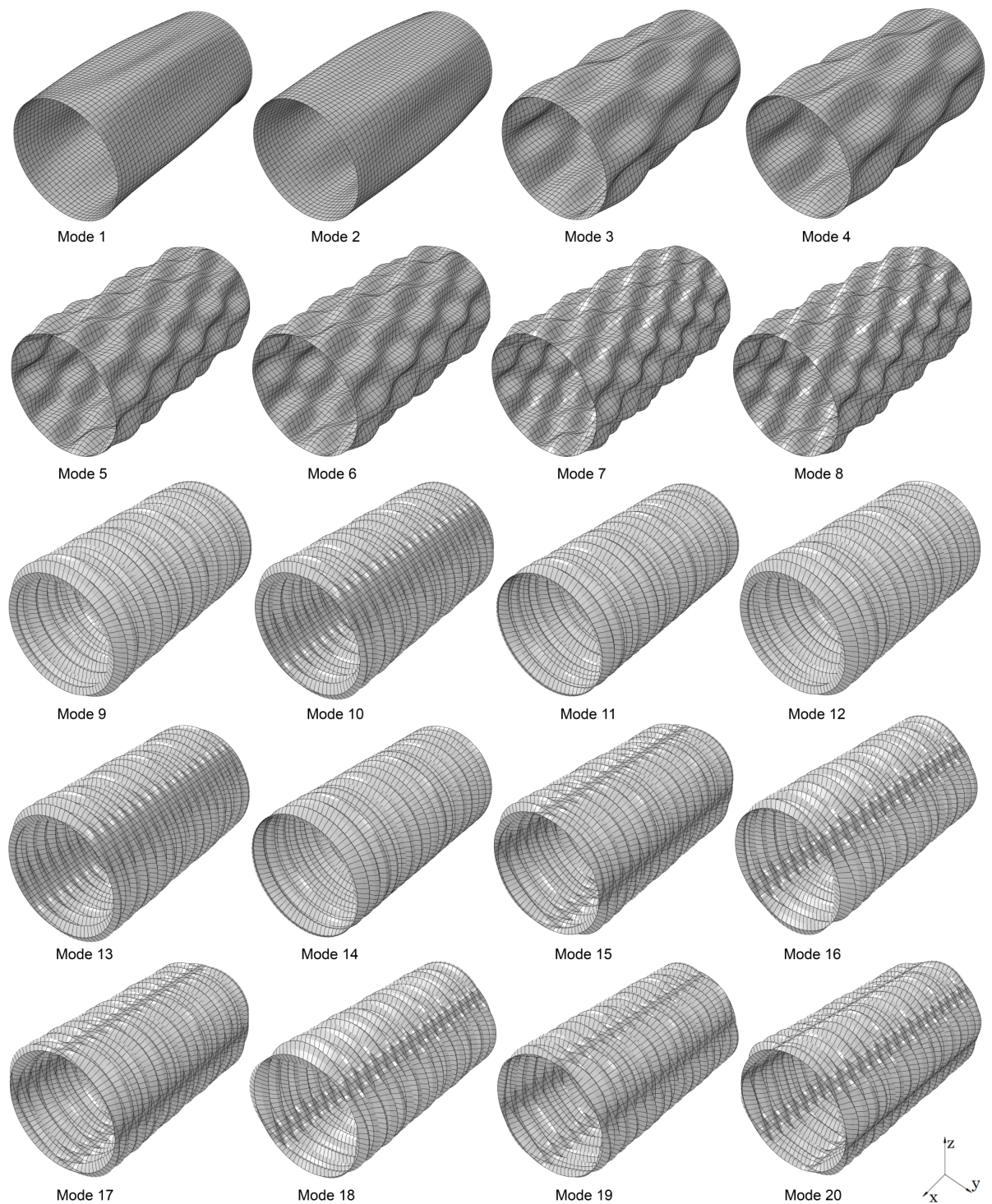


Figure C.1: Visualization of the mode shapes 1-20 obtained through LBA. Scale=0.3.

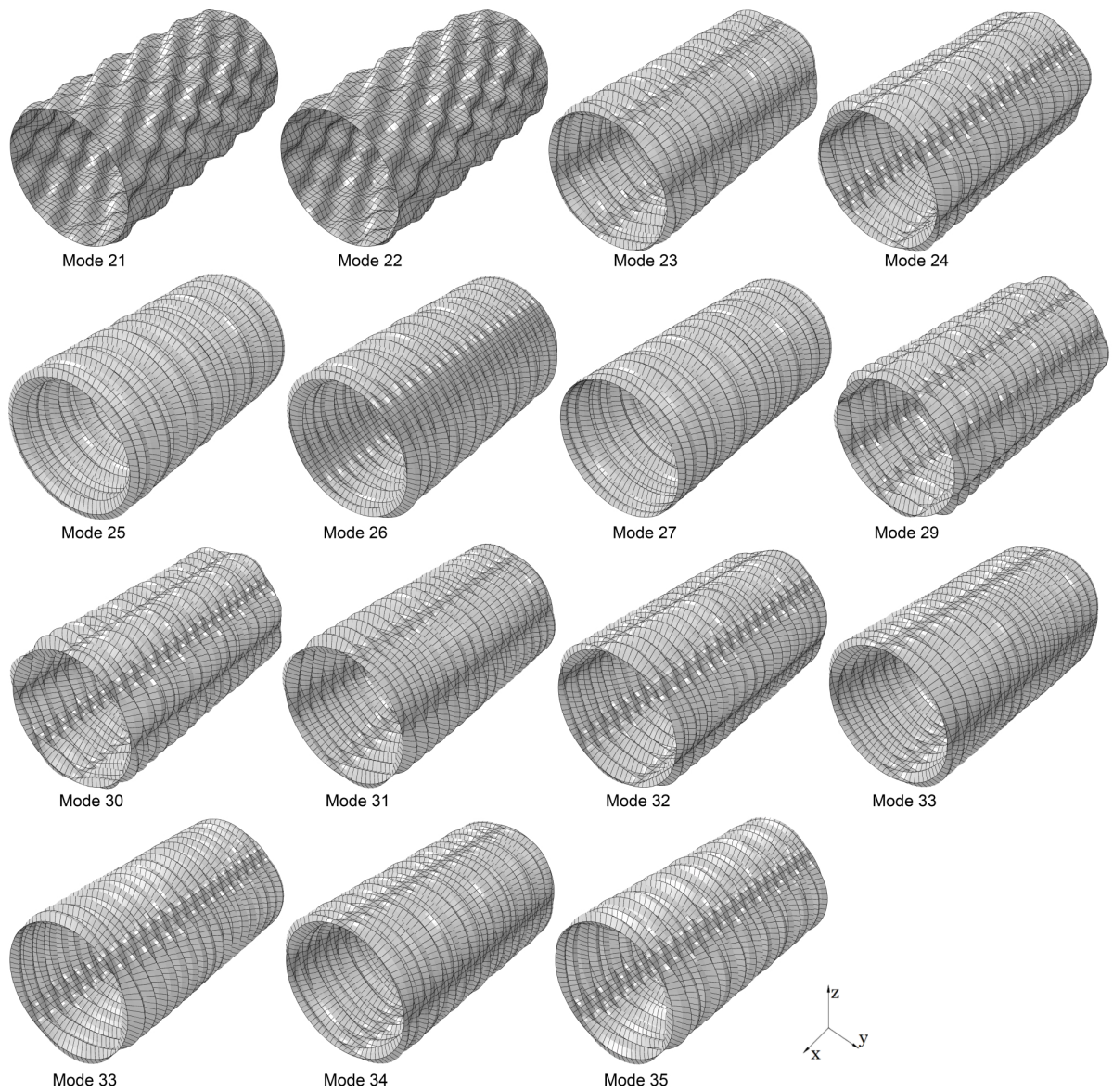


Figure C.2: Visualization of the mode shapes 21-35 obtained through LBA. Scale=0.3.